Constraints on subvolcanic magma plumbing system evolution from crystal size distribution analysis of igneous groundmass, Henry Mountains, Utah

By

Tess Oldroyd-Johnson

July 2024

Director of Thesis: Eric Horsman, PhD

Major Department: Geological Sciences

ABSTRACT

Shallow magma systems drive surface volcanism and are commonly built through multiple injections of magma. Recognizing separate magma injections can be difficult because differences in resulting rock texture, geochemistry, etc. may be subtle or non-existent. However, differences in injection crystallization histories may be recognizable through analysis of the late-crystallizing groundmass in porphyritic subvolcanic igneous rocks. In igneous bodies built from component magma sheets, early injections generally cool rapidly relative to later injections, resulting in distinct groundmass crystal size distribution (CSD) in the youngest, slowly cooled magma sheets compared to older, faster-cooled sheets. Previous work demonstrates that the ~28 Ma Copper Ridge laccolith (Henry Mountains, Utah) was constructed at a depth of ~2 km from at least two texturally distinct igneous sheets stacked atop one another and suggests these two sheets may themselves include multiple injections of magma. This study tests the hypothesis that the relative timing between intrusive sheets in a laccolith can be constrained using CSD analysis of groundmass texture and that the individual intrusive sheets are comprised of multiple pulses of magma.

To test this, a suite of porphyritic diorite samples was collected from a natural cross-

section through the entire 400-m-thick Copper Ridge intrusion, including samples at well-exposed upper and lower contacts of the laccolith with sedimentary host rock, at contacts with an intercalated layer of host rock within the laccolith, and at regular intervals within the upper and lower igneous sheets themselves. CSD analysis was conducted on electron backscattered diffraction (EBSD) mineral phase maps of quartz, anorthite, and orthoclase in the groundmass (crystals <100 microns).

Examining the crystal size population density variation across different elevations of the Copper Ridge Laccolith (CRL) reveals that samples at some elevations have a wider variation of population density while some elevations have a narrower variation. Overall, the pattern of CSD for the ~100 m thick upper sheet is consistent with injection of a single magma pulse and shows generally larger groundmass crystals suggesting it cooled relatively slowly and perhaps intruded after the lower sheet. The pattern of CSD for the ~300 m thick lower sheet is more complex and shows a wider variation of crystal sizes but has generally fewer large groundmass crystals, suggesting it was intruded before the upper sheet and is constructed from three or more component pulses of magma, each being approximately 100 m thick.

The results of this study provide insight into the construction history of the CRL, suggesting that it was constructed through multiple magma pulses, each leaving distinct CSD patterns in the upper and lower sheets. These findings have significant implications for understanding the construction history of shallow magma systems, as CSD analysis can help identify and interpret the timing and dynamics of multiple magma injections within igneous intrusions. By demonstrating the effectiveness of CSD analysis, this research provides a valuable framework for studying the complex histories of other shallow magma systems and the processes driving surface volcanism.

Constraints on subvolcanic magma plumbing system evolution from crystal size distribution analysis of igneous groundmass, Henry Mountains, Utah

A Thesis

Presented to the Faculty of the Department of Geological Sciences

East Carolina University

In Partial Fulfillment of the Requirements for the Degree

Master of Science in Geology

By

Tess Oldroyd-Johnson

July 2024

Director of Thesis: Eric Horsman, PhD

Thesis Committee Members:

Ryan Currier, PhD

David Farris, PhD

Adriana Heimann Rios, PhD

Acknowledgments

First and foremost, I would like to thank my thesis advisor Dr. Eric Horsman, whose endless support and encouragement have made this project possible. His guidance during fieldwork, data analysis, writing, and life in general has been instrumental in the completion of my thesis. I couldn't have asked for a better advisor, and I am so grateful for his mentorship and unwavering support. I would also like to thank my committee members, Dr. David Farris, Dr. Adriana Heimann Rios, and Dr. Ryan Currier for their involvement and help throughout my research and for their review of my thesis. And thank you to the community of the Department of Geological Sciences at East Carolina University for the supportive and encouraging learning environment.

A special thank you to my insanely loving and supportive family. To my dad, thank you for supporting me and my education in so many ways to accomplish my goals and chase my dreams. To my momma, thank you for being the best mom in the world for teaching me so much and inspiring me to be the best person I can be. And to my dear husband, thank you for always literally and figuratively "carrying my rocks for me". I love you all.

Finally, I would like to thank the Geological Society of America Mineralogy, Geochemistry, Petrology, and Volcanology Division and the Lipman Student Research Grant for funding this project.

Table of Contents

List of Tables

List of Figures

1 Introduction

Surface volcanism is the ultimate end for magma generated at depth, which is subsequently transported, stored, and potentially altered along its path through the crust. Our understanding of how magmatic plumbing system development has changed in recent years. Previously, magmatic intrusions were thought to be formed as a single event, contiguous magma bodies (i.e., a “big tank”) (McBirney, 1996). However, research on well-exposed intrusions, utilizing methodologies such as textural analysis, geochemical studies, and geochronological techniques, has demonstrated that many subsurface intrusions form through multiple pulses of magma (Glazner et al., 2004; Coleman et al., 2004; Horsman et al., 2005, 2009; De Saint Blanquat et al., 2011).

Magma plumbing systems grow and evolve with each new pulse of magma. Volcanic systems can remain active for hundreds of thousands to millions of years, yet they can erupt on much shorter human time scales, ranging from decades to hundreds of years (De Saint Blanquat et al., 2011). The complicated interplay of heat and mass transport, host rock deformation, and volatile pressure within subsurface plumbing systems can result in frequent eruptions or long periods of repose. Examining the intricacies of these magma plumbing systems is crucial to better understand volcanic eruptions, and potentially our ability to forecast eruptions. The numerous injections influence the temperature of surrounding rocks and existing magma, thereby affecting their crystallization history. Igneous groundmass in porphyritic rocks contains a record of the ascent and emplacement of the magma. By analyzing the finest portions of the groundmass, a record of the final stages of emplacement can be interpreted. This study utilizes a detailed quantitative analysis of igneous textures to interpret the growth and evolution of a well-exposed portion of a magma plumbing system intruded into the shallow crust. Crystal size distribution (CSD) analysis of the igneous groundmass provides insight on the late-stage magma ascent and emplacement in the shallow crust.

The study area for this work is within the Henry Mountains of southern Utah, which consist of five igneous intrusive centers (Hunt et al., 1953; Nelson et al., 1992) (Figure 1 A). This study focuses on the Copper Ridge Laccolith (CRL), a tongue-shaped igneous lobe radiating from the east side of Mount Ellen (Figure 1 B). The CRL provides an exceptional exposure of two igneous sheets: an upper sheet approximately 80-100 m thick capped by sedimentary host rocks, and a lower sheet about 300-400 m thick, lying atop sedimentary host rock. Separating the two igneous sheets is a layer of shale (Maurer, 2015).

For this study, a suite of samples was collected focusing on the upper and lower contacts of both sheets complemented by previously collected samples taken at regular intervals throughout the ~400 m thick cross-section. Using a variety of methods, including electron microscopy and CSD analysis, I test the hypothesis that the Copper Ridge Laccolith was constructed through multiple pulses of magma, resulting in multiple component sheets of magma comprising it.

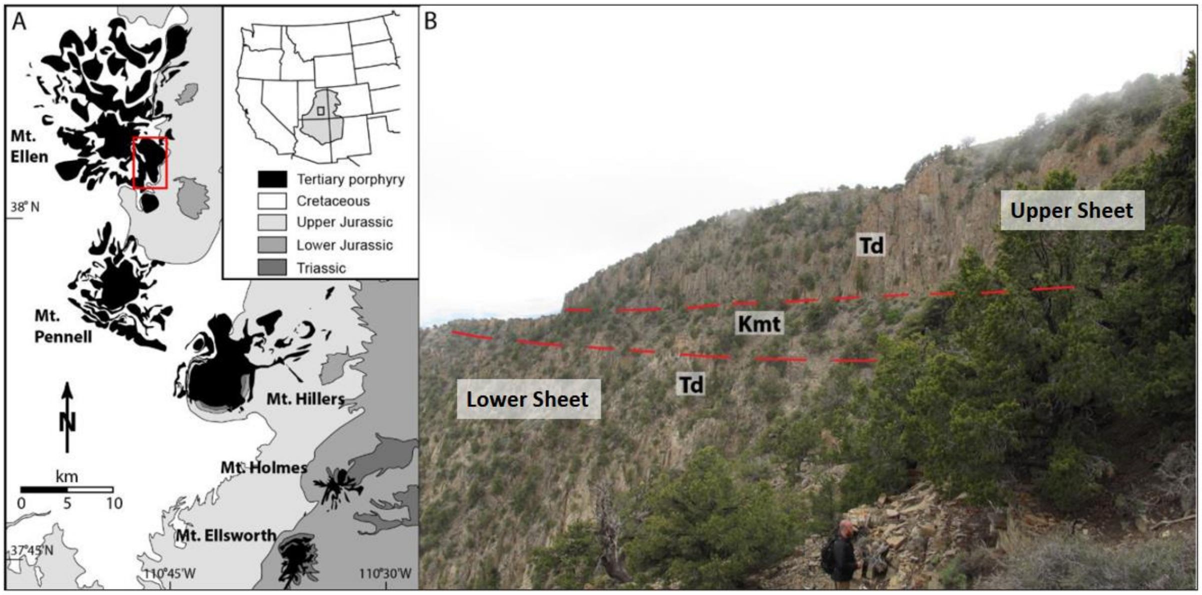

Figure 1. A- Map showing the location of the Henry Mountains in Utah with associated stratigraphy. The Copper Ridge Laccolith on Mount Ellen is outlined in red. Modified from Horsman et al., 2009. B- Photo showing a cross-section of the Copper Ridge laccolith with geologic units labeled. Modified from Maurer, 2015.

2 Background

2.1 Volcanic Plumbing Systems

Volcanoes are fed by transcrustal magma systems beneath the Earth's surface (Figure 2). Understanding how volcanic systems operate in the subsurface is essential for understanding the formation of igneous intrusions. The processes by which magma is delivered and emplaced in the subsurface facilitates the formation of igneous intrusions of varying sizes, from sills to batholiths.

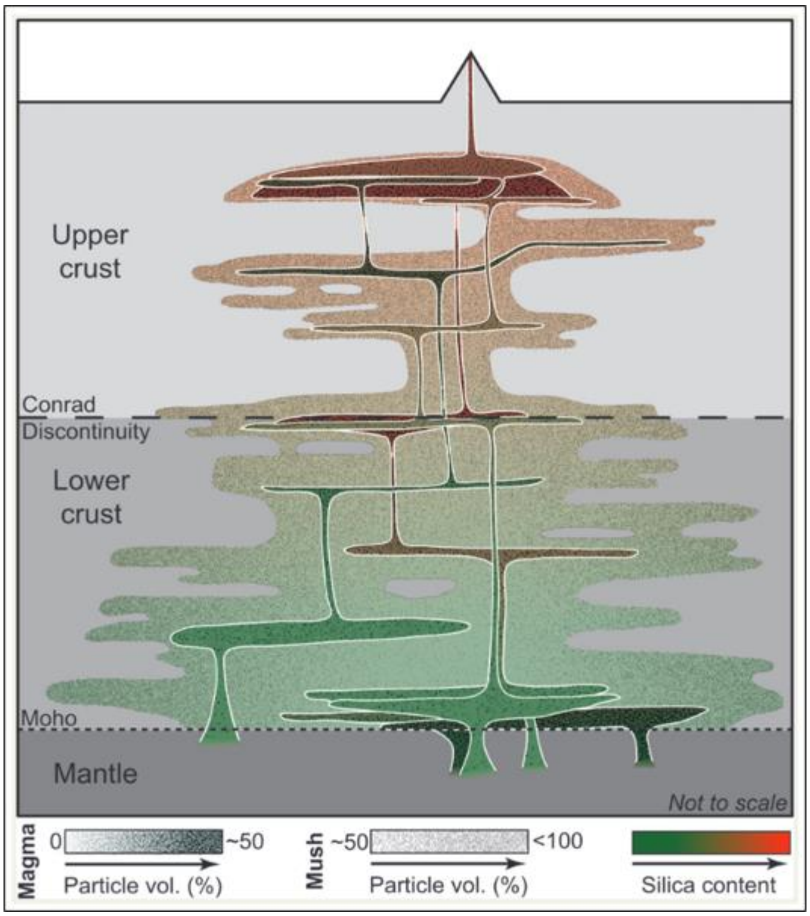

Figure 2. Schematic of a transcrustal magma plumbing system showing interconnected tabular magma intrusions (dikes, sills, laccoliths) within a crystal mush. From Magee et al., 2018.

2.1.1 *Magma Storage and Transport*

Magma is transported and stored in conduits and reservoirs of differing geometries and depths in a network of channels called magma plumbing systems (Figures 2 and 3) (Tibaldi, 2015). Magma plumbing systems consist of dikes, sills, vertical or inclined conduits, horizontal concordant intrusions, and chambers where magma can be stored (Figure 3) (Best, 1982; Tibaldi, 2015). Dikes serve as primary channels for pressurized magma to propagate through the upper crust to form igneous bodies (Gudmundsson, 1990; Annen et al., 2008; Gonnermann and Taisne, 2015). Sills also contribute to magma plumbing system and laccolith growth with the lateral movement of magma (Kavanagh et al., 2006; Menand, 2008). Large amounts of magma from these plumbing systems fail to reach the surface as eruptive products and rather remain in the subsurface to cool and crystallize, with the ratio of intrusive to extrusive igneous volumes estimated to be 2-3:1 in most magmatic systems (White et al., 2006). These magmatic intrusions cool and crystallize, transferring their heat into the surrounding wall rock, and at scale, can significantly alter the thermal conditions within the crust (Annen et al., 2008). Exhumed magmatic intrusions provide clues of the inner workings of magmatic systems. By reconstructing the dynamic histories of exposed magmatic plumbing systems, new insights can be gained of subsurface processes at active volcanoes (Tibaldi, 2015).

The term "magma" is loosely defined and typically refers to a multiphase mixture that includes liquid melt, dissolved or exsolved volatiles, and varying amounts of crystals (Figure 2) (Tibaldi, 2015). Magee et al. (2018) define ‘magma’ as fully or partially molten rock material consisting of melt with or without crystals and gas bubbles and containing a high enough proportion of melt to be capable of intrusion and extrusion. As magma begins to solidify, the proportion of suspended crystals increases, leading to an increase in the magma’s bulk viscosity

(Arzi, 1978). This process continues until a relatively immobile, continuous network of crystals and interstitial melt forms, which is referred to as a ‘crystal mush’ (Magee et al., 2018). Late-stage crystallization is important to this study because it provides a record of the final stages of magma ascent and emplacement.

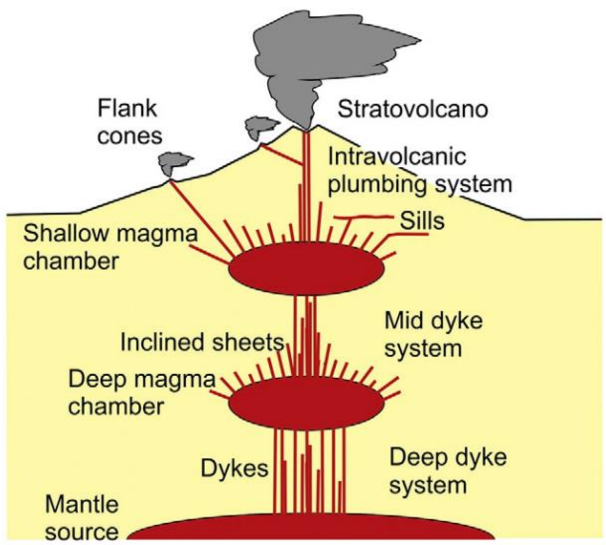

Figure 3. A magma plumbing system represented as a network of conduits channeling magma toward the surface and storage chambers. From Tibaldi, 2015.

2.1.2 Progressive Laccolith Construction

A laccolith is an igneous intrusion with a flat base, a convex-up roof, and formed from one or more amalgamated pulses of magma typically emplaced at a crustal depth of 3 km or less (Gilbert, 1877; Corry, 1988). Laccoliths serve as primary storage reservoirs for magma in the upper crust and often directly feed volcanic eruptions, also, the lateral transport of magma in the upper crust often occurs in sills which are often the foundational components of laccoliths (Corry, 1988; Castro et al., 2016). It is well established that numerous igneous intrusions of varying spatial scales, including laccoliths, can develop through sequential injections of separate magma pulses (Figure 4). Evidence from larger volume intrusions indicates that laccoliths form through stacked sheets or the amalgamation of multiple magma pulses (Glazner et al., 2004; Horsman et al., 2005, 2009, 2018; Morgan et al., 2008; De Saint Blanquat et al., 2011; Ward, 2014; Broda, 2014; Maurer, 2015; Currier and Marsh, 2015). However, recognizing changes (e.g. new injections) in magma plumbing systems can be difficult.

Different intrusion geometries and compositions reflect distinct aspects of magma transport. Within the deeper crust, typically below depths of 12-15 km, materials exhibit predominantly ductile behavior, resulting in blob-like magma bodies. In the upper crust, materials tend to behave in a brittle manner, leading to the development of magma bodies with sheet-like geometries due to fracturing processes within the host rock.

In the upper crust, where rock behaves brittlely, dikes serve as conduits for vertical magma movement bodies (Gudmundsson, 1990; Annen et al., 2008; Gonnermann and Taisne, 2015). Once a dike reaches a certain depth in the crust, it becomes mechanically more favorable to propagate laterally than to continue vertical ascent and will transition to a sill (Elliot et al., 1999; Thomson and Hutton, 2004; Hansen and Cartwright, 2006). With lateral expansion, a sill may eventually reach an areal extent where it becomes easier to lift the overlying strata rather than continue lateral growth, prompting the formation of a laccolith (Gilbert, 1877; Elliot et al., 1999) (Figure 4). Once a fracture develops within the upper crust, it represents a mechanical weakness, making it easier to utilize the existing fracture rather than initiate a new one. Magma conduits in the upper crust that exploit fractures and other mechanical weaknesses, like dikes and sills, can undergo repeated utilization.

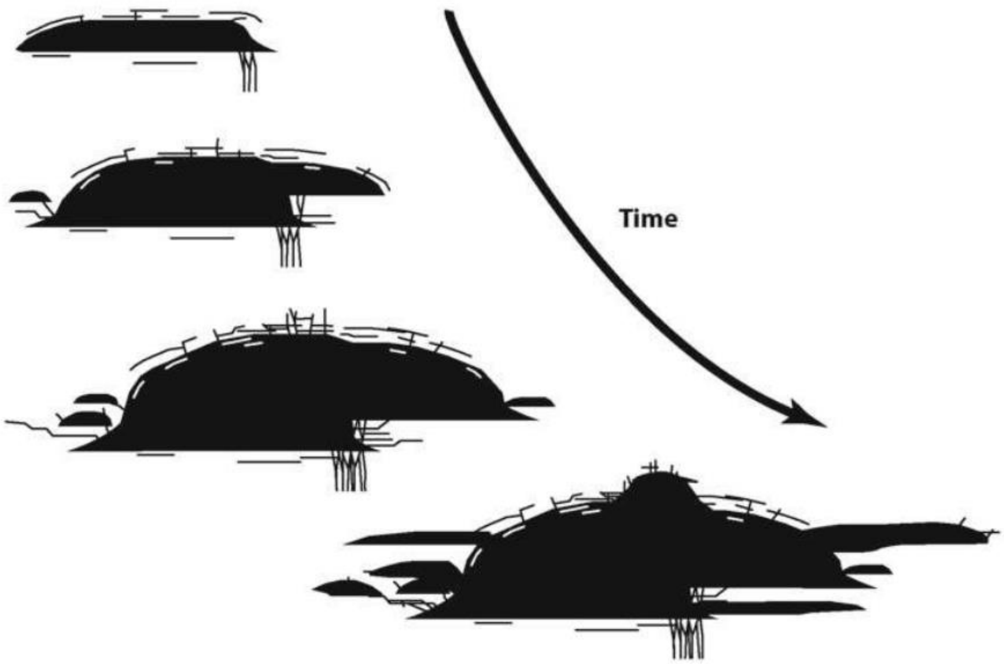

Figure 4. Schematic diagram showing the progressive growth of a laccolith over time. From Horsman et al., 2018.

2.1.3 Magma Pulses

For this study, a magma pulse can be defined as a single injection of magma that contributes to the overall construction of an igneous intrusion (De Saint Blanquat et al., 2011). The formation and expansion of igneous bodies in the subsurface often involve multiple pulses of magma. It is fairly common for intrusions within the upper crust, such as dikes, sills, or laccoliths, to be built through the accumulation of multiple pulses or injections of magma (Figure 5). Identifying separate injections can be straightforward when good indicators such as contrasts in composition or textures are present. However, these indicators of internal contacts are often cryptic, resulting in limited knowledge about the typical geometric forms of individual pulses (Glazner et al., 2004).

For this study, a magma “sheet” is defined as the main observed upper and lower sills of the CRL. It is inferred that these main sheets are built from multiple pulses or injections of texturally distinct magma which I will call “component sheets.”

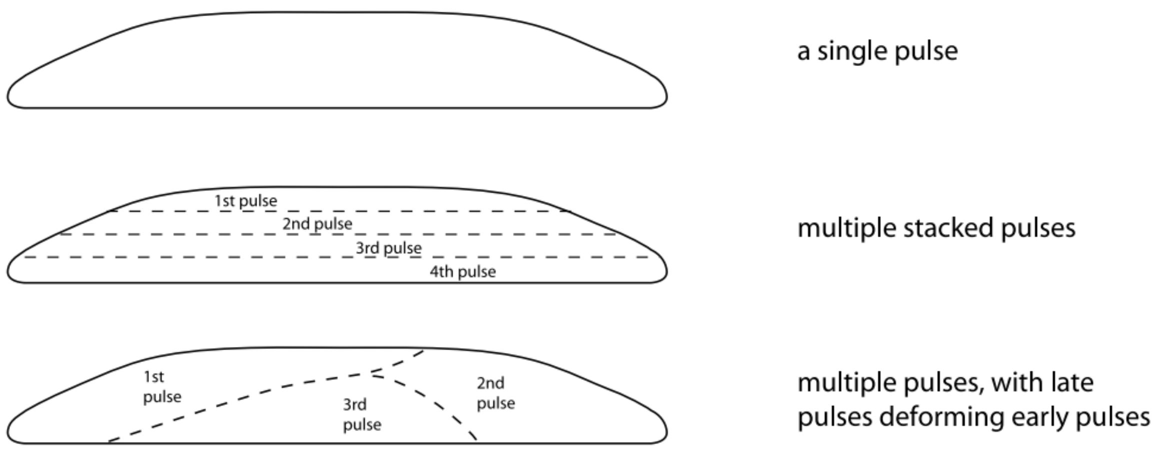

Figure 5. Schematic diagram illustrating pulsed assembly through multiple injections (pulses) of magma. Modified from Horsman et al., 2009.

2.1.4 Timescale of Igneous Intrusion Construction and Volcanic Eruptions

The timescale for the construction of igneous intrusions is strongly correlated with the volume of the pluton, as demonstrated De Saint Blanquat et al. (2011). The larger the pluton, the longer its construction time (Figure 6). Most igneous intrusions, regardless of tectonic setting, tend to grow at a limited range of magma injection rates (2-3 orders of magnitude) on geological timescales.

Research on volcanic systems shows that the frequency of eruptions is linked to the bulk composition of the system (Caricchi et al., 2021). Active mafic systems typically exhibit shorter intervals between eruptions, spanning from days to years, whereas more felsic systems tend to have eruptions over longer timescales, ranging from years to centuries (Weber et al., 2020). These eruptions are presumably all driven by changes in the subsurface magma plumbing system. Geophysical methods can be employed to correlate evidence of magma plumbing system evolution to active eruptions (Burchardt and Galland, 2016). In some instances, these conduits for magma migration extend to the earth's surface resulting in a volcanic eruption. Eruptions can also be triggered by interactions with the near-surface environment (Caricchi et al., 2021), such as a phreatic eruption.

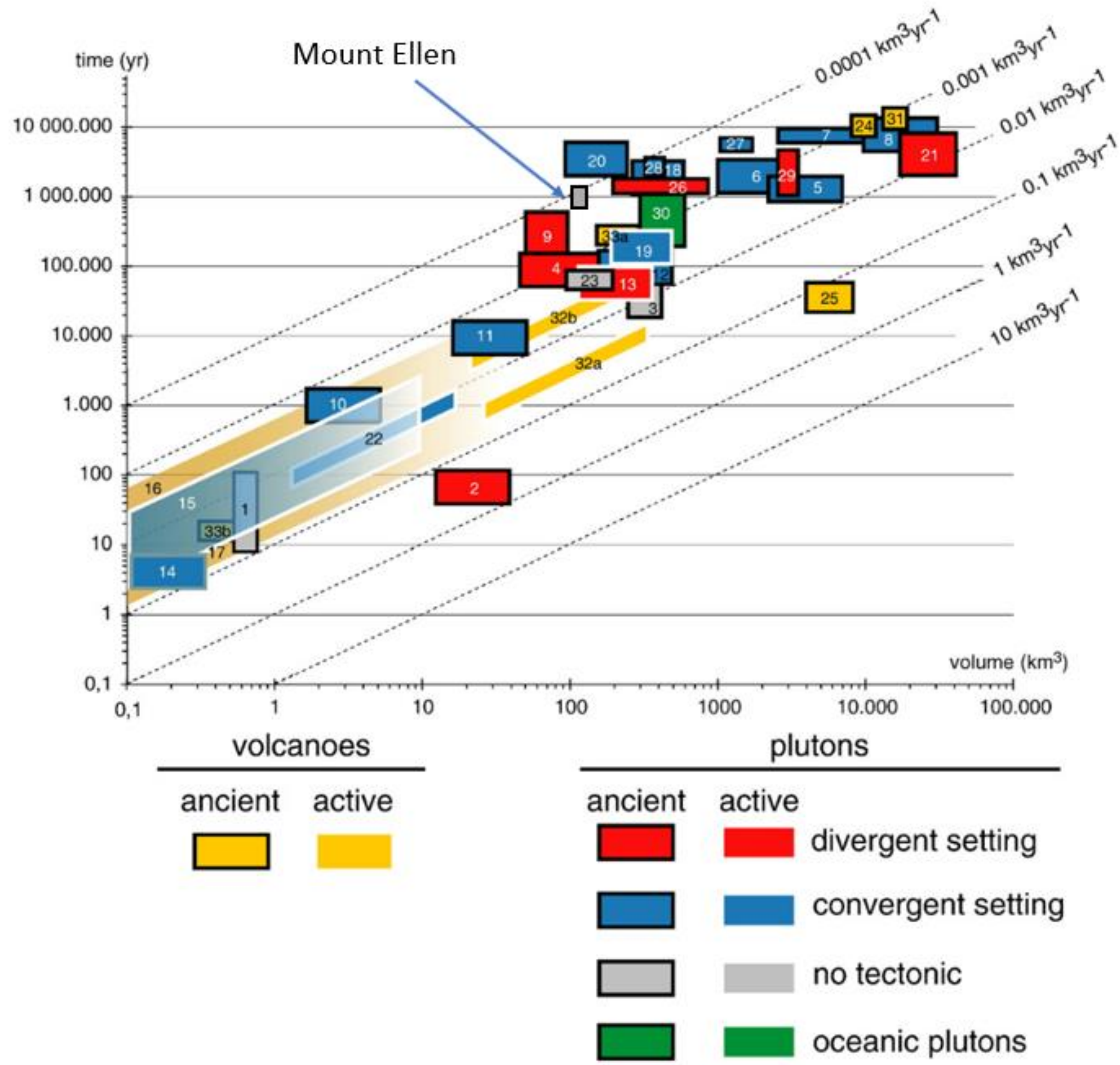

Figure 6. Compilation of available data on the duration and rates of pluton construction for various pluton sizes. Modified from De Saint Blanquat et al., 2011.

2.2 CSD Background

Igneous rock texture is a result of the crystallization process or history of a melt. The crystallization history of a melt results from the thermal cooling and/or decompression of a magma body. Crystal Size Distribution (CSD) analysis aims to quantitatively describe the textural features of an igneous rock sample by measuring the size and distribution of crystals. This provides constraints on the crystallization history and therefore the cooling and decompression history of igneous rocks (Marsh, 1988, 2007; Higgins, 1999, 2000, 2011; Cashman, 2020).

A traditional CSD plot shows the relationship of the natural log of the population density of the crystals versus the size of the crystals (Figure 7). The CSD curve is defined by connecting the points at the midpoint of each crystal size bin (Figure 8). The number of determined bins varies depending on the sample and the crystal sizes within each sample. The crystal abundance in each bin determines the population density for that interval. The natural log of the population densities is then plotted against the midpoint values of each size bin. Units for the natural log of the population density are $length^{-4}$, as the volumetric number density of crystals has the units of $length^{-3}$, and it is divided by a length (the interval width of the bin size).

The size and shape of the resulting slope as well as the intercepts can be interpreted to tell us about the crystallization history of the rocks (Figure 9). The igneous textures can be quantitatively compared using CSD plot characteristics such as slope, y-intercept, etc.

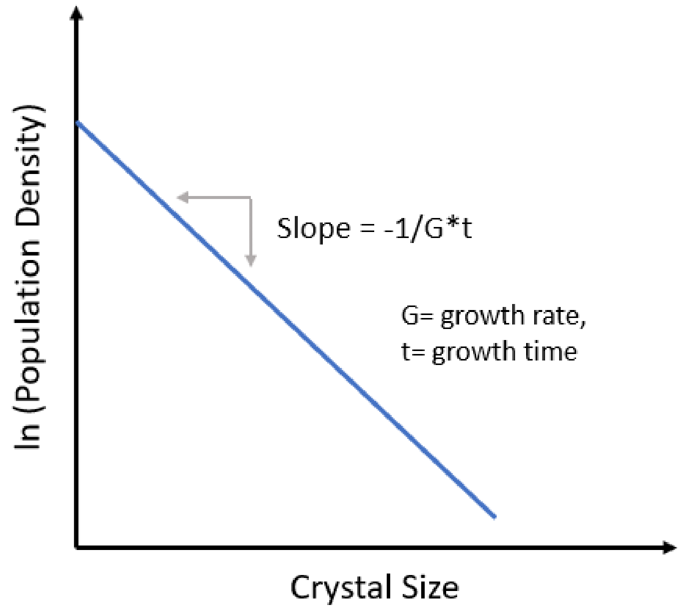

Figure 7. Schematic diagram of a traditional CSD plot showing the population density (y-axis) and the crystal size (x-axis).

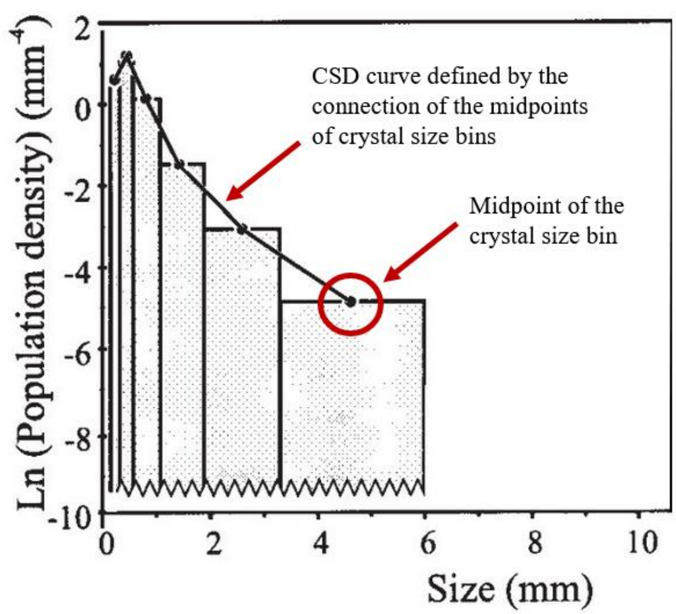

Figure 8. Diagram of how a CSD curve is produced from the mid-point of histogram bins. Modified from Higgins, 2000.

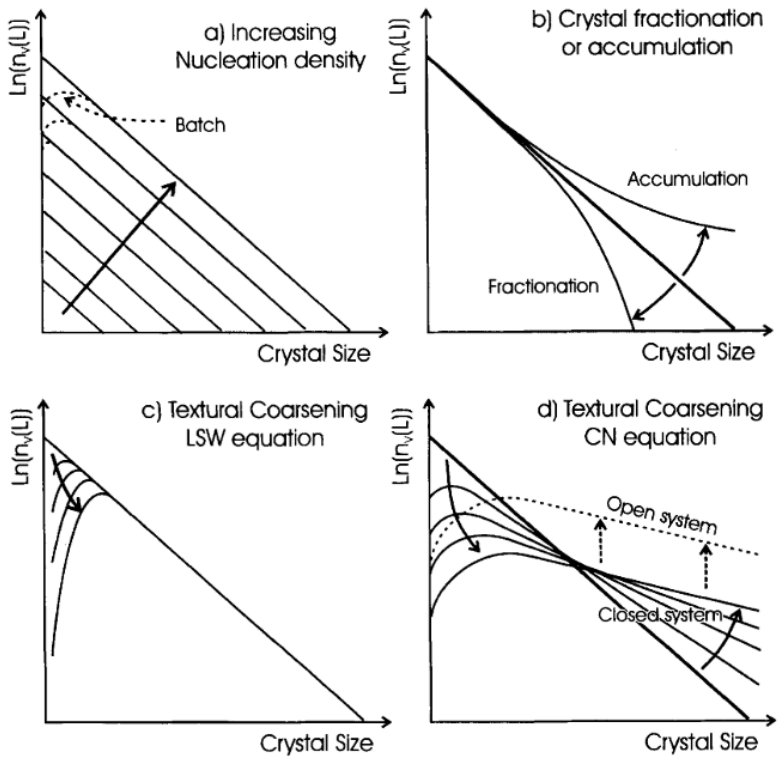

Figure 9. Diagram showing various ways to interpret differences in CSD plots based on changes in slope and intercept. From Higgins, 1999.

2.3 Geologic Setting

2.3.1 Colorado Plateau

The Colorado Plateau extends about 350,000 km^2 (150,000 mi^2) in the North American Cordillera and covers parts of Utah, Colorado, Arizona, and New Mexico (Figure 10) (Hunt, 1956). It consists of 45-50 km thick cratonic crust (Thompson and Zoback, 1979) and mostly consists of subhorizontal Phanerozoic sedimentary strata on top of Precambrian basement rock with little magmatic activity.

While much of the North American Cordillera experienced intense deformation during the Phanerozoic, the Colorado Plateau remained relatively stable. This stability is attributed to earlier crustal thickening (Thompson and Zoback, 1979; Nelson et al., 1992; Nelson and Davidson, 1993; Flowers, 2010). The interior of the Plateau was less affected due to the structural and rheological properties of its thickened crust (Thompson and Zoback, 1979; Nelson and Davidson, 1993).

The most voluminous Phanerozoic magmatic activity in the Colorado Plateau region consists of the laccoliths of the Henry, La Sal, and Abajo Mountains, which are dated to 31-20 Ma (Nelson et al., 1992) (Figure 10).

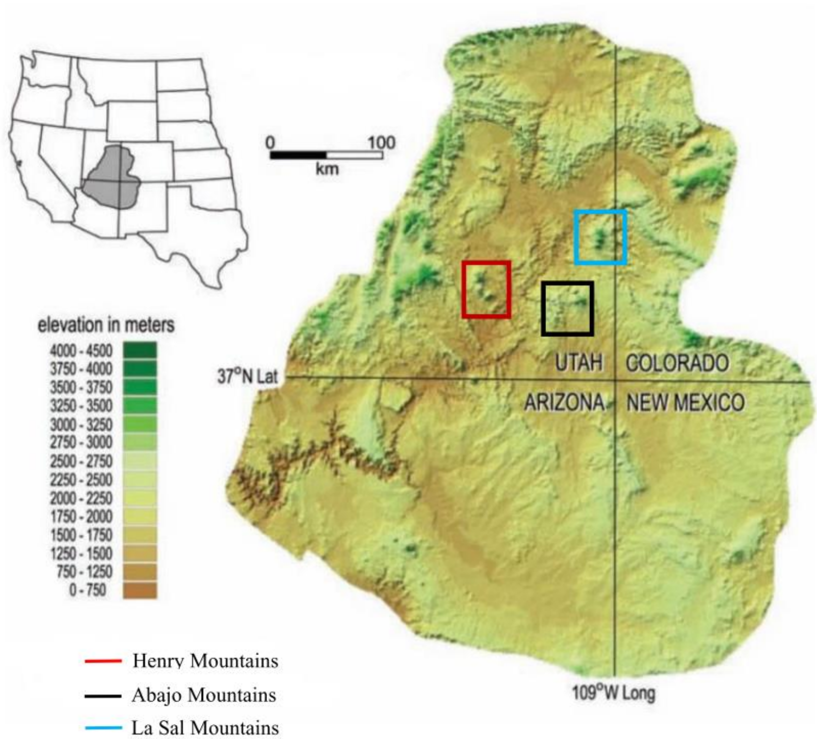

Figure 10. Location and elevation map of the Colorado Plateau. Colored boxes indicate magmatic activity on the plateau. From de Sousa, 2021 modified from Pederson et al., 2002.

2.3.2 The Henry Mountains

The Henry Mountain intrusions in southern Utah (Figure 11) were emplaced in the Oligocene in very shallow (1-3 km) crust of the Colorado Plateau. Each of the five large laccolithic intrusive centers consists of a central igneous body from which radiate numerous lobes and sheets, such that the overall laccolith is built from dozens of component intrusions (Jackson and Pollard; Horsman et al., 2018). Published geochronology data (Nelson et al., 1992; Murray et al., 2016) places the range of Henry Mountains igneous rock ages between 28-25 Ma. The rocks are mostly porphyritic andesite. However, these studies did not have sufficient data to constrain the growth duration of any individual intrusive center. In-progress work on Mt. Hillers using U-Pb TIMS data on zircon suggests an overall emplacement range of ~220,000 years for the ~35 km^3 volume of igneous rock of Mount Hillers (Paquette et al., in review). Previous studies on the Henry Mountains (Horsman et al., 2018; de Sousa, 2021) show that these laccoliths are built from multiple component intrusions emplaced on much smaller time scales.

Early work in the Henry Mountains (e.g. Hunt et al., 1953) suggested four of the five laccolithic intrusive centers are generally very homogeneous in igneous composition and texture. More recent work (Ward, 2014; Broda, 2014; Maurer, 2015; Horsman et al., 2018) demonstrates that Mt. Pennell and Mt. Ellen exhibit clear evidence of construction through multiple texturally and geochemically distinct magma injections. The evidence of multiple injections for Mt. Hillers is less clear, although numerous distinct textures have been identified (e.g. Thornton, 2014; Broda, 2014), comprehensive mapping and detailed studies have yet to be conducted.

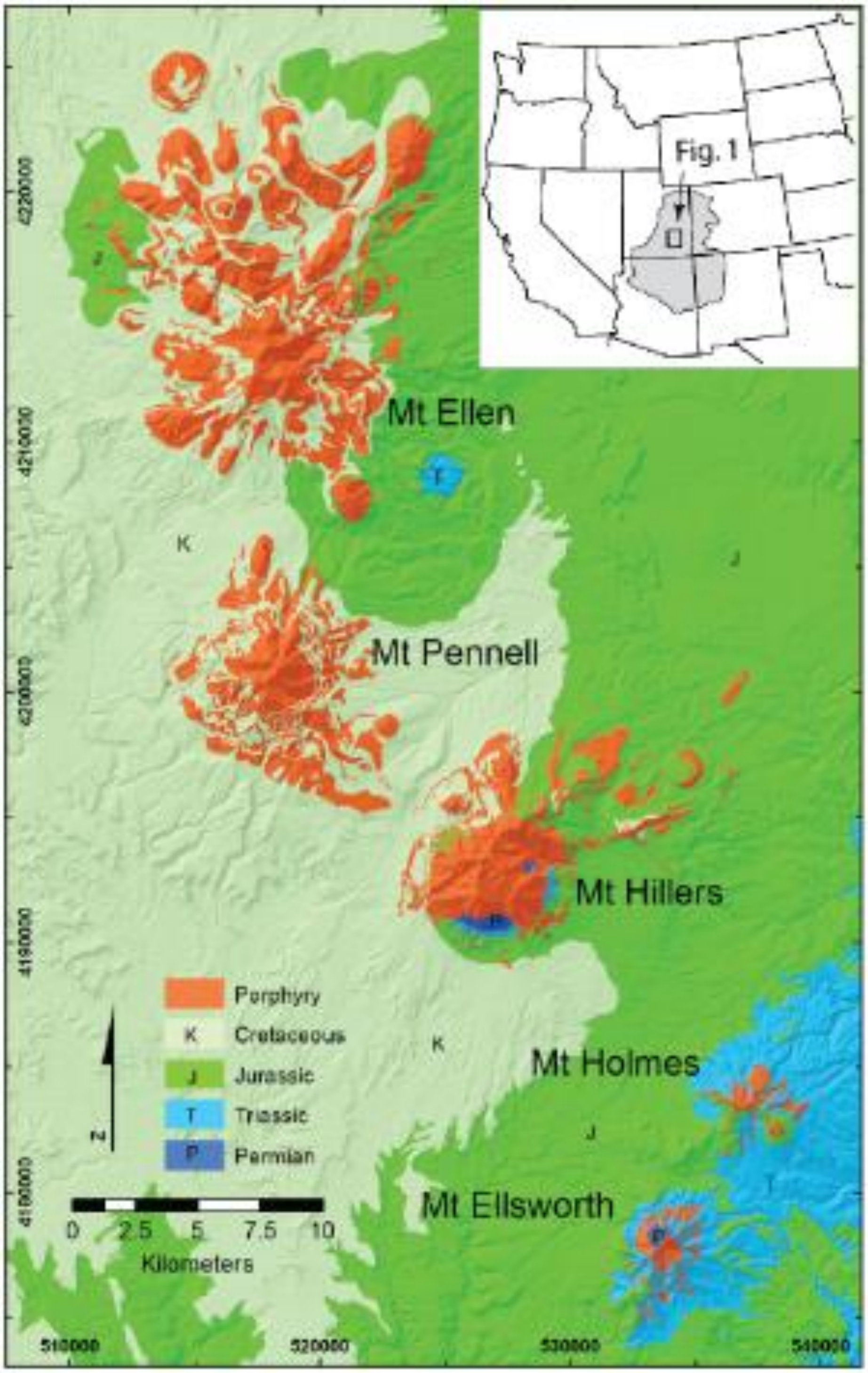

Figure 11. Geologic map of the five intrusive igneous centers of the Henry Mountains. From Horsman et al., 2018.

2.3.3 Mount Ellen

Mount Ellen is the largest of the five intrusive centers of the Henry Mountains (Figure 12) and is interpreted as a late stage in the development of a laccolithic intrusive center in the shallow crust (Horsman et al., 2018). Mount Ellen is a relatively large laccolith and evidence suggests that it is built from numerous component intrusions that have built up the laccolith over time (Maurer, 2015; Horsman et al., 2018; de Sousa, 2021) (Figure 13). These component intrusions are porphyritic andesite and generally asymmetric and tongue-shaped lobes that radiate out from the central body (Maurer, 2015; Horsman et al., 2018; de Sousa, 2021). The Copper Ridge Laccolith is one of these largest component intrusions comprising the Mount Ellen intrusive center and is located on the southeast side of Mount Ellen and is the focus of this study (Figure 12).

The total volume of the Mount Ellen intrusive center is estimated to be approximately 100 to 120 km^3 (Horsman et al., 2018) and it was intruded at approximately 28 Ma (Murray et al., 2016) based on U/Pb zircon analysis. Recent work by Paquette et al. (in review) suggests that the ~35 km^3 Mount Hillers intrusive center, another of the five intrusive centers of the Henry Mountains, was assembled at approximately 26 Ma over a period of ~250,000 years. Assuming a similar rate of magma injection for both Mount Hillers and Mount Ellen, the total duration for the assembly of Mount Ellen is estimated to be around 1 m.y., with a conservative upper limit at 2 m.y. (Figure 6).

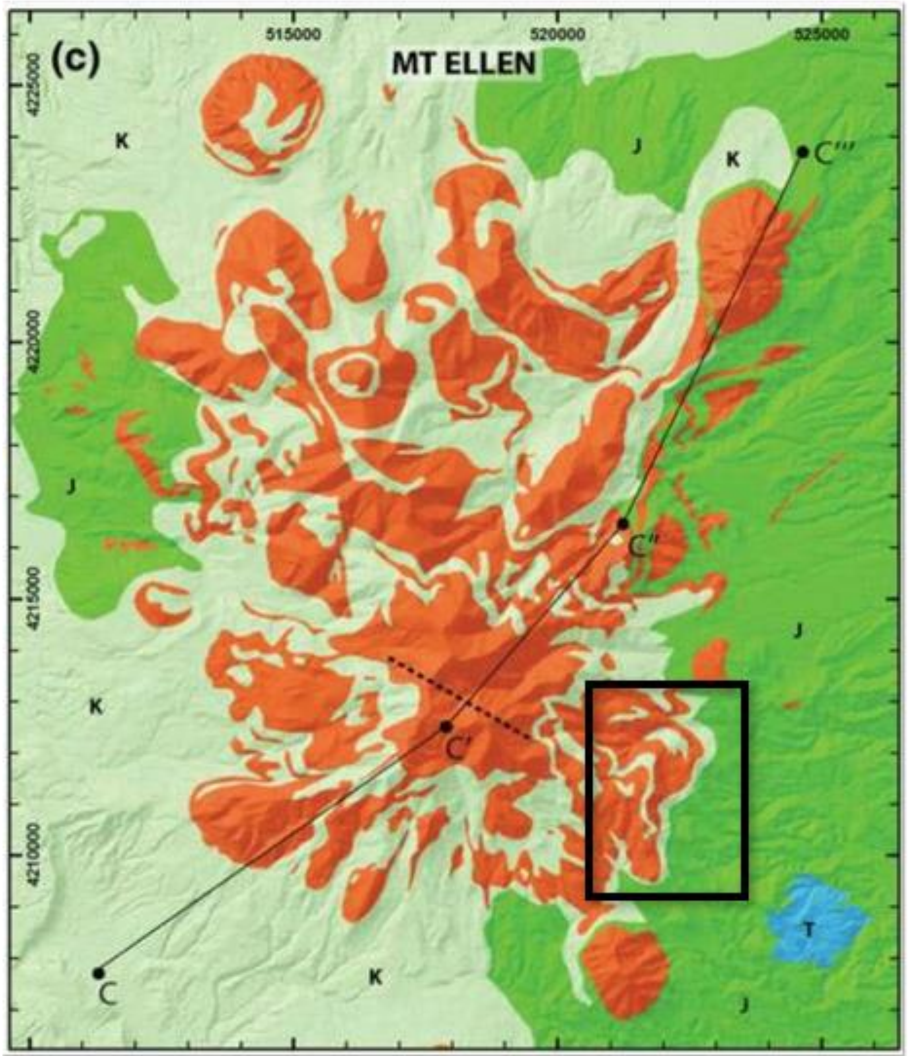

Figure 12. Geologic map of Mt. Ellen. Transect C-C''' corresponds with the cross-section in Figure 13. Red units are igneous porphyry, green units are sedimentary host rock. The black box indicates the location of the Copper Ridge Laccolith. Modified from Horsman et al., 2018.

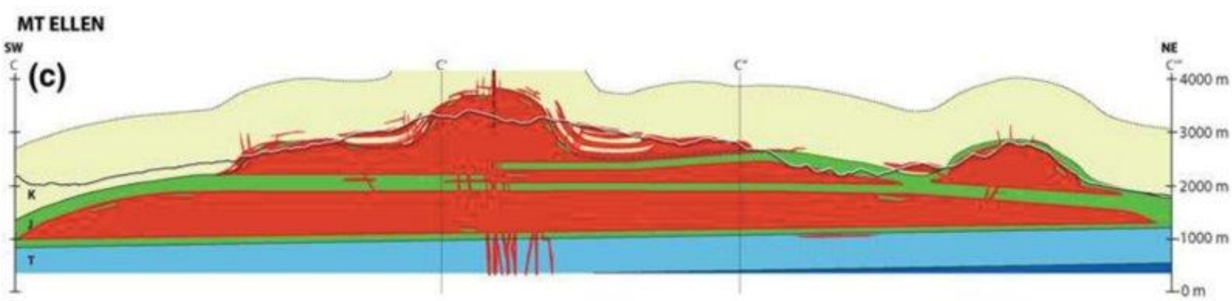

Figure 13. Geologic cross section of Mt. Ellen. From Horsman et al., 2018.

2.3.4 Copper Ridge Laccolith

The Copper Ridge Laccolith (CRL) is located on the eastern side of Mount Ellen and is an asymmetric, tongue-shaped lobe radiating off the main Mount Ellen intrusive center. The CRL has an estimated magma volume of about 2.9 km^3 (Figure 12) (Maurer, 2015). The CRL intrusion is well-exposed at the surface and features a complete natural cross-section (Figures 14 and 15) through the ~400 m thick igneous body (Maurer, 2015). Through the exposed CRL cross-section, a layer of Cretaceous Tununk shale approximately 25 m thick is preserved between two sections of igneous rock. Tununk shale is also locally exposed in several places atop the CRL. The Cretaceous Dakota sandstone is well exposed below the lower contact of the CRL. The upper section of igneous rock is about 80-100 m thick, whereas the lower portion is about 300-400 m thick (Figure 14) (Maurer, 2015; Horsman et al., 2018). The igneous rocks of the upper sheet generally contain larger phenocrysts compared to the lower sheet. In the upper sheet, plagioclase phenocrysts reach up to 14 mm, and hornblende phenocrysts up to 7 mm, while the lower sheet has plagioclase phenocrysts up to 8 mm and hornblende phenocrysts up to 4 mm (Maurer, 2015). Geochemical differences in both major and trace elements exist between the sheets, with consistent compositions within each sheet. The upper sheet exhibits a more mafic major element composition with lower SiO_2 and higher Fe_2O_3, MgO, and CaO. Interestingly, the upper sheet also has consistently higher abundances of incompatible elements such as Zr and rare earth elements (REE) (Maurer, 2015).

For this study, these two igneous sections will be termed the upper and lower “sheets.”

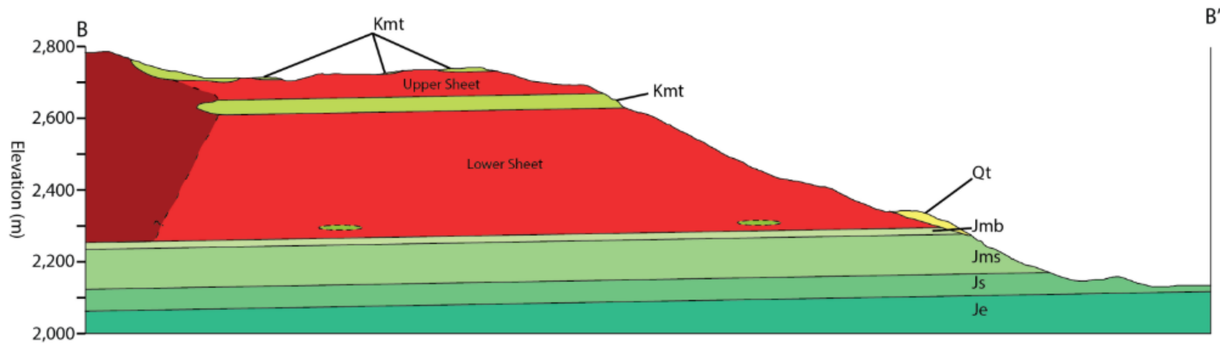

Figure 14. Geologic cross section of the Copper Ridge Laccolith with no vertical exaggeration. B-B' runs roughly east-west and transects the main ridge of the CRL. From Maurer, 2015.

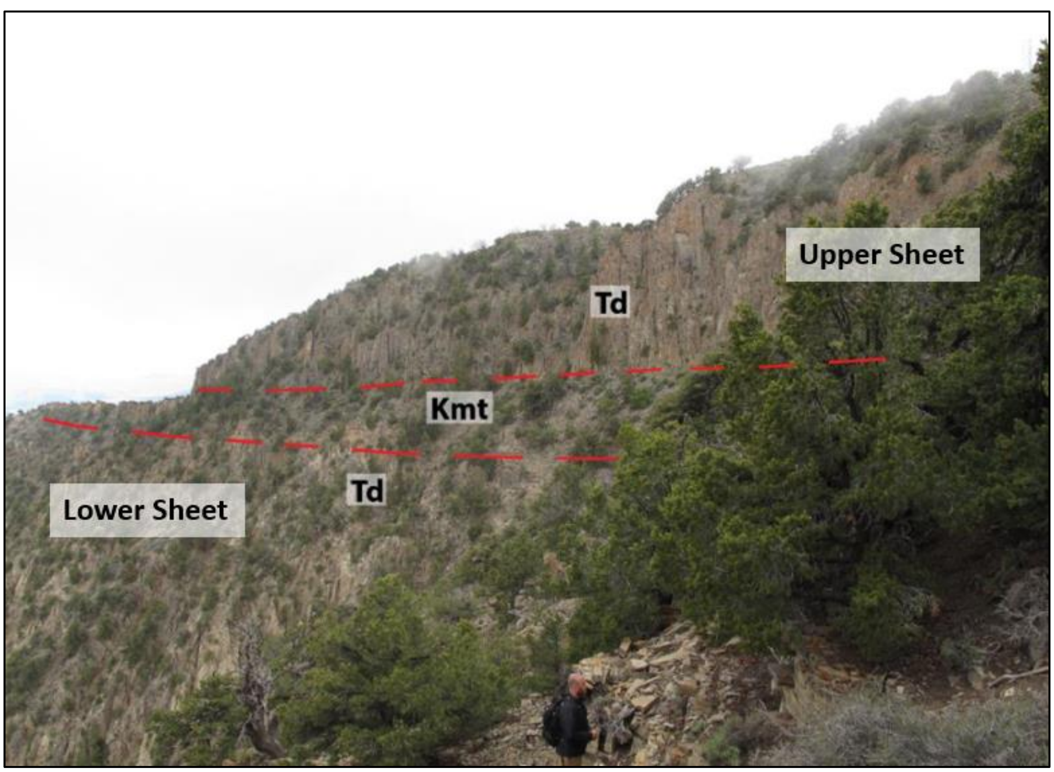

Figure 15. Photo showing a natural cross-section through the CRL, with the contacts between the Cretaceous Tununk shale (Kmt) and the igneous rocks (Td) marked by dashed red lines. The 80-100 m thick upper sheet and 300-400 m thick lower sheet are labeled. Modified from Maurer, 2015.

The phenocrysts (hornblende and plagioclase) in the porphyritic igneous rock likely grew in mid-crustal magma storage chambers or during initial magma ascent (Nelson and Davidson, 1993), but the groundmass crystallized very rapidly in the uppermost crust during the final phase of ascent and at the level of emplacement (Figure 16). Differences in groundmass CSD of these rocks should reflect distinct crystallization histories, with earlier injections cooling faster to produce small crystals and later injections cooling more slowly to produce larger crystals. Thus, studying the CSD of the groundmass of this laccolith will provide insight into the growth history of this shallow igneous system.

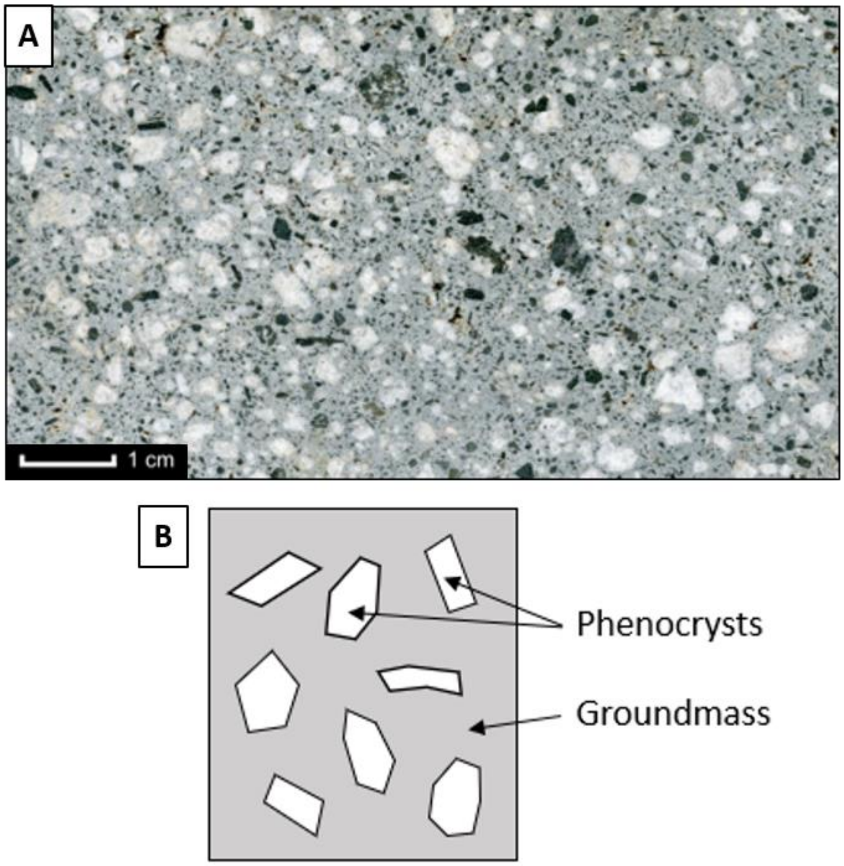

Figure 16. The porphyritic texture of the igneous rocks of the Copper Ridge Laccolith. A- Photograph of the plagioclase and hornblende phenocrysts (white and black crystals) and the fine-grained groundmass (grey matrix). B- schematic illustration of porphyritic texture.

3 Methods

A combination of fieldwork and analytical techniques was used to address the research questions for this study (Figure 17). Field work was conducted in the Henry Mountains, focusing on Mount Ellen and the Copper Ridge Laccolith to collect data on rock textures and to collect samples for analysis. Bulk magnetic susceptibility measurements were taken to assess the magnetic properties of the samples. Thin sections were prepared and analyzed. Electron microprobe analysis, along with scanning electron microscopy (SEM) and electron backscatter diffraction (EBSD) data were collected to map the spatial variation in elemental abundance and texture. Data were processed using ImageJ, CSD Corrections, and Microsoft Excel to analyze EBSD images and CSD. The resulting data allow for interpretations of how the Copper Ridge Laccolith was constructed over time from multiple component magma pulses.

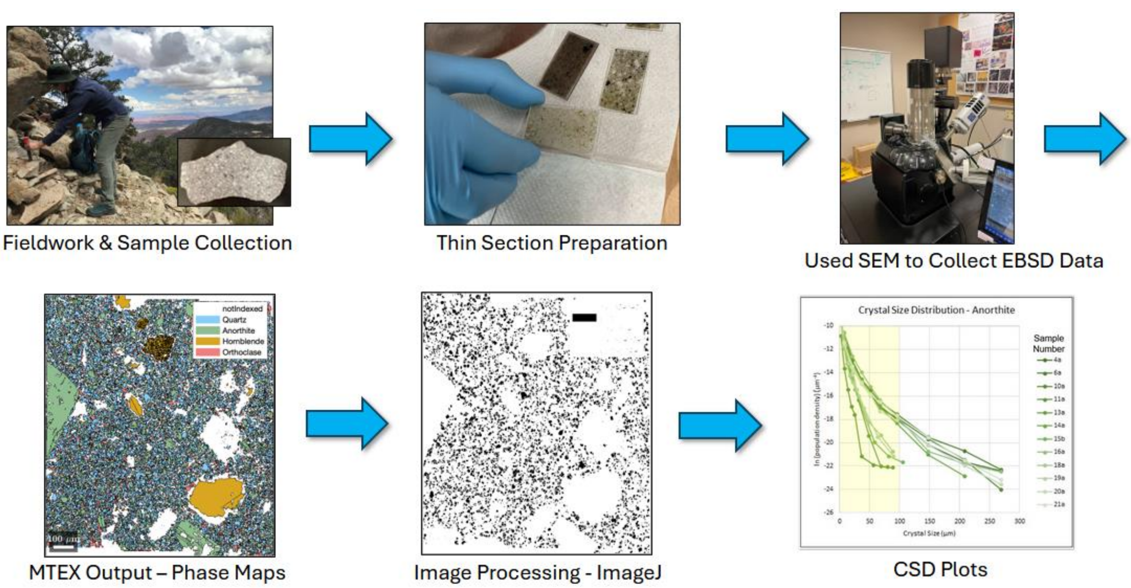

Figure 17. Workflow of the main methods used for this study.

3.1 Field Work

Fieldwork was performed in the Henry Mountains in south-central Utah on Mount Ellen and the Copper Ridge Laccolith in July 2022 (Figure 18). A suite of samples was collected from the north and south sides of the exposure, focusing on the upper and lower contacts of the sheets of the Copper Ridge Laccolith. Observations of the textures of the rocks at 12 stations throughout the CRL and surrounding rock units were recorded. GPS locations of each station were recorded using a Garmin GPS handheld device. Structural measurements such as strike and dip of host rock and the orientation of samples were taken using a Brunton geological compass. We collected 12 oriented rock samples of the igneous rock of the CRL (Figure 19). These samples are hereafter referred to as CR22 samples. A suite of previously collected samples were also used for this study (Braunagel, 2016) and are hereafter referred to as LN15 samples.

Figure 18. Sample collection on the Copper Ridge Laccolith.

Figure 19. The 12 igneous samples collected in order in preparation for transport.

3.2 Bulk Magnetic Susceptibility

Bulk magnetic susceptibility is measured by placing a sample in a magnetic field of known characteristics and observing how the sample becomes temporarily magnetized in the known field. The strength of the induced magnetic field is related to the mineralogy of the sample (Dunlop and Özdemir, 1997). In general, bulk magnetic susceptibility increases with a sample's iron content. In igneous rocks, initial magnetic mineralogy produced during crystallization can be changed by later alteration. Low-field bulk magnetic susceptibility was taken at various elevations throughout the upper and lower sheets of the CRL. Magnetic susceptibility is a unitless quantity, with results reported as SI units. For this study, magnetic susceptibility data were used to make interpretations about spatial variation of magnetic mineralogy throughout the cross-section of the CRL.

3.3 Thin Section Preparation and Analysis

The collected CR22 rock samples were cut into billets at East Carolina University (Figure 20) and sent to Grindstone Laboratories for polished thin section preparation for petrographic and EBSD analysis. Out of the 12 CR22 samples collected during fieldwork, 8 representative thin sections were chosen for EBSD analysis (Figure 19). The previously collected LN15 samples were also sent for polished thin section preparation (Figure 21).

Figure 20. Cutting CR22 hand samples into 1/2-inch thick billets.

Figure 21. LN15 sample preparation.

3.4 Electron Microprobe

Electron microprobe data were collected at Fayetteville State University for several samples using the JEOL JXA-8530F Hyperprobe Electron Probe Microanalyzer (EPMA) (Figure 22). Thin sections were coated with a thin layer (~5 nm) of carbon for analysis. Two primary types of data were collected: first, energy dispersive X-ray spectroscopy (EDS) maps showing the spatial variation in elemental abundance for a range of major and trace elements, and second, backscattered electron images, which provided detailed insights into the compositional and textural characteristics of the samples. Once elemental maps for key elements were obtained, image processing was performed to create maps of major mineral phases for crystal size distribution (CSD) analysis.

Figure 22. Electron microprobe used for data collection at Fayetteville State University.

3.5 SEM & EBSD Data Collection

Polished thin sections of the LN15 and the CR22 samples were used for SEM analysis. EBSD data were collected on a JEOL JSM-IT-300LV low vacuum SEM with EDS and EBSD capabilities at Appalachian State University, Boone, NC (Figure 23). EBSD patterns were collected on a NordlysNano camera and processed and indexed using Oxford Instruments AZTEC software. A step size of 2-3 µm was used for most of the areas analyzed. Additionally, a 0.2 µm step size was used for a detailed view of a small subset area of one sample that was also analyzed with a 2 µm step size. Utilizing the open-source MTEX toolbox for MATLAB, individual grains were constructed from raw EBSD data, including identification and correction for feldspar twins. A misorientation of 5 degrees was used to distinguish adjacent grains of the same composition. The resulting maps of mineral phases were used for all subsequent CSD analysis.

EBSD is a common method used to determine the crystallographic preferred orientation (CPO) of mineral crystals. For this study, EBSD data were obtained to make high-magnification phase maps of the mineral phases present in the groundmass of our samples. The generated phase maps use designated colors uniformly applied to all samples. The assigned colors are as follows: quartz (blue), plagioclase (green), orthoclase (red/pink), and hornblende (orange). CR22 samples have a slightly higher indexing rate compared to the LN15 samples.

Figure 23. Photo of the SEM with EBSD capabilities at Appalachian State University.

3.5.1 EBSD Phase Maps and CSD

EBSD phase maps are ideal for CSD analysis because they provide detailed objective information about rock microstructure with relatively little effort. The basis of backscatter diffraction is the interaction of an electron beam with a specimen in a SEM. The beam generates an omni-directional source of scattered electrons within the sample. The electrons diffract across all lattice planes simultaneously, and the backscattered electrons (BSE) that escape form a diffraction pattern, which is imaged on a phosphor screen (Prior et al., 1999).

Collected diffraction patterns reflect the crystallography of the analyzed spot of the sample. This diffraction pattern is compared by a crystallographic database and can identify both phase identification and crystallographic orientation. The resulting phase maps are ideal for CSD analysis because individual grains of each analyzed phase are easily distinguishable and outlined through subseqeuent processing with the MTEX software. The crystallographic preferred orientation data were not used for this study.

3.6 Data Processing

3.6.1 Grain Segmentation

The ImageJ computer application was used for image analysis and grain segmentation for this study. EBSD phase maps were opened in ImageJ and converted to grayscale. For each image, the threshold tool was used to isolate each phase present in the sample (quartz, anorthite, and orthoclase) (Figure 24). Hornblende was not analyzed due to its low abundance in the groundmass of these samples. The area of each grain of each phase was counted. The CSDCorrections plug-in in ImageJ was used to export the results to a file compatible with the CSDCorrections program (Higgins, 2000, 2002, 2006, 2011).

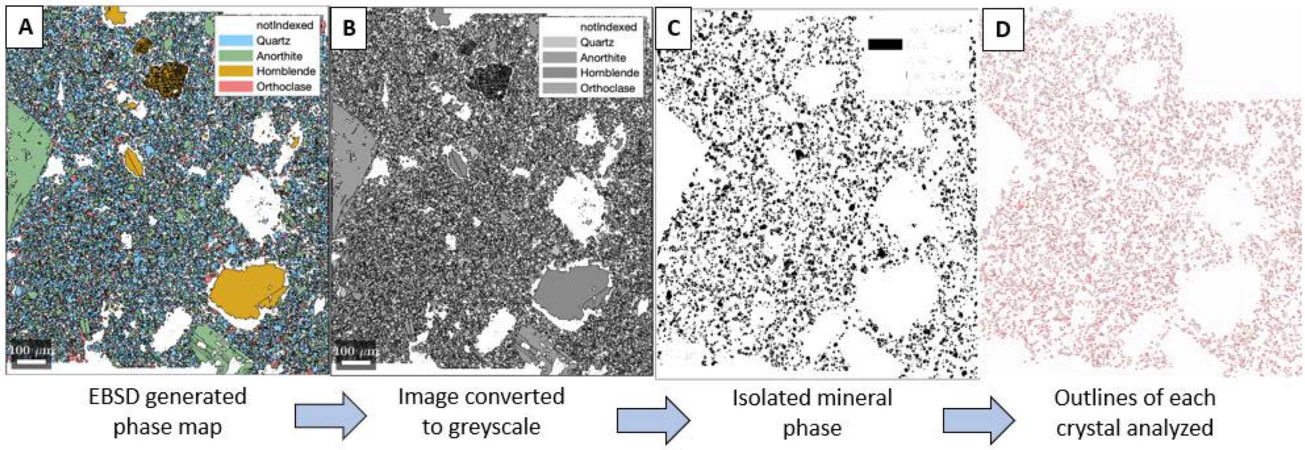

Figure 24. ImageJ workflow of taking the MTEX-generated EBSD phase map, isolating each mineral phase, and analyzing the size and shape of each crystal.

3.6.2 Textural Analysis

The program CSDCorrections is an indirect method for stereological calculations of CSD based on measurements of crystal shape outlines in thin sections, outcrops, and similar contexts. The methods of the program are detailed in Higgins (2000, 2002, 2006, 2011).

After analyzing the area of each identified crystal in ImageJ, the files are then opened in CSDCorrections (Figure 25). The “length” and “width” columns (Figure 25 Box 3) were copied from CSDCorrections and pasted into CSDSlice (Morgan and Jerram, 2006). CSDSlice calculated the shape factors used as the parameters in CSDCorrections (Figure 25 Box 1). The bin sizes used were 100, 80, 60, 40, 25, 20, 15, 10, and 5 square microns (Figure 25 Box 2). These bin sizes were selected in order to focus on the groundmass crystals, which were estimated to be less than 100 microns. The x, y, and z factors from CSDSlice correspond to the short, inter, and long boxes in CSDCorrections (Figure 25 Box 1).

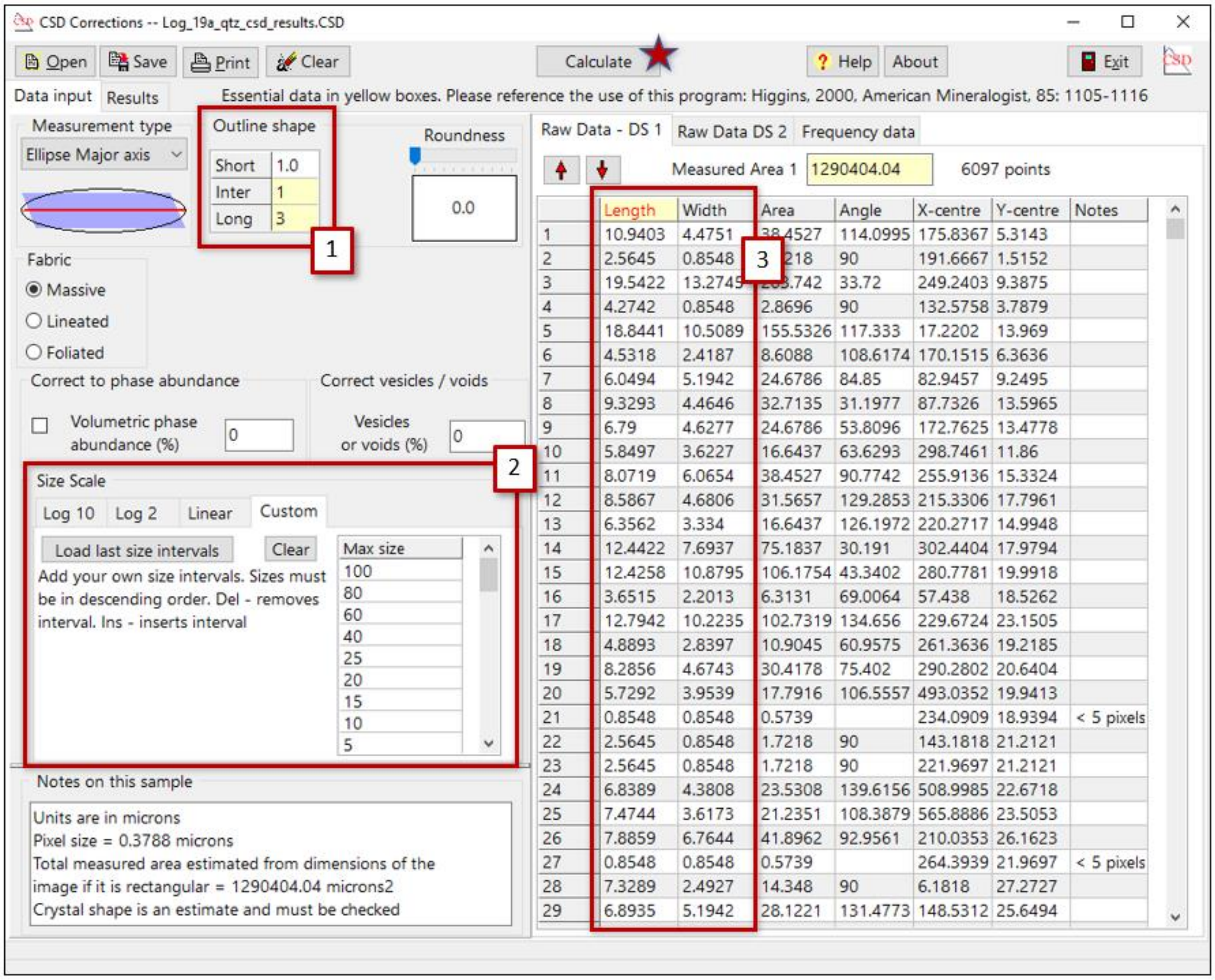

Figure 25. Modified screenshot of a typical CSDCorrections “Data input” page. Red boxes indicate areas of interest where settings were changed or columns that were used for analysis and are referenced in the text.

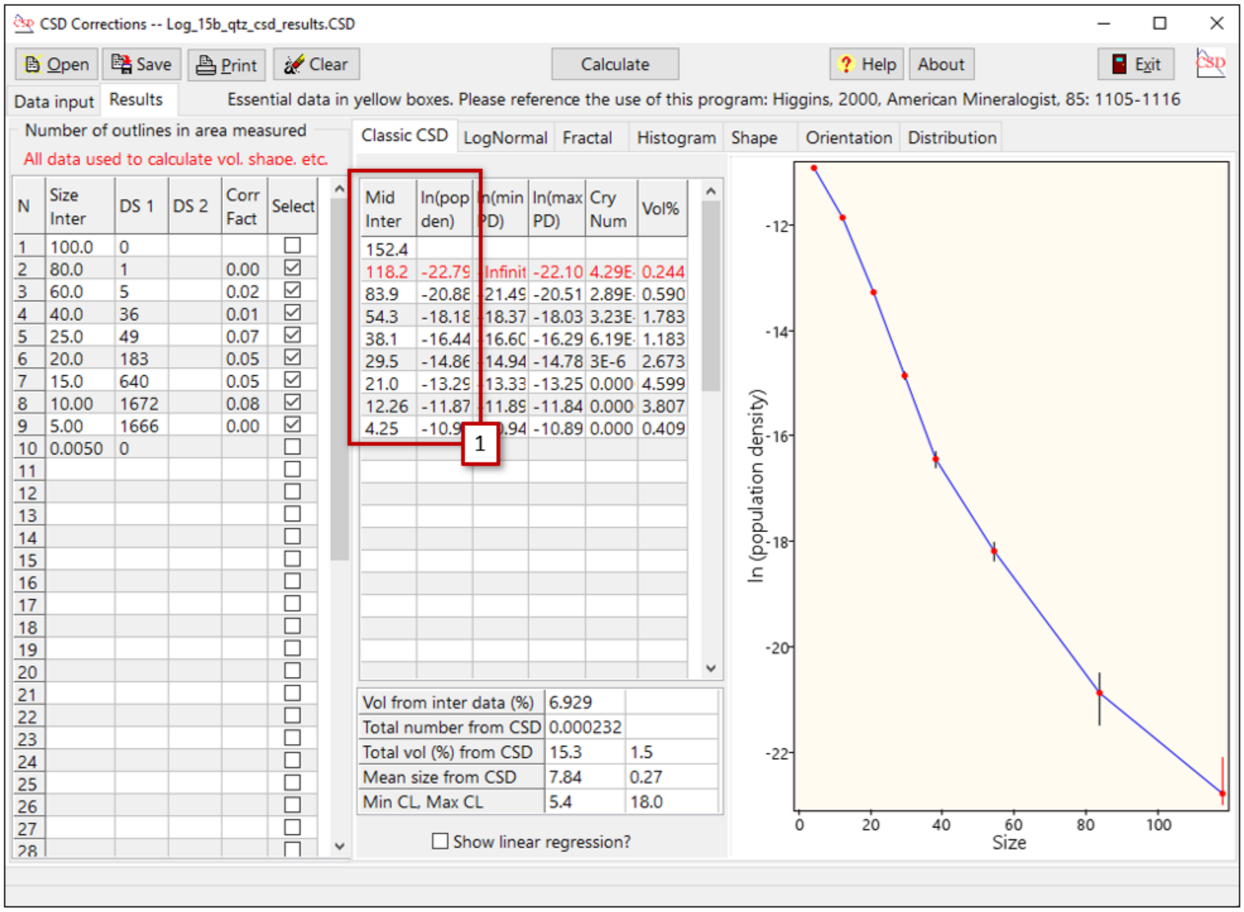

Figure 26. Modified screenshot of the "Results" page of CSDCorrections. Red box indicates the columns used for analysis and is referenced in the text.

3.6.3 Curve Fitting

Microsoft Excel was used for additional data processing and calculations. Traditional CSD plots were created in Excel using the "Mid Inter" and "ln(pop den)" columns (Figure 26 Box 1) from the results of the CSDCorrections calculations. Population density is plotted on the y-axis, and the crystal size bin on the x-axis.

To create plots similar to those of Zieg and Marsh (2012), which display the elevation and population density of a range of pre-determined crystal sizes for each sample, Microsoft

Excel was used. To accomplish this, interpolation of output from CSDCorrections was required because crystal size bins vary between samples. First, a polynomial trendline was fitted to the CSD data output from CSDCorrections for each mineral phase of each sample (Appendix B). A polynomial trendline allows for the capturing of some curvature and 2^{nd}, 3^{rd}, and 4^{th} order polynomials were selected based on visual inspection of best fit to the CSD data. No attempt was made to quantify the error or misfit of the curve to the data. Using the equation that describes the trendline, the population density for each pre-determined crystal bin size for each mineral phase was calculated. By inputting the pre-determined bin size (x) into the equation, the corresponding population density (y) was obtained. Finally, the population density values were plotted against the elevation of each sample.

4 Results

4.1 Field Work and Sample Collection

Field observations and samples were collected to provide comprehensive coverage of the upper and lower sheets of the CRL (Figures 27 and 28) (Table 1). Observations included rock compositions, textures, and the contacts between igneous intrusions and surrounding sedimentary host rock. CR22 samples were taken from the upper and lower contacts of both sheets on the northern and southern sides of the CRL exposure. Additionally, LN15 samples, collected by Braunagel and others in 2015 (Braunagel, 2016), were borrowed for this study. The combined CR22 and LN15 samples provide a complete cross-sectional representation, allowing for the analysis of elevation variation in the crystal sizes of the groundmass within the CRL.

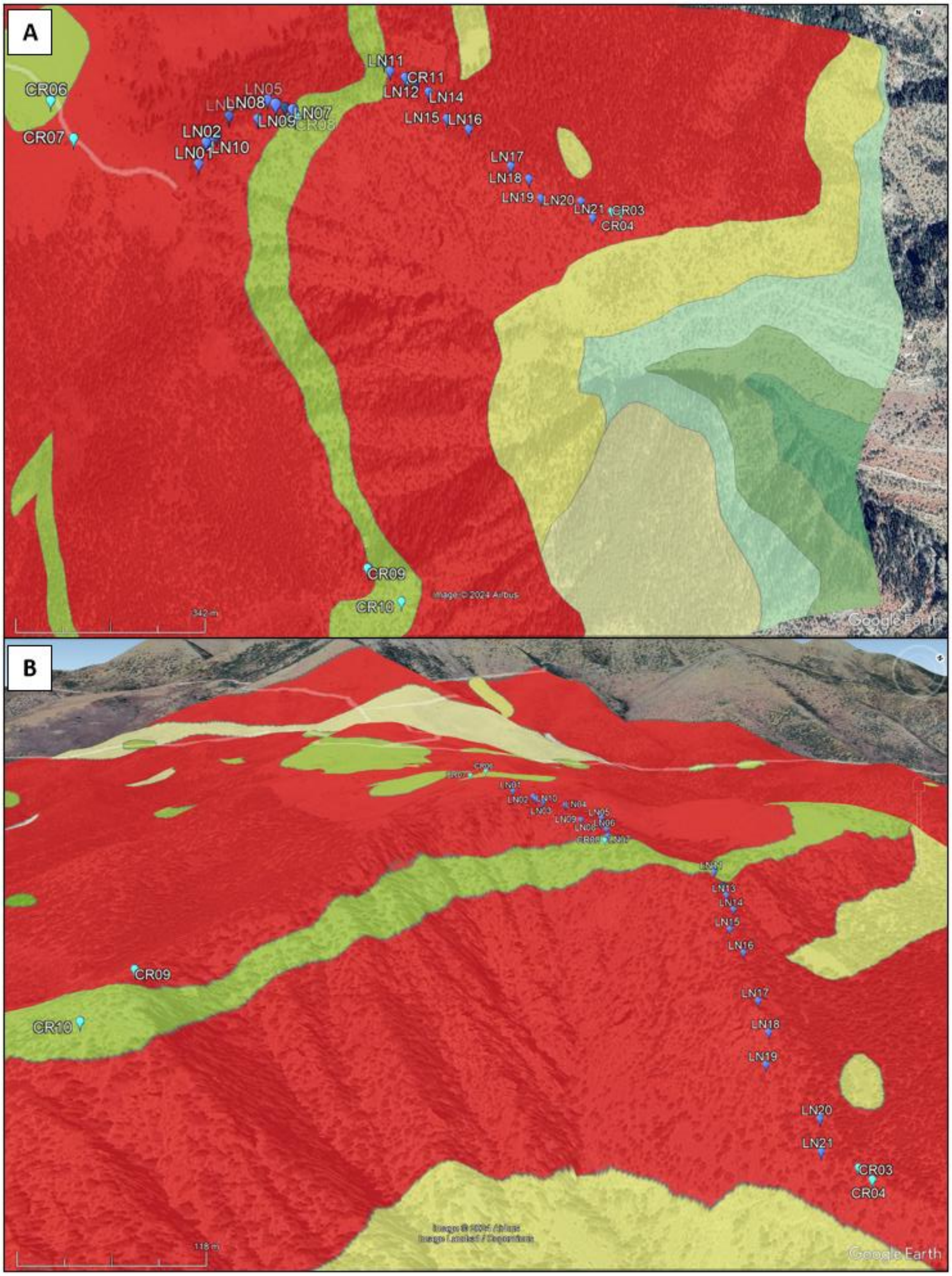

Figure 27. Locations of CR22 and LN15 samples overlain on a geologic map (Maurer, 2015). A- Top-down view of the study area. B- Looking at the CRL from the east.

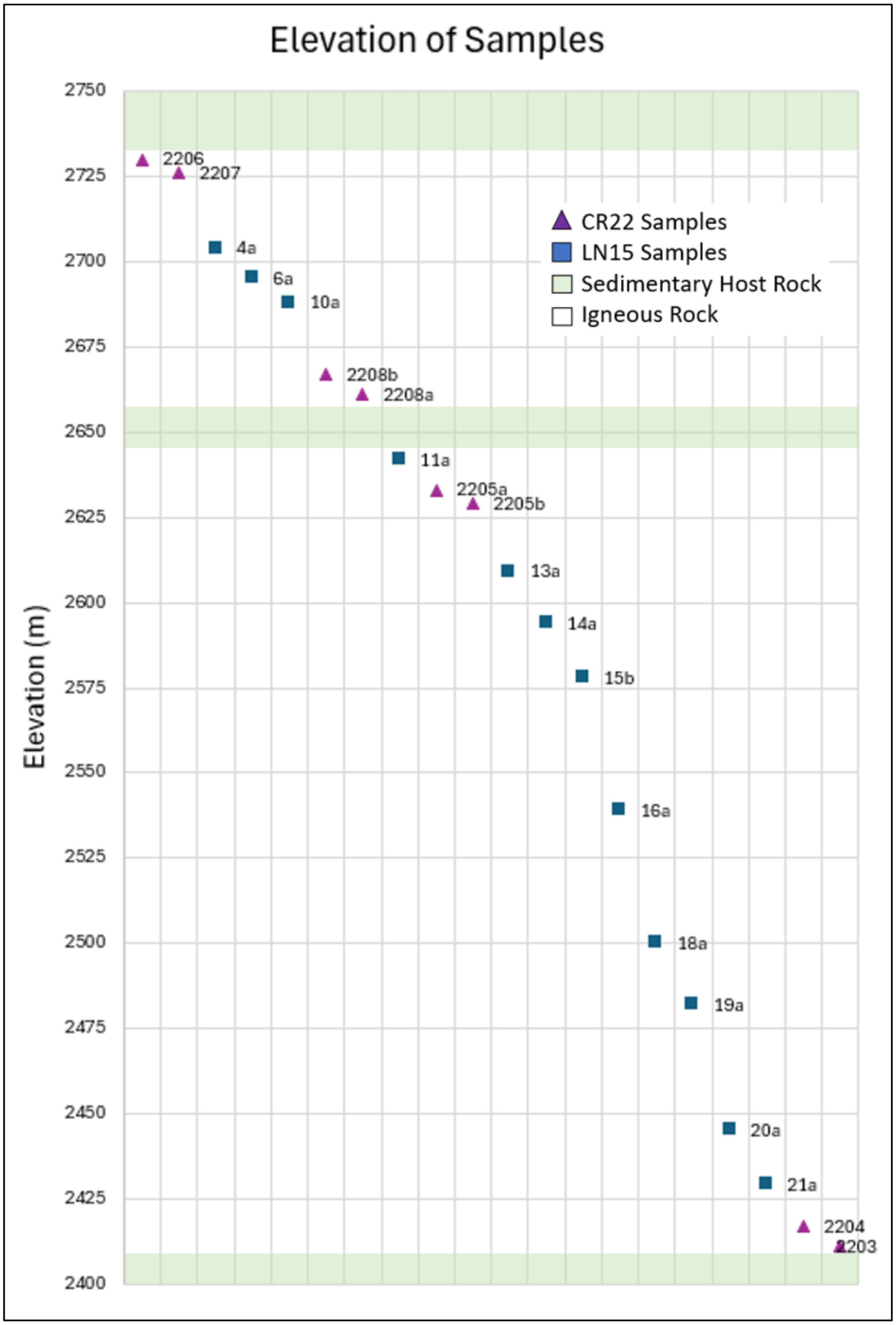

Figure 28. Chart showing elevations of each sample (CR22 and LN15 samples) used for this study.

Table 1. UTM coordinates and elevation for all samples used in this study. All coordinates in UTM zone 12 with datum NAD83.

	Sample #	Elevation (m)	Easting	Northing
Upper Sheet	CR2206	2730	521492	4211150
	CR2207	2726	521523	4211099
	LN15_4a	2704	521728	4211139
	LN15_6a	2695	521800	4211159
	LN15_10a	2688	521705	4211101
	CR2208b	2667	521812	4211146
	CR2208a	2661	521812	4211146
Lower Sheet	LN15_11a	2642	521947	4211227
	CR2205a	2633	521938	4211240
	CR2205b	2629	521938	4211240
	LN15_13a	2609	521983	4211214
	LN15_14a	2594	522003	4211207
	LN15_15b	2578	522031	4211170
	LN15_16a	2539	522065	4211159
	LN15_18a	2500	522165	4211091
	LN15_19a	2482	522187	4211063
	LN15_20a	2445	522259	4211064
	LN15_21a	2429	522282	4211038
	CR2204	2417	522333	4211047
	CR2203	2411	522316	4211050

4.2 Bulk Magnetic Susceptibility

Bulk magnetic susceptibility results range from a minimum of 9.59×10^{-4} SI to a maximum of 3.2×10^{-2} SI throughout the CRL. In both the upper and lower sheets of the CRL, a general pattern is apparent with lower magnetic susceptibility toward the top and bottom of each sheet and a higher magnetic susceptibility toward the middle of the sheets (Figure 29). This pattern is more pronounced in the lower sheet but is still visible in the upper sheet. A higher magnetic susceptibility reading indicates a greater abundance of ferromagnetic minerals such as titanomagnetite.

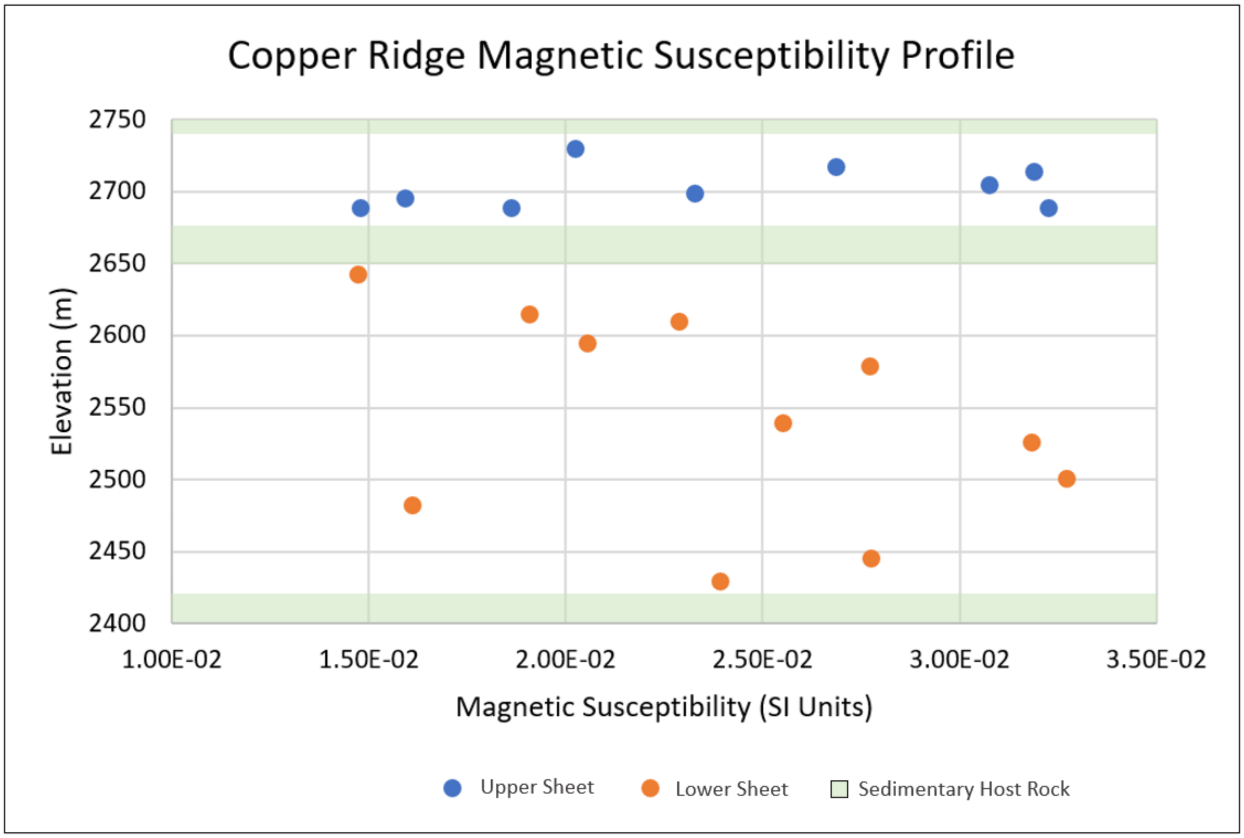

Figure 29. Magnetic susceptibility profile throughout the CRL. Blue circles indicate samples in the upper sheet, orange indicates lower sheet samples.

4.3 Electron Microprobe

A method was tested using electron microprobe chemical image maps from energy-dispersive spectroscopy (EDS) to create mineral phase maps for crystal size distribution (CSD) analysis. The microprobe images depict spatial variation of individual chemical element abundance. To make maps of mineral phases, EDS maps of elements were combined using Adobe Illustrator software (Figure 30). Elemental maps for Ca and Ca+Na to identify anorthite, Fe for hornblende, K for orthoclase, and Si for quartz were used. By layering these images in Adobe Illustrator, phase maps were generated with approximately 85% indexing, indicating the percentage of the image with chemistry consistent with anorthite, hornblende, orthoclase, or quartz (Figure 30). The resulting images were not well suited for CSD analysis because adjacent crystals of the same mineral were often indistinguishable, leading to potential skewing of CSD results towards inaccurately large crystal sizes.

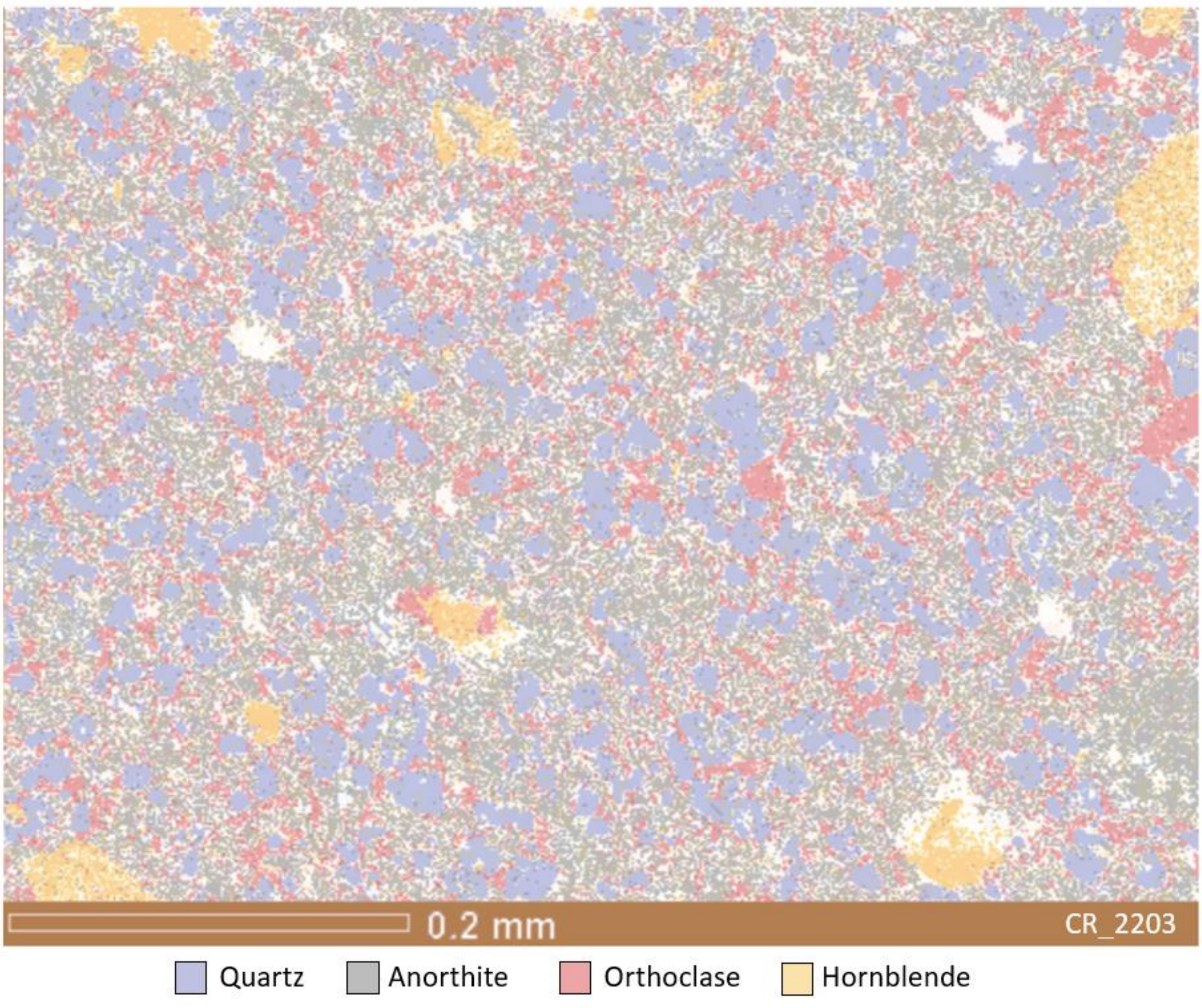

Figure 30. Phase map generated from microprobe chemical data.

Additionally, high magnification (1,000x) backscattered electron (BSE) images were taken to observe the texture of the groundmass (Figure 31). These BSE images revealed a network of interconnected groundmass crystals ranging in size from less than 2 µm to approximately 20 µm.

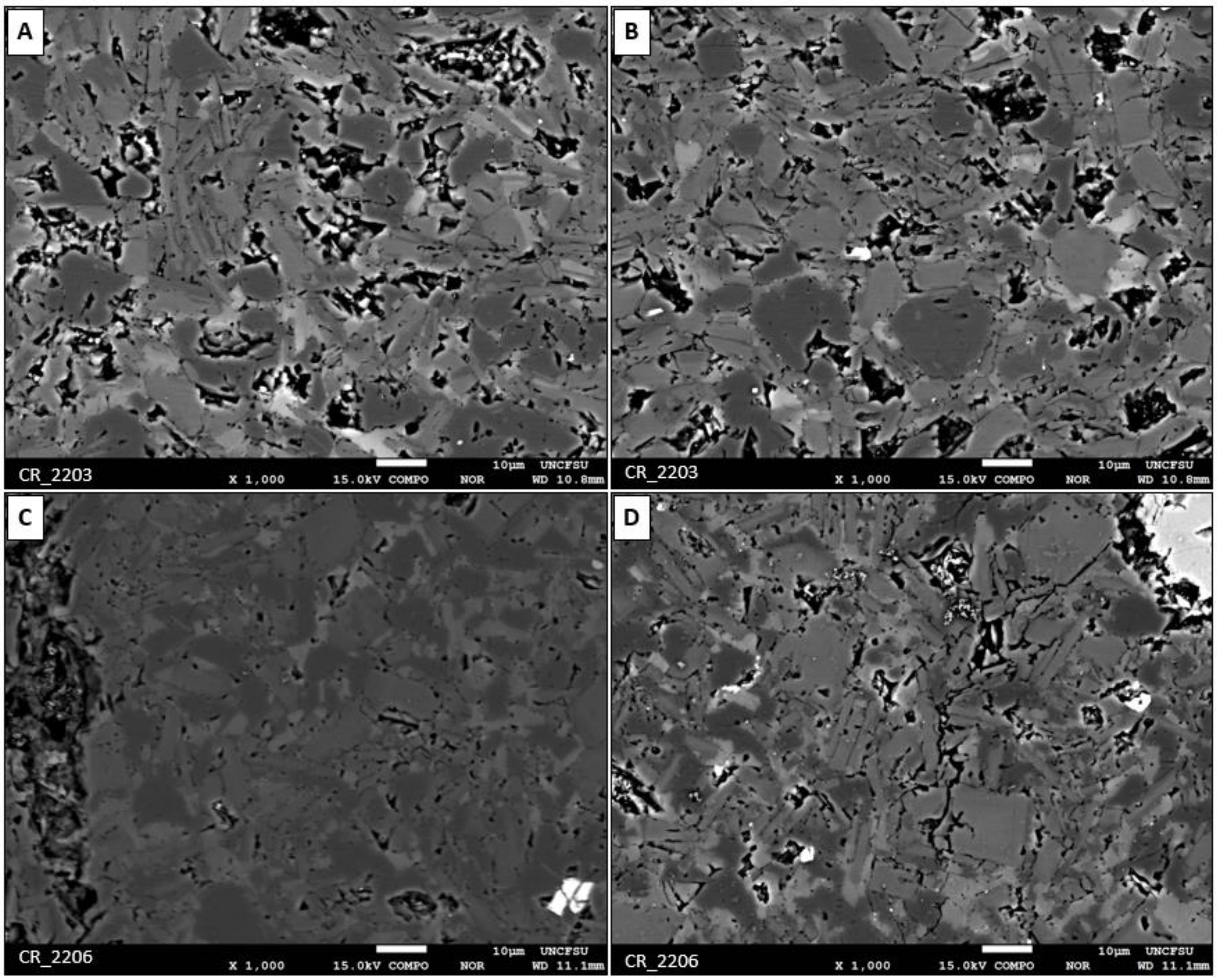

Figure 31. High magnification (x 1,000) backscattered electron image of samples 2203 (A and B) and 2206 (C and D) showing detailed groundmass texture.

4.4 SEM and EBSD Data

EBSD data were used to create color-coded phase maps of the thin sections (Figure 32). A step size of 2-3 μm was used for these phase maps. The phase maps show coarser-grained phenocrysts surrounded by the finer-grained groundmass. All images used for ImageJ processing and CSD analysis are found in Appendix C.

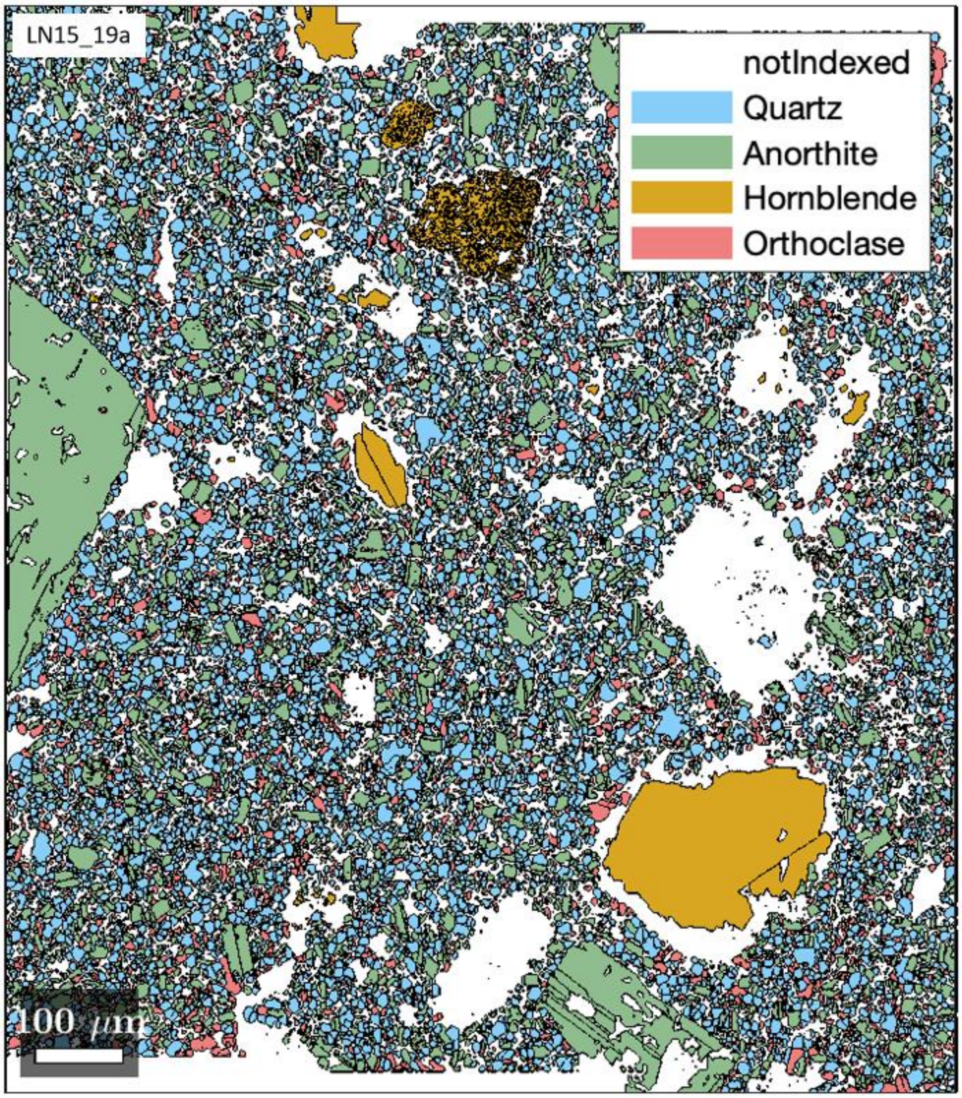

Figure 32. EBSD phase map of sample LN15_19a color-coded by mineral phase.

To better understand the details of groundmass texture, an EBSD map (Figure 33) was made with a finer step size of 0.2 µm. In Figure 33, adjacent grains within regions of the same mineralogy are clear because this image combines mineralogy (color) with EBSD data quality information (band contrast, indicated in grayscale from poor in black to good in white). Good examples of adjacent grains are especially clear for anorthite (labeled bytownite). This detailed map provides useful information about the finest crystals present in this sample for different mineral phases. The finest quartz crystals appear to be 1-2 µm across, although most are larger. The finest bytownite crystals are 2-4 µm and most bytownite crystals are relatively elongate. The finest orthoclase crystals appear 2-4 µm and most crystals are more equant than anorthite/bytownite. Hornblende is the least abundant mineral in the groundmass of all studied samples and only appears as a few pixels (<1%) in this area of this sample.

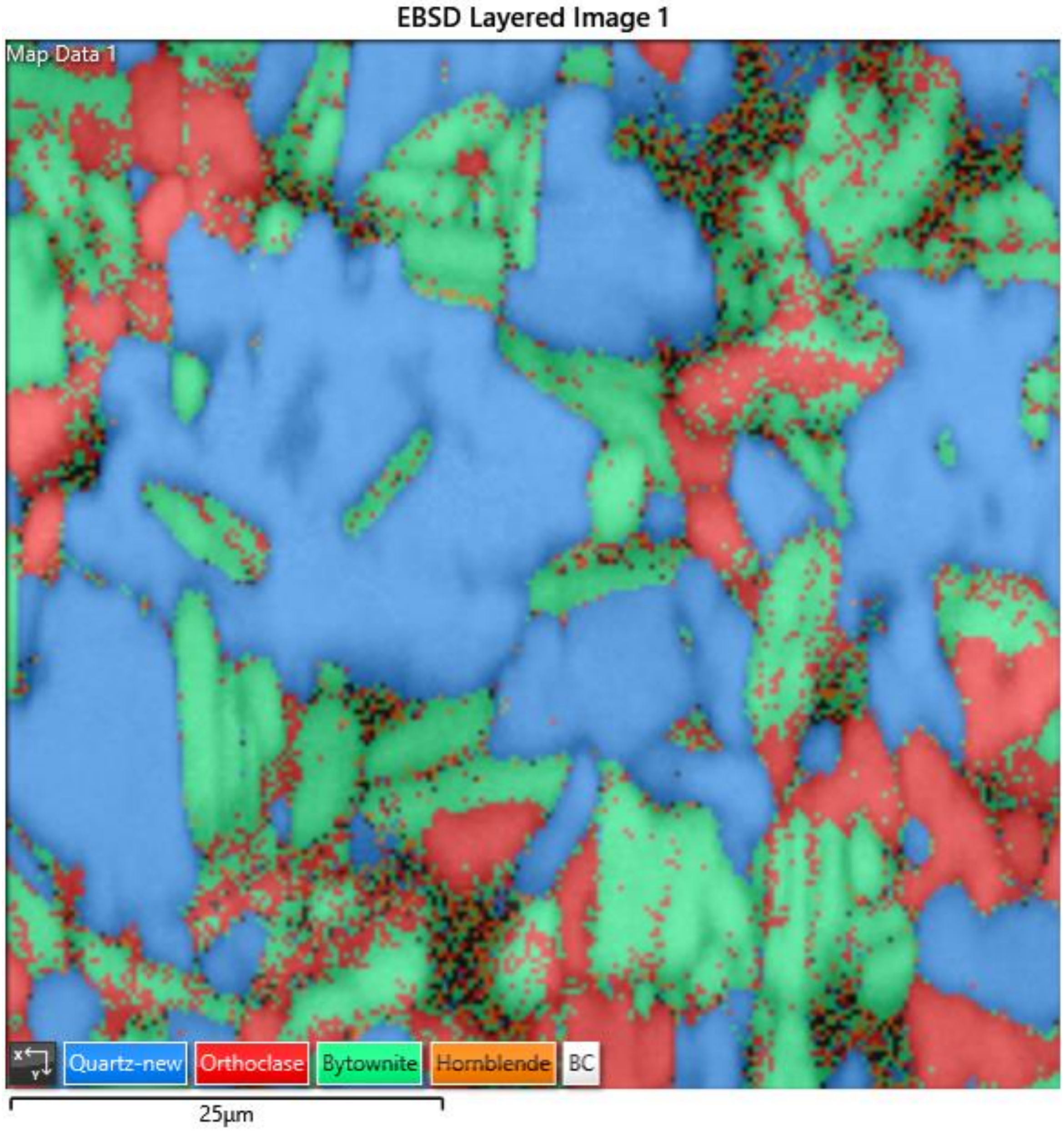

Figure 33. High-resolution image of sample CR_2208b, created with a 0.2 µm step size. Colors indicate the indexed mineral phase, and the underlying grayscale band contrast (BC) image indicates the quality of EBSD indexing, with good quality as light / white and poor quality as dark / black.

4.5 Crystal Size Distribution Results

CSD results (Appendix A) for both CR22 and LN15 samples were used to quantify the textural differences of the groundmass throughout the upper and lower sheets of the CRL. For this study, groundmass crystals are defined as those less than 100 µm in size, and the analysis of this study focuses on groundmass crystals within this size range. CSD results are displayed as traditional CSD plots for each phase of each sample (section 4.5.1), a comparison of CSD of each mineral phase near the margins (section 4.5.2), and as a comparison of each phase of the CSD variation at various elevations throughout the CRL (section 4.5.3).

4.5.1 Traditional CSD Plots

Traditional CSD plots show the relationship of the natural log of the population density of the crystals on the y-axis versus the size of the crystals on the x-axis. Figures 34 and 35 show traditional CSD plots exhibiting the expected negative sloping curve. The curves for each mineral phase in various samples throughout the CRL have different slopes and shapes (some more curved versus some straighter). Sampled at regular intervals throughout the CRL cross-section, the LN15 samples (Figure 34 A, B, C) display a wider range of crystal sizes and some samples have a more shallow, curved slope. The LN15 samples also show two distinct populations, (1) a population of steeper, straighter slopes, and (2) another population of shallower and more curved slopes. The CR22 samples (Figure 34 C, D, F) were collected at the top and bottom margins of each sheet and show relatively steeper and straighter curves with fewer larger crystals.

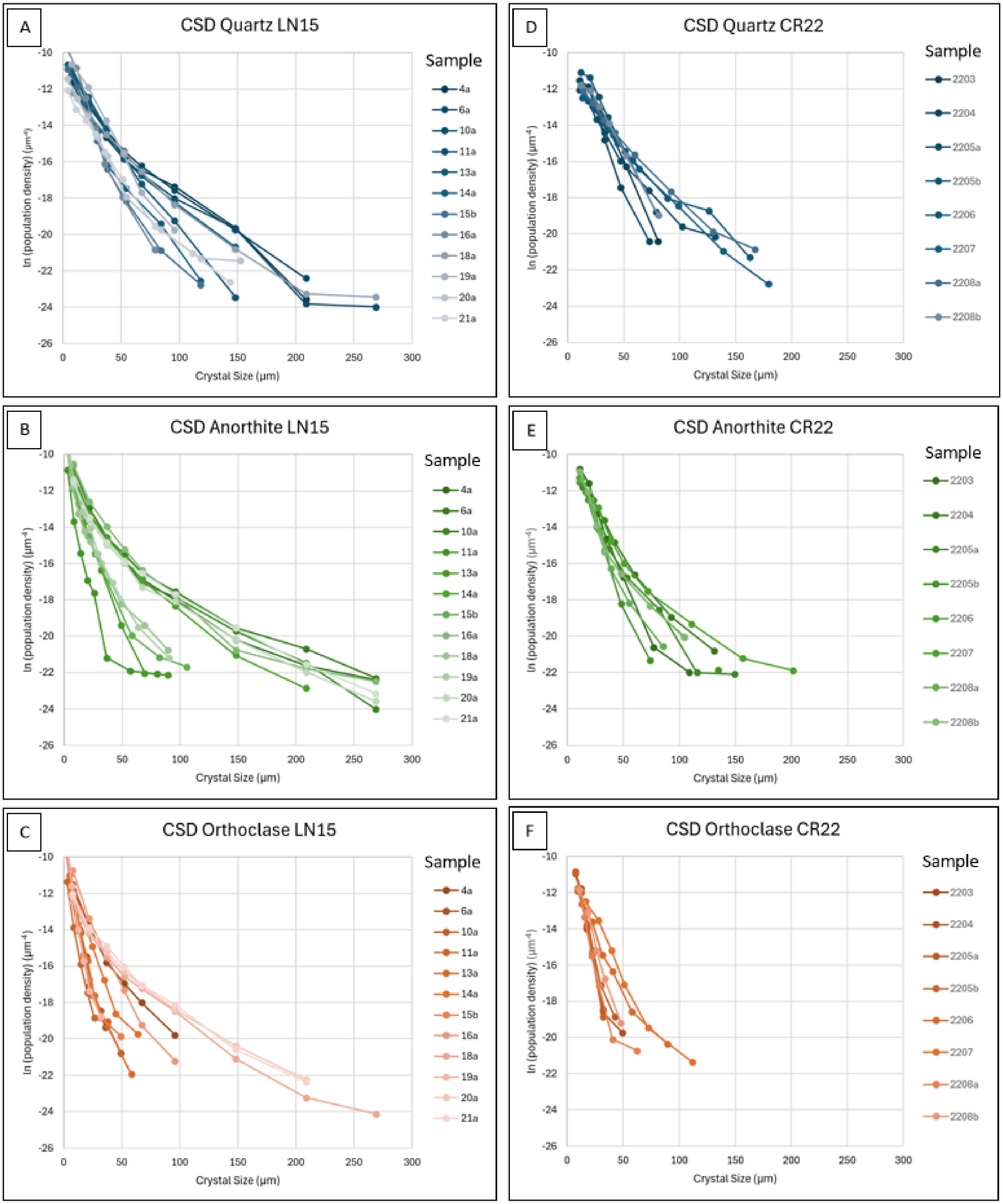

Figure 34. CSD of quartz (A and D), anorthite (B and E), and orthoclase (C and F) for CR22 and LN15 samples for the upper and lower sheets of the CRL. CR22 samples focused on the margins of each sheet and LN15 samples were collected at regular intervals throughout the cross-section. Each line represents one sample.

Figure 35 shows the CSDs comparing the upper and lower sheets of the CRL for crystals up to 300 µm. The upper sheet (Figure 35 A, B, C) shows generally more shallow and curved slopes. Comparing results from both sheets, the lower sheet (Figure 35 D, E, F) is more texturally homogeneous, while the upper sheet (Figure A, B, C) displays more textural variability, ranging from relatively straight and finer-grained CSDs to concave up, coarser-grained CSDs. The CSD curves for quartz in the upper sheet (Figure 35 A) generally show a shallower slope than those in the lower sheet. The CSD curves for quartz in the lower sheet (Figure 35 D) show a wider spread among the curves with some having a straighter and steeper slope, with other samples having a shallow and more curved slope. The CSD curves for anorthite in the upper sheet (Figure 35 B) display a pattern similar to that of quartz, with a generally shallow and curved slope. For anorthite in the lower sheet (Figure 35 E), there is also a wider spread with two crystal populations, (1) a population of samples with a steep and straight slope and (2) a population with shallower curved slopes. The CSD curves for orthoclase in the upper sheet (Figure 35 C) have more samples with a shallower slope than those in the lower sheet. For orthoclase in the lower sheet (Figure 35 F), several samples show a shallow curve with larger crystals but in general, orthoclase in the lower sheet has smaller crystals and steep and straight slopes.

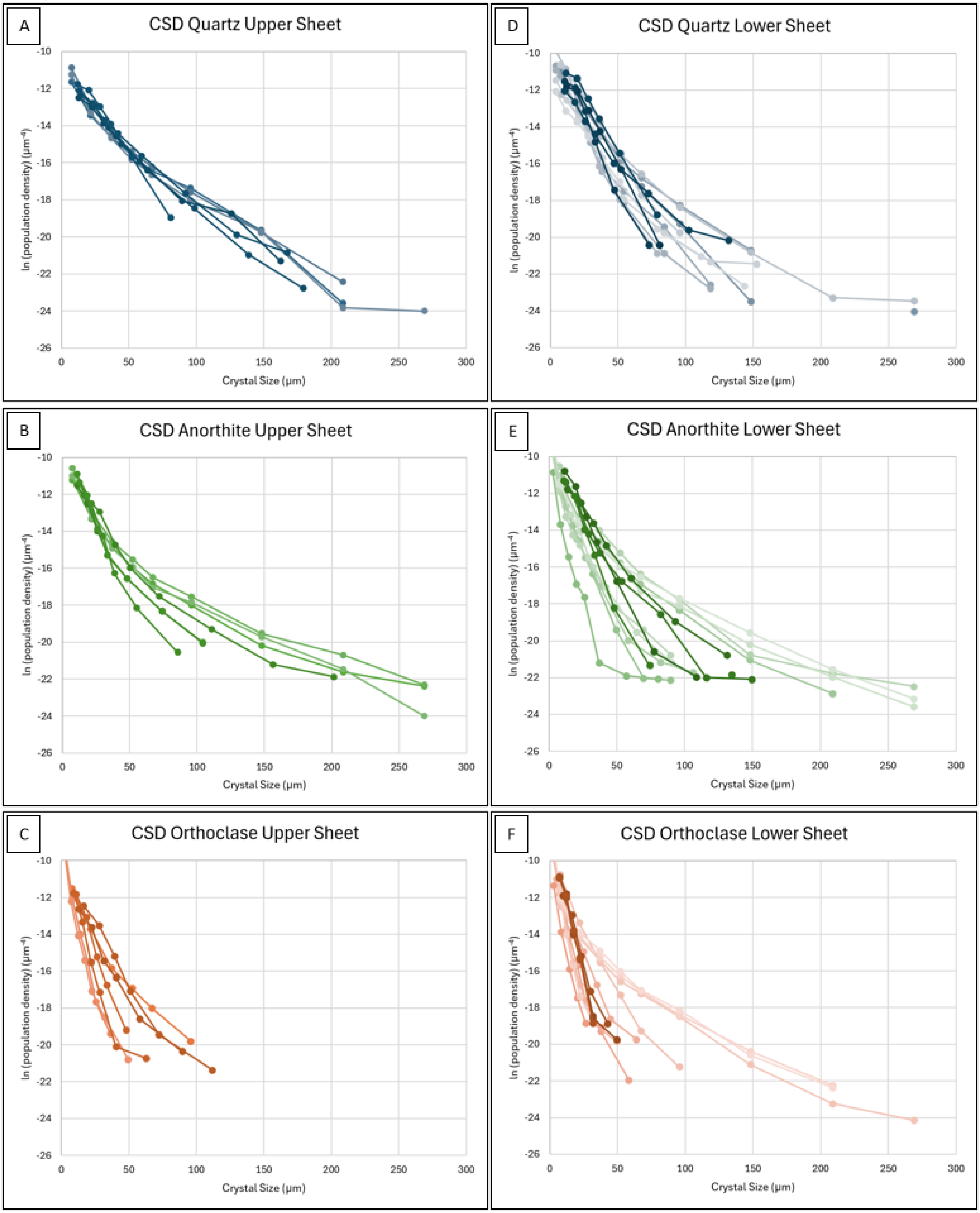

Figure 35. CSD for quartz (A and D), anorthite (B and E), and orthoclase (C and F) for CR22 and LN15 samples the upper and lower sheets of the CRL. Each line represents one sample.

4.5.2 Comparing CSD Plots Close to the Margins

At each contact between CRL igneous rock and host rock, one sample was taken a few centimeters from the contacts, and another sample was taken 3-5 m inward from the contact (Figures 36 and 37). This provides a test for a difference of the CSD right at the contact versus a few meters inward. We would expect to see finer-grained groundmass closest to the margins due to assumed faster cooling. The CSD data for samples from the upper igneous sheet are shown in Figure 36 and CSD data for samples from the lower igneous sheet are shown in Figure 37. In both these figures, samples near the contact are shown in dark colors with solid lines connecting data points, and samples farther from the contact are shown in lighter color with dashed lines.

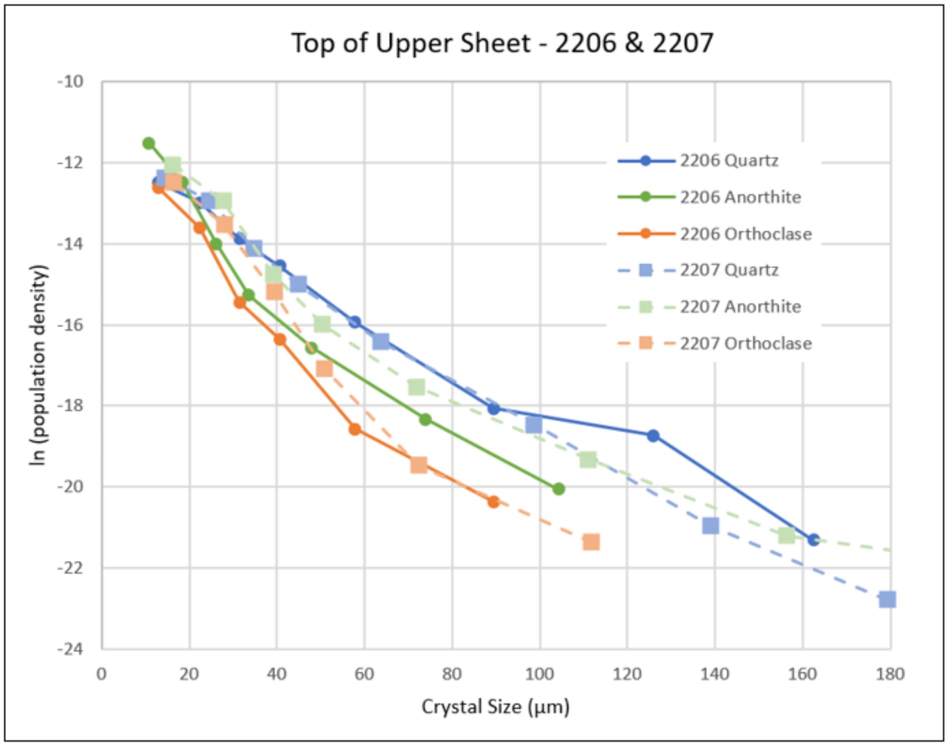

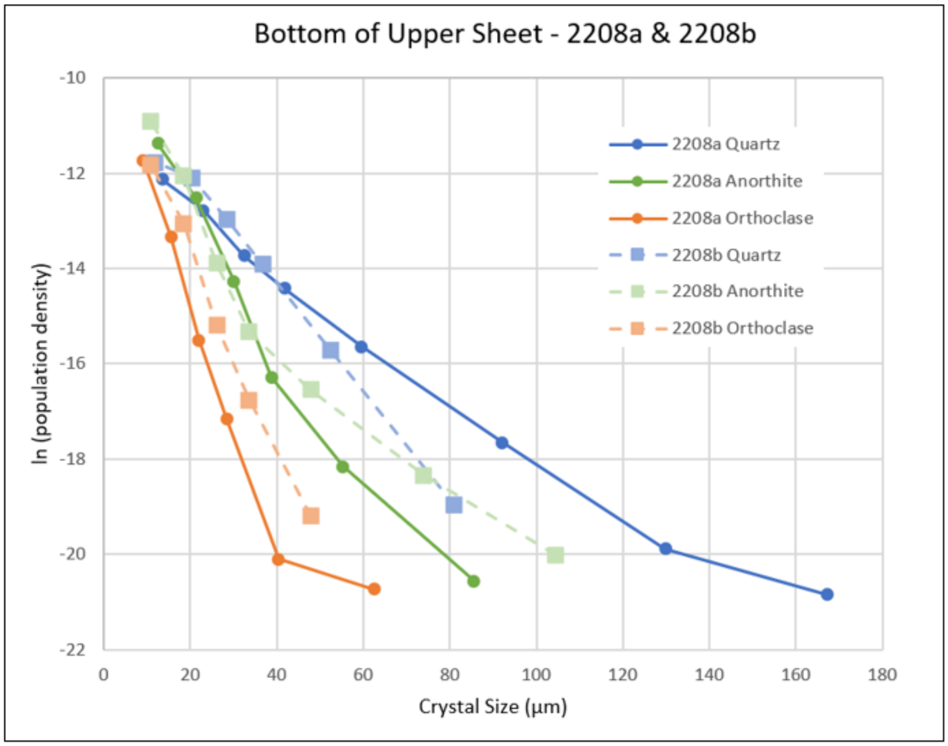

Figure 36. CSDs of CR22 samples taken near the top and bottom contact between the upper igneous sheet of the CRL and the surrounding sedimentary host rock. Darker colored lines with circles are from the sample close to the contact (within a few centimeters). Lighter, dashed lines with squares are from the samples several meters inward.

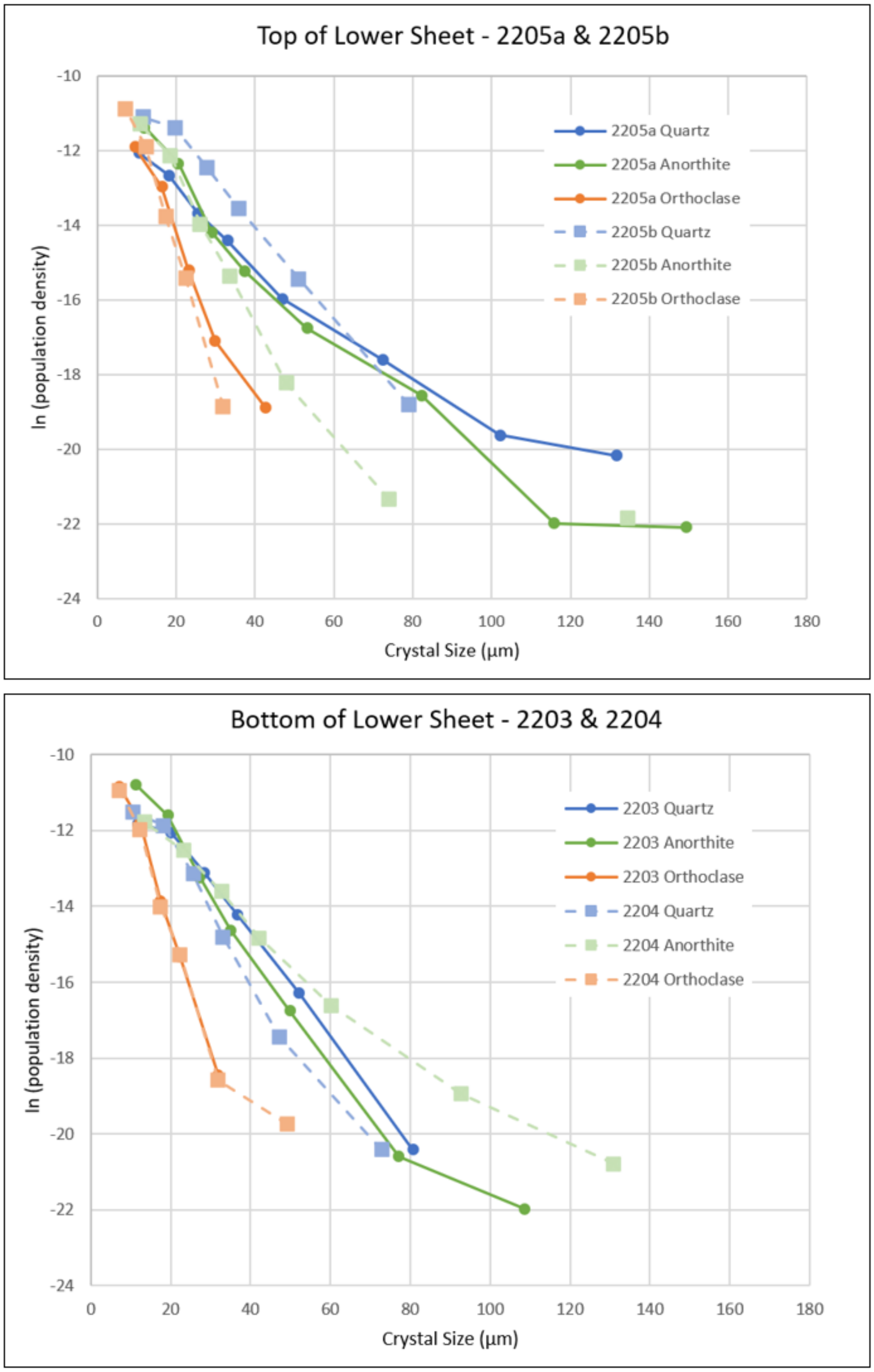

Figure 37. CSDs of CR22 samples taken near the top and bottom contact between the lower igneous sheet of the CRL and the surrounding sedimentary host rock. Darker colored lines with circles are from the sample close to the contact (within a few centimeters). Lighter, dashed lines with squares are from the samples several meters inward.

4.5.3 CSD Variation Through the Upper and Lower Sheets of the CRL

CSD variation plots for CRL samples (Figures 38 and 39) are modeled after Zieg and Marsh (2012) and show the elevation of each sample through the cross-section of the CRL on the y-axis versus the CSD population density for various crystal sizes on the x-axis. Units for the natural log of the population density are length^{-4}, as the volumetric number density of crystals has the units of length^{-3}, and it is divided by a length (the interval width of the bin size). Each colored line on the plot corresponds to a crystal bin size and shows the variation in population density for that crystal bin size from samples at different elevations throughout the thickness of the intrusion. Crystal bin sizes established for this study were 100, 80, 60, 40, 25, 20, 15, 10, and 5 µm. Bin sizes were chosen because, we consider crystals less than 100 µm to be groundmass in these porphyritic rocks. More bins for the smallest crystal sizes were used because they are more abundant in our samples, as is shown on the traditional CSD plots (Figures 36 and 37). For a sample at a given elevation within the intrusion, the range of population densities for the different crystal bin sizes is directly analogous to the slope of the line on a traditional CSD plot. In general, a wider range of population densities for a given sample on the diagram corresponds to fewer of the largest crystal sizes present in that sample. Conversely, a narrower range of population densities for a given sample corresponds to a higher population density of the larger crystal sizes.

The smallest crystal size classes (bin sizes 5-25 µm) have a consistently higher population density, generally ranging from e^{-15} to e^{-10} μm^{-4}, and do not show as much variation between samples with the highest population density of that crystal size and the samples with the lowest population density. For one crystal bin size, or one line on the plot, the population density generally ranges within 1-2 orders of magnitude, the largest range of values being about 4 orders of magnitude for one bin size. The larger crystal size classes (bin sizes 40-100 µm) show a wider range of population densities on the plot (fewer larger crystals) for a given bin size, generally ranging from about e^{-25} to e^{-14} μm^{-4}, and the largest range of population density values is about 13 orders of magnitude. For orthoclase and anorthite, few if any larger crystals (>40 µm) were present in some samples, resulting in physically unrealistic polynomial equation fits to the CSD curve at coarse crystal sizes. Due to this lack of data, those large crystal bin sizes were not plotted for orthoclase and anorthite.

Upper Sheet of CRL

The plots for the ~80 m thick upper sheet (Figure 38) generally show a wider variation in population densities (fewer large crystals) towards the top and bottom margins of the sheet, and a narrower variation (more larger crystals) in the center of the sheet. The CSD variation for quartz (Figure 38 A) is widest at the top and bottom margins of the sheet. For the samples at the highest elevations (2725-2730 m), the maximum variation of population density for all bin sizes is approximately 8 orders of magnitude. Towards the center of the sheet (around 2695 m), there is a narrower variation of about 6 orders of magnitude. At the lowest elevations (2660-2665 m), the maximum variation is approximately 10 orders of magnitude. The CSD variation for anorthite (Figure 38 B) shares a similar general pattern seen in quartz with a wider range of population densities at the top and bottom margins of the sheet and a narrower range in the center. The maximum population density range at the highest elevation (2730 m) is ~10 orders of magnitude. In the center of the sheet (around 2695 m), there is a narrower variation of ~8 orders of magnitude. At the bottom of the sheet (2660 m), the maximum variation is ~14 orders of magnitude. The CSD variation for orthoclase (Figure 38 C) shows a different pattern than the other two phases. At the top of the sheet (2730 m), the maximum range of population density of

~6 orders of magnitude. Towards the center of the sheet (2690-2695 m), there is an area of the plot with a wider range of population densities, around 10 orders of magnitude. The narrowest range of population densities for this plot occurs near 2705 m and 2670 m at ~5 and ~7 orders of magnitude, respectively.

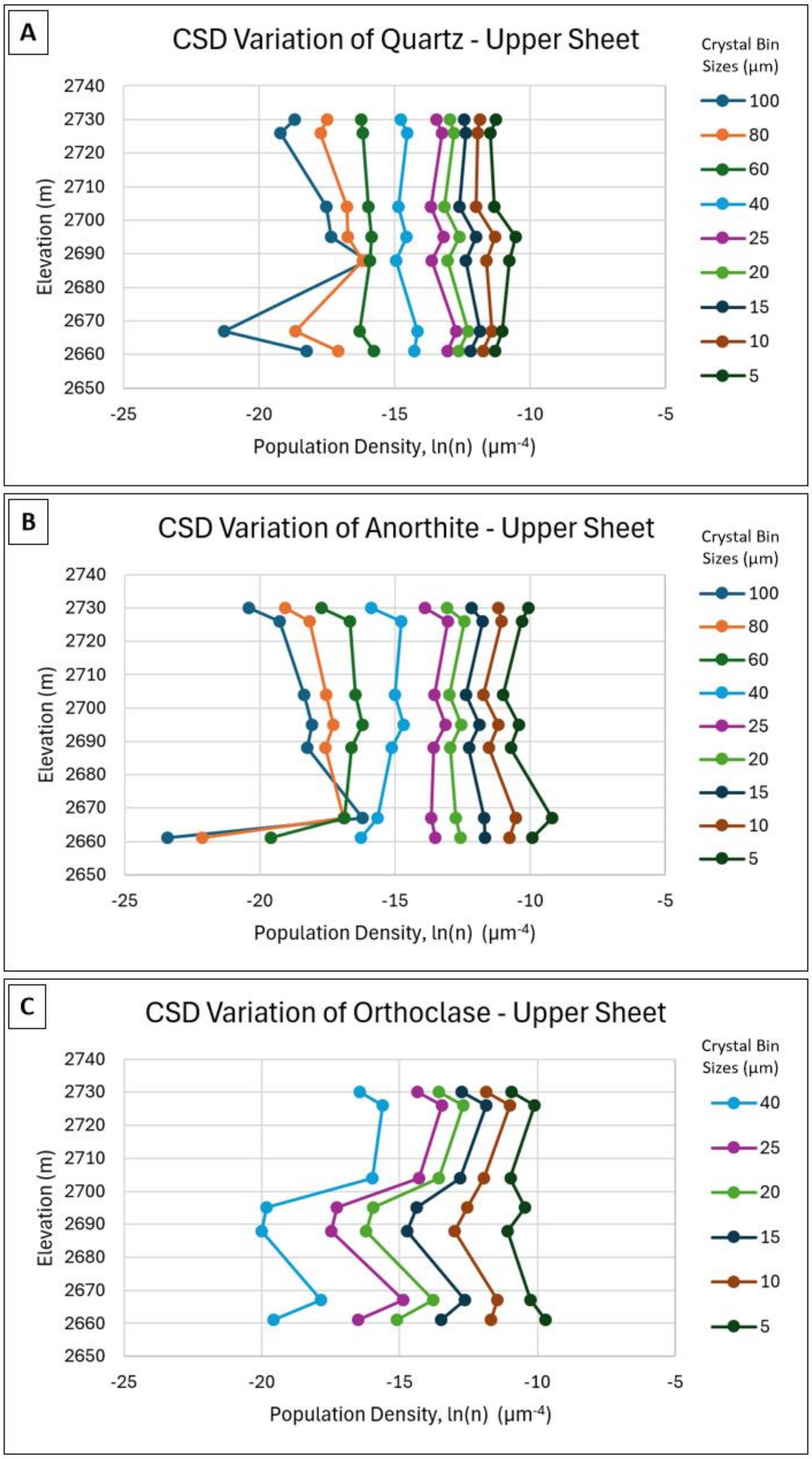

Figure 38. CSD Variation through the upper sheet of the CRL. Population density, ln(n) is shown as a function of elevation throughout the upper sheet of the CRL. Colors refer to different crystal size classes.

Lower Sheet of CRL

The plots for the ~300 m thick lower sheet (Figure 39) are more complicated than those of the thinner upper sheet. The CSD variation plot for quartz (Figure 39 A) shows zones of wider and narrower ranges of population densities at different elevations throughout the sheet. The widest population density variation occurs near the center of the sheet at an elevation of 2540-2580 m at ~16 orders of magnitude. The top and bottom of the sheet also have a wider range of population density variation of ~11 and ~14 orders of magnitude at 2630-2640 m and 2410 m respectively. Another area with a wide variation of population densities is between 2482-2429 m with ~10 orders of magnitude. Areas of narrower variation include orders of magnitude of ~5, ~6, and ~8 at elevations of 2594, 2500, and 2417 m respectively. The CSD variation for anorthite (Figure 39 B) is a simpler with a general pattern of a wider variation at the top of the sheet and a more narrow variation at the bottom with some fluctuation throughout. Areas of narrow variation occur at 2633 m elevation with ~6 orders of magnitude variation, 2595 m with ~5, 2539-2500 m with ~7, 2445-2417 m with ~6 orders of magnitude. Areas of wide variation occur at 2629-2609 m with ~12 orders of magnitude, 2578 m with ~9, 2482 m with ~9, and 2411 m elevation with ~9 orders of magnitude. The CSD variation for orthoclase (Figure 39 C) includes areas with narrow and wide ranges of population densities. Areas of narrow ranges of population densities include elevations of 2629 m with ~2 orders of magnitude variation, 2594 m with ~7, 2539-2500 m with ~5, and 2445-2429 m with ~4 orders of magnitude. Areas with wider ranges of population densities include 2642-2633 m with ~9 orders of magnitude difference, 2609 m with ~10, 2578 m with ~9, 2482 m with ~8, and 2417-2411 with ~12 orders of magnitude. The spatial distribution of the areas of wide and narrow population density variation may indicate the locations of multiple component pulses of magma and therefore the locations of boundary regions between potential component injections into the main upper and lower sheets.

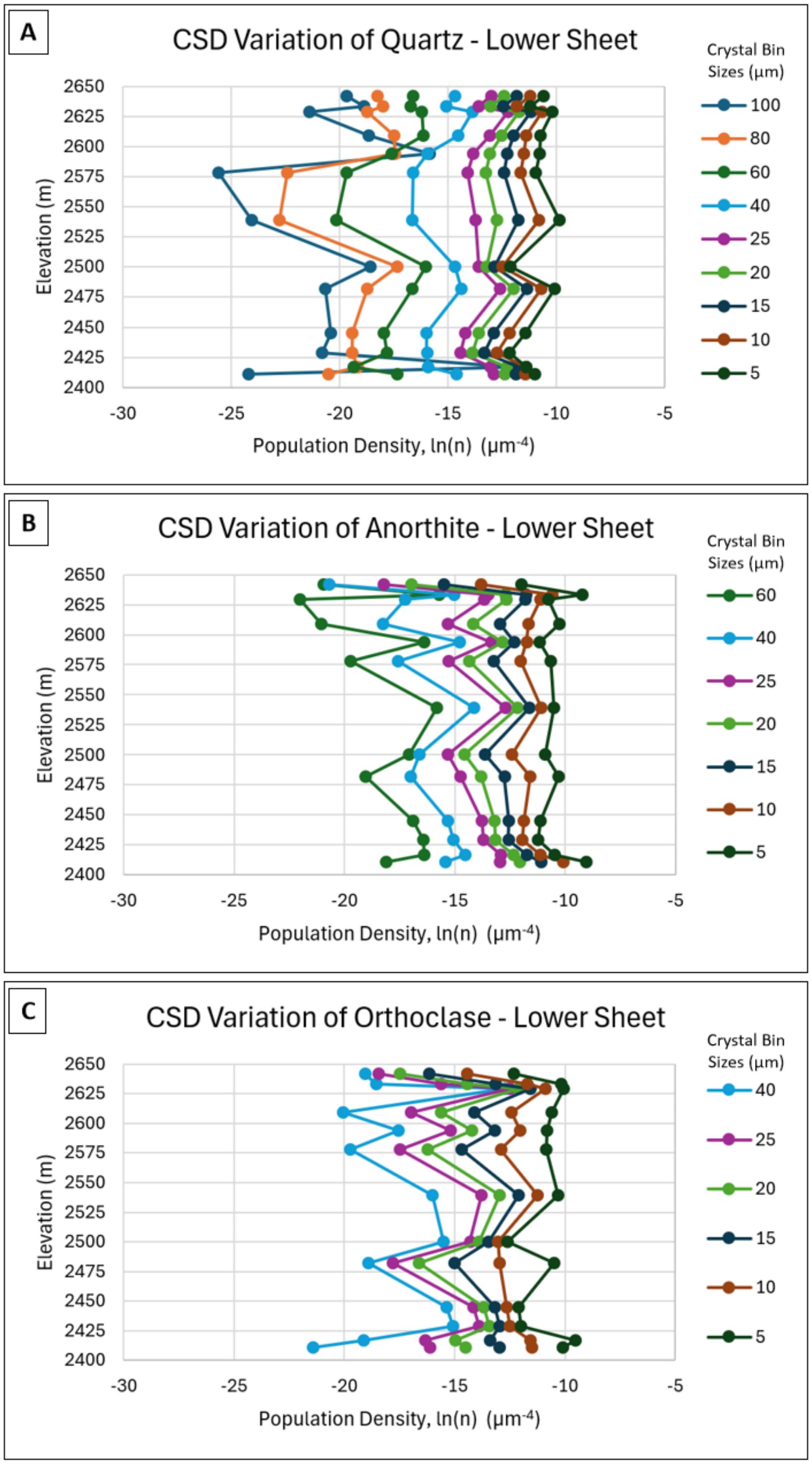

Figure 39. CSD variation throughout the lower sheet of the CRL. Population density, ln(n) is shown as a function of elevation throughout the lower sheet of the CRL. Colors refer to different crystal size classes.

5 Discussion

In this section, the data from each method utilized in this study, including fieldwork and sample collection, bulk magnetic susceptibility, microscopy, and CSD analysis are discussed and synthesized. Possible interpretations and implications of the results are also discussed.

For this study, the quantified texture of the groundmass of porphyritic rock is used to identify evidence of multiple component pulses or sheets building up larger intrusive sheets of a laccolith and to better understand the late-stage emplacement of the magma.

5.1 Field Work and Sample Collection

The fieldwork conducted on Mount Ellen and the Copper Ridge Laccolith aimed to provide a systematic sampling of the upper and lower sheets of the CRL (Figure 28). Using the CR22 and LN15 samples, a complete detailed cross-sectional sampling was completed, which was crucial for understanding the spatial variation in crystal sizes of the groundmass within the upper and lower sheets of the CRL.

5.2 Magnetic Susceptibility

In both the upper and lower sheets of the CRL, a general pattern exists of lower magnetic susceptibility toward the top and bottom of each sheet and a higher magnetic susceptibility toward the middle of the sheet (Figure 29). A higher magnetic susceptibility reading indicates a greater abundance of ferromagnetic minerals such as titanomagnetite, which is the primary contributor to the magnetic mineralogy of the Henry Mountains igneous rocks (Horsman et al., 2005). This pattern could be due to two main possibilities (1) the pattern is primary and the result of injection and crystallization, or (2) the pattern is secondary and the result of alteration of the primary pattern.

This pattern suggests several reasonable conclusions: (1) the basic composition of the upper and lower sheets is the same with no major geochemical difference which is consistent with previous work (Maurer, 2015). (2) The broad pattern within each sheet suggests the processes operating in each during emplacement and later alteration, if any, were similar. The upper and lower sheets seem to have broadly similar histories. (3) The data within each sheet includes slight variation that is likely to be natural variation but could be related to component sheets or multiple injections. These data alone are insufficient to make a definitive determination.

5.3 Microprobe and SEM/EBSD

The images obtained from microprobe analysis, SEM, and EBSD were used for data processing and CSD analysis. High-resolution, high-magnification images (Figures 31 and 33) reveal details about the fine-grained groundmass texture and chemistry showing that the finest groundmass crystals range from approximately 2-20 μm in size. The smallest bin size used for CSD analysis for this study was 5 μm, meaning some of the very smallest crystals are not analyzed. Additionally, the resolution for the EBSD phase maps that used a step size of 2-3 μm also does not analyze the very smallest crystals. Despite this, the consistent slope of the standard CSD curves at the finest bin sizes (Figures 34 and 35) suggests that the data for the 5 μm bin sizes provide a representative measure of the small grains of groundmass crystal population in these samples.

5.4 Crystal Size Distribution

5.4.1 Hypothesized CSD Results

In an idealized intrusion with a single pulse of magma injected into the host rock and that cooled below the solidus with no other factors, we would expect the groundmass CSD plots for the samples near the top and bottom of the sheet to have a steep and straight slope suggesting relatively fast and simple cooling/crystallization. Because the idealized intrusive sheet cools from the outside in, the samples from the center of the sheet would show a shallower CSD slope due to slower cooling/crystallization (Figure 40).

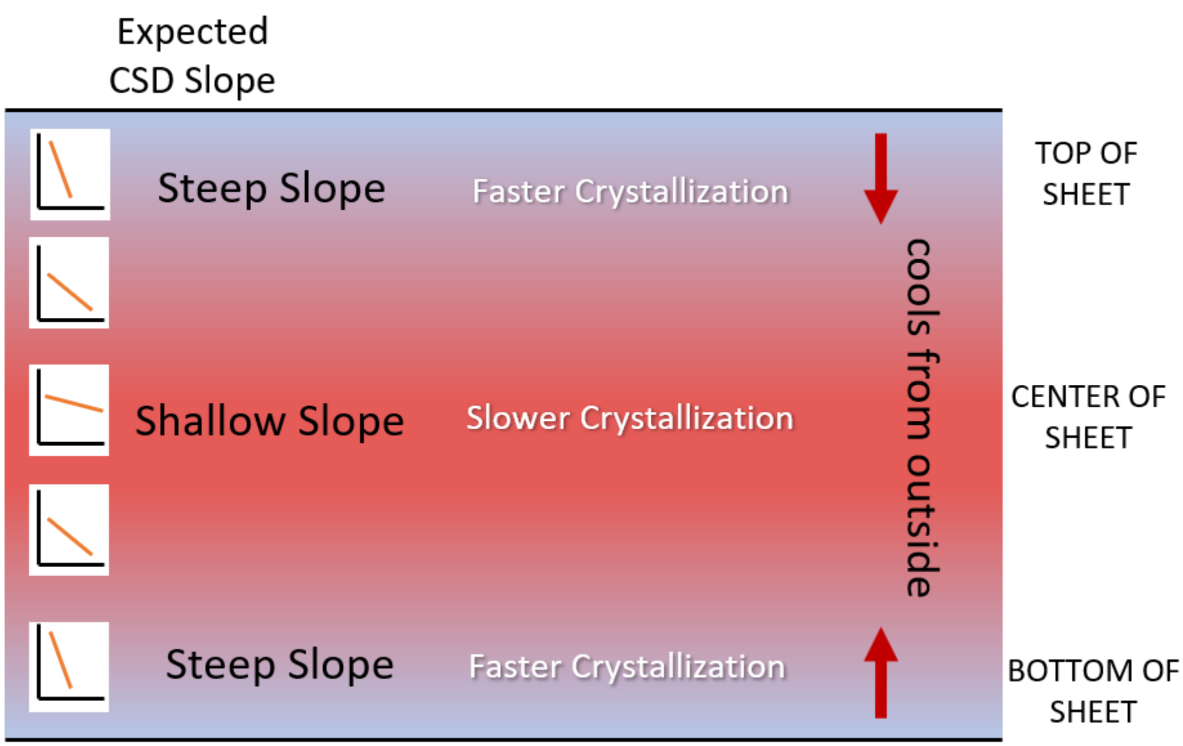

Figure 40. For an idealized cooling igneous sheet, expected CSD slopes are steeper at the margins and shallower towards the center due to faster crystallization at the margins and slower crystallization in the center.

Plotting these results to show the crystal population density at a given size versus elevation (Figures 38 and 39) helps to visualize the CSD throughout the intrusion. Using this type of plot (Figure 41), modeled after Zieg and Marsh (2012), it is possible to visualize the CSD variation of an idealized single pulse intrusion. At the top and bottom of the sheet, the population density variation for a range of crystal sizes should be wider due to faster crystallization at the margins (fewer large crystals), and a more narrow population density range in the center of the sheet with more relatively large crystals.

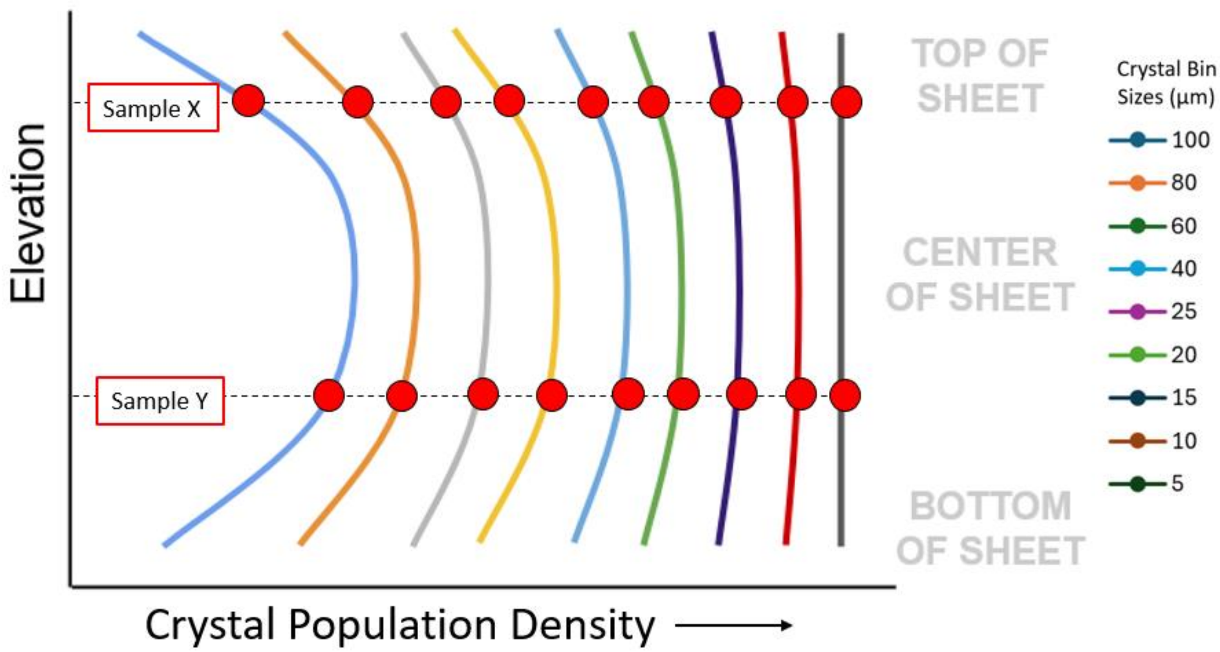

Figure 41. Crystal size population density variation for an idealized single pulse intrusion. Crystal population density is wider at the top and bottom of the sheet.

5.4.2 Interpreting CSD Variation Through the CRL

When plotting the results from this study to show the crystal population density versus elevation, as illustrated in Figure 41, samples at some elevations exhibit a wider variation of population density, while others display a narrower variation. Samples at elevations with a wider population density variation have fewer large crystals, which suggests faster cooling at those elevations. Conversely, samples at elevations with a narrower variation of population density contain more larger crystals in the groundmass, suggesting slower cooling at those elevations.

Upper Sheet of CRL

In the upper sheet of the CRL (Figure 38), the observed pattern matches reasonably well with the hypothesized pattern (Figure 41) for a single pulse of magma is present in the plots for quartz and anorthite (Figure 38 A and B). The plots of the CSD in each phase in the upper sheet show a wider variation in population densities (fewer large crystals) towards the top and bottom (the margins) of the sheet, and a narrower variation (more larger crystals) in the center of the sheet, consistent with emplacement by a single pulse (Figure 42 A and B). The plot for orthoclase shows an area of elevation with wider population densities in the center, near 2690 m, suggesting two possible pulses of magma (Figure 42 C). Based on the overall trends seen in the upper sheet, the simplest interpretation is that it was formed by a single pulse of magma similar to the idealized model shown in Figure 41.

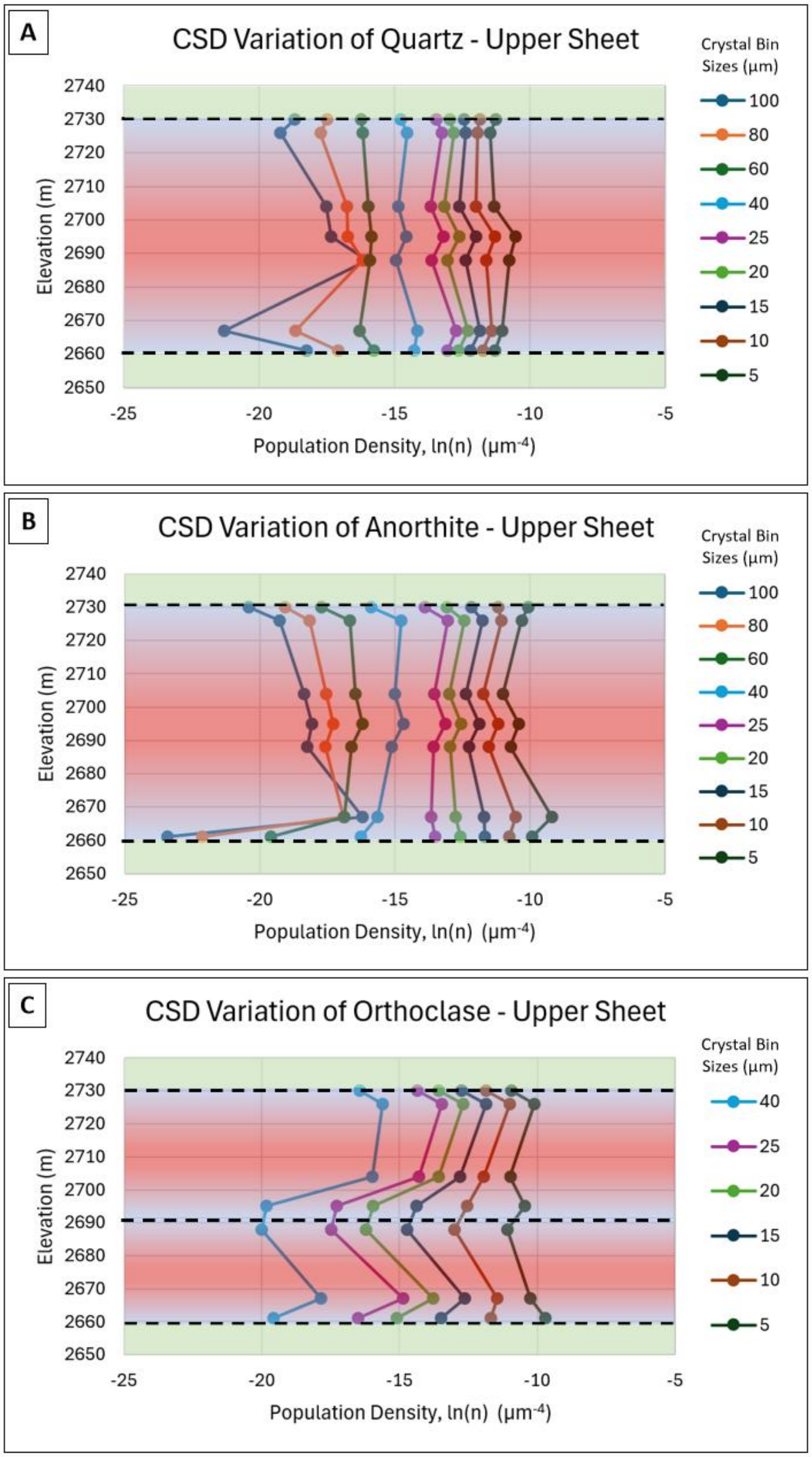

Figure 42. Interpreted pulses or component sheets for the upper sheet of the CRL. Blue shade indicates areas of more rapid crystallization, red shade indicates areas of slower crystallization, and black dashed lines indicate the contact boundary between component sheets or the contact with the sedimentary host rock (green shade).

Lower Sheet of CRL

The crystal population density variation in the lower sheet (Figure 39) is more complicated than the single pulse hypothesis (Figure 41). The population density variation for quartz (Figure 43 A) shows a wider variation near the top (2630 m) and bottom (2410 m) of the sheet as well as at 2575 m and 2475 m suggesting potential boundaries between component sheets at these elevations. Similarly, the population density variation for anorthite (Figure 43 B) shows the widest variation at the top and bottom of the sheet and at 2575 m and 2475 m reinforcing the idea of boundaries between component sheets. For orthoclase (Figure 43 C) the variation is wider at the top and bottom of the sheet as well as at 2575 m and 2474 m. Additionally, there is an area of wider variation around 2610 m suggesting a possible fourth component sheet. Overall, the pattern of wider elevations at the top of the lower sheet (2630 m), at 2575 m, 2475 m, and at the bottom (2410 m) suggests a construction history of the lower sheet of the CRL consisting of three pulses of magma, with each component sheet approximately 100 m thick.

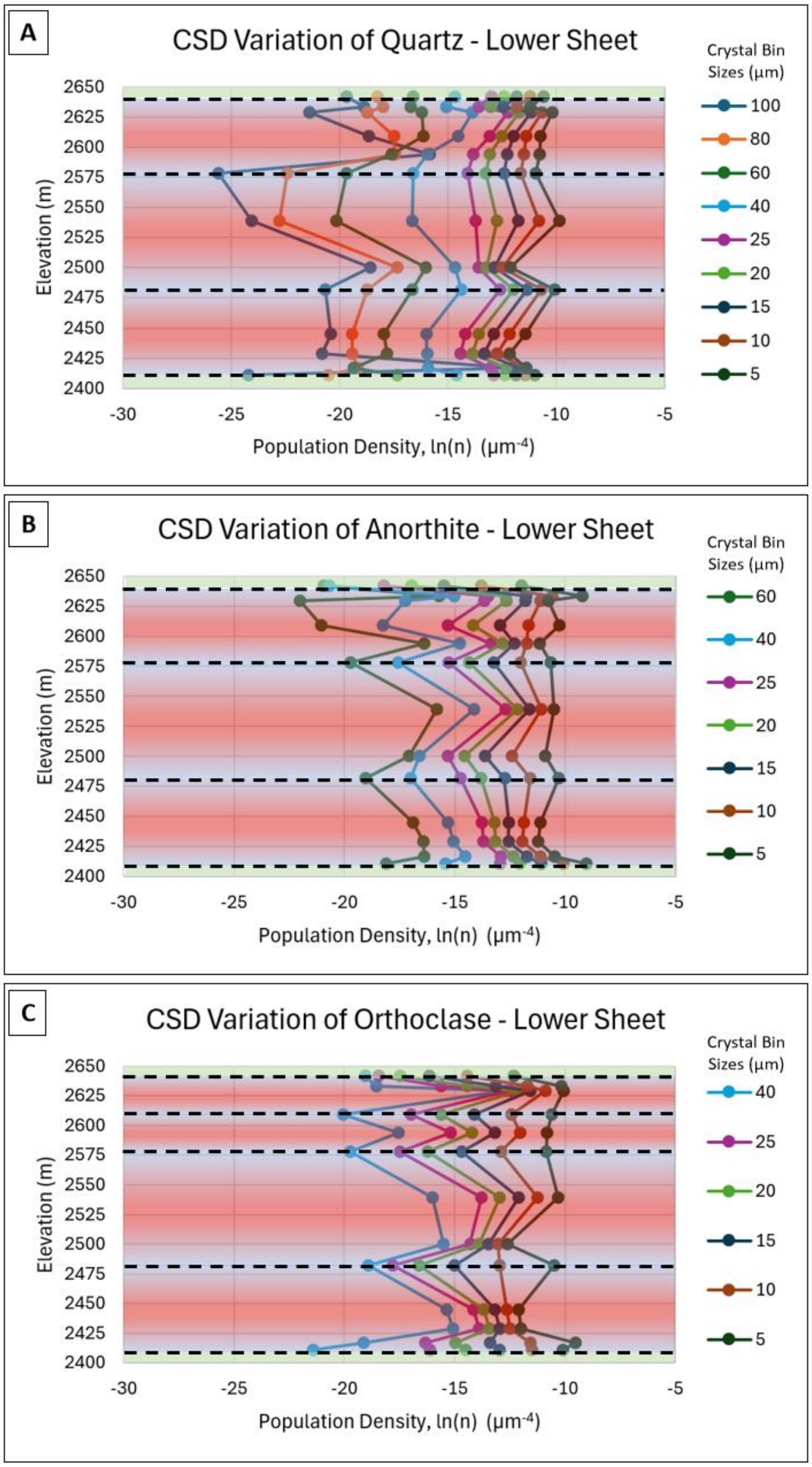

Figure 43. Interpreted pulses or sheets for the lower sheet of the CRL. Blue shade indicates areas of more rapid crystallization, red shade indicates areas of slower crystallization, and black dashed lines indicate the contact boundary between component sheets or the contact with the sedimentary host rock (green shade).

5.5 Overall Interpretations

This research provides evidence that the lower sheet of the CRL may be built from multiple component sheets of magma. CSD results and analyzing the crystal population density variation throughout various elevations of the CRL reveals that samples at some elevations have a wider variation of population density and therefore crystallized faster. These areas of likely faster crystallization are interpreted to be boundaries between component sheets in the intrusion. Based on these results, boundaries are interpreted at the top and bottom of both upper (2730 m and 2660 m) and lower (2640 m and 2410 m) sheets, as well as the lower sheet containing three component sheets with boundaries at 2575 m and 2475 m. Figure 44 shows a schematic interpreted cross-section of component sheets of the Copper Ridge Laccolith.

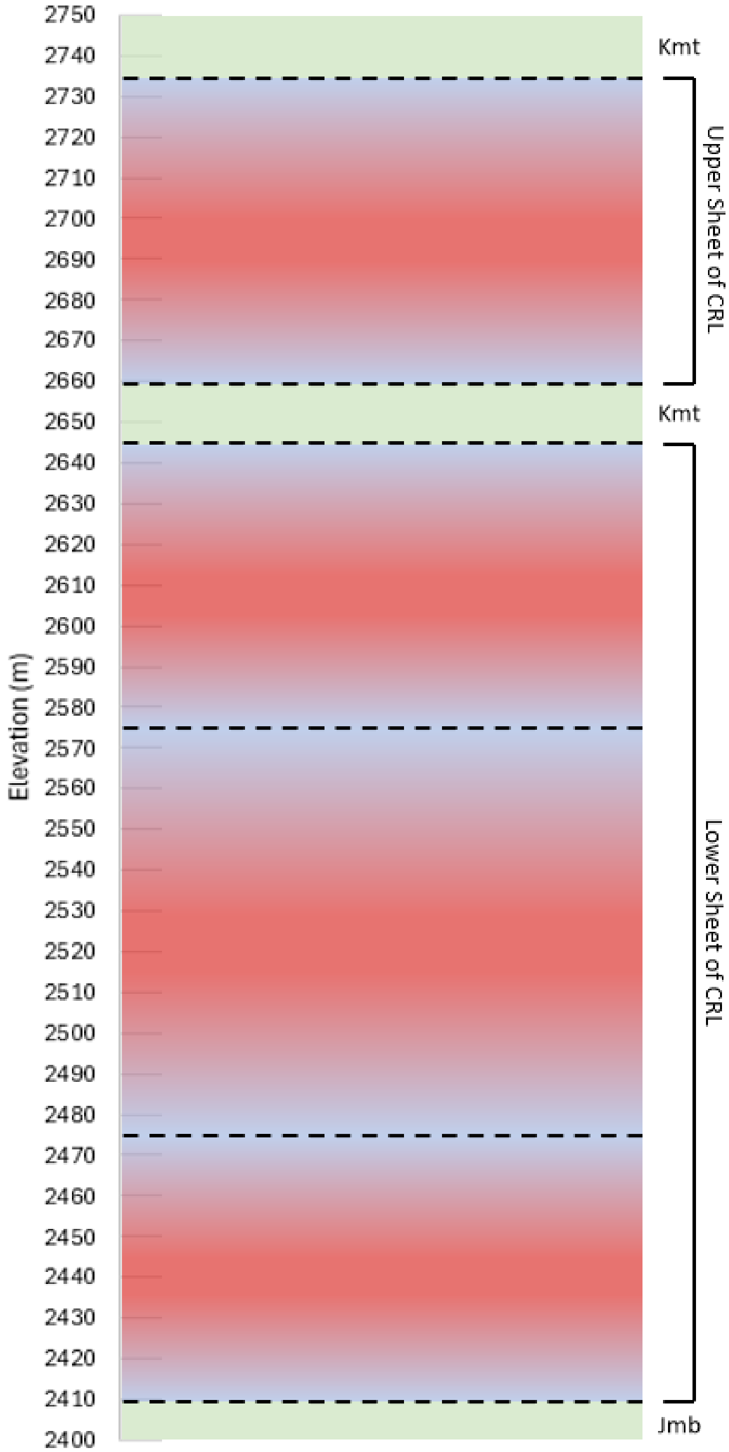

Figure 44. Cross section through the upper and lower sheets of the CRL showing the interpreted number and location of component sheets comprising the two main sheets. Blue shade indicates areas of more rapid crystallization, red shade indicates areas of slower crystallization, and black dashed lines mark the contact boundary between component sheets or the contact with the sedimentary host rock (green shade).

The results of this study allow for a rough interpretation of the injection order of the component sheets of the upper and lower sheets of the CRL (Figure 45). Comparing the general population densities of small and large crystals in the upper and lower sheets, the upper sheet has more larger groundmass crystals than the lower sheet suggesting that it cooled slower overall and therefore may have been injected after the lower sheet had been injected and started cooling. Based on the results for the thicker, more complex lower sheet, it is interpreted that it was constructed by three component sheets of magma. The center component sheet (2475-2575 m) overall has the finest groundmass grains suggesting the fastest crystallization in that area. The bottom component sheet (2410-2475 m) has slightly larger crystals than the center, suggesting that this component sheet was intruded next. The top component sheet (2575-2645 m) in the lower sheet has slightly larger groundmass grains than the center and bottom, suggesting that this component was intruded third. Figure 45 shows my interpreted injection order of the component sheets of the upper and lower sheets of the CRL based on the sizes of the groundmass crystals in the inferred component sheets.

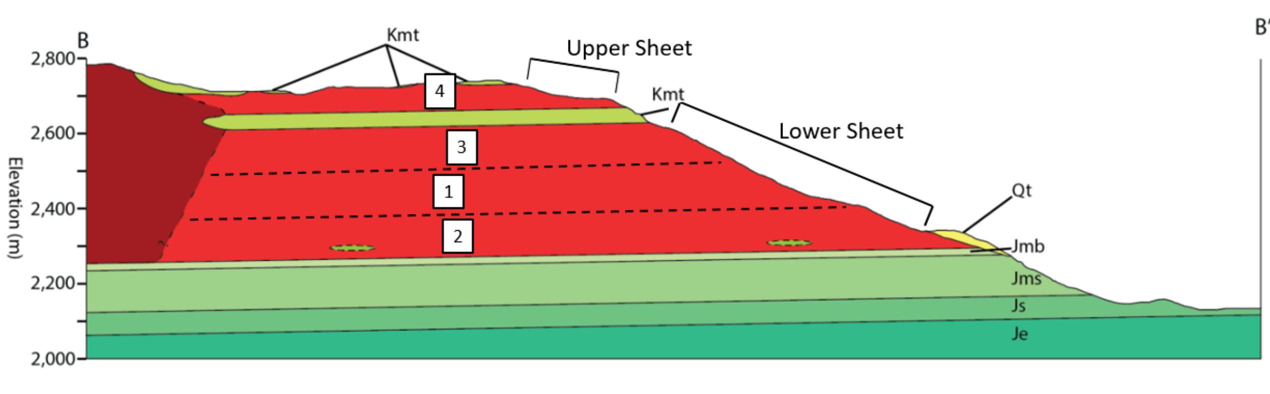

Figure 45. Interpreted injection order of the component sheets of the upper and lower sheets of the CRL. Modified from Maurer, 2015.

These interpretations assume that thermal cooling is the dominant factor of crystallization for the finest-grained (<100 μm) portions of the groundmass of these rocks. Initial crystallization of the phenocrysts of plagioclase and hornblende in these rocks likely occurred in mid-crustal magma reservoirs and possibly with decompression crystallization during initial magma ascent. The crystallization of the finest-grained groundmass occurred at the time of, or shortly after, emplacement and represents the final stages of magma emplacement. At the scale of an approximately 400 m thick igenous sheet in the very shallow crust (1-3 km depth), thermal cooling likely plays an important, perhaps dominant, role in the crystallization history of the finest-grained groundmass for this final stage of magma emplacement.

6 Conclusions

Magma plumbing systems within the shallow crust drive surface volcanism. Modern examples of these magma systems are difficult to study directly but ancient systems exposed at the surface can be used as analogs. The Henry Mountains in southern Utah consist of five well-exposed shallow crustal laccolith intrusions. The Copper Ridge Laccolith on the east side of Mount Ellen provides an excellent cross-sectional exposure of an upper and lower sheet. The Copper Ridge Laccolith is an exceptional opportunity to study part of an ancient shallow magma system and the processes that contributed to its construction.

This study aimed to investigate a method of using crystal size distribution analysis of igneous groundmass to better understand subvolcanic magma plumbing system evolution. Igneous groundmass in porphyritic rocks is a record of the ascent and emplacement of the magma. By analyzing the finest portions of the groundmass, we get a record of the final stages of emplacement into a ~400 m thick cross-section of the Copper Ridge Laccolith.

Results from this study indicate that the main sheets of the Copper Ridge Laccolith may have been built from multiple pulses of magma or component sheets. It is interpreted that the ~80-100 m thick upper sheet was constructed by a single injection of magma. The ~300-400 m thick lower sheet is interpreted to be constructed by at least three separate injections of magma creating ~100 m thick component sheets comprising the main lower sheet.

6.1 Future Work

Future research could include obtaining whole-rock and trace element geochemistry data, anisotropy of magnetic susceptibility, and paleomagnetic data at various elevations of the Copper

Ridge Laccolith to compare differences in data throughout the cross-section to further test the hypothesis of multiple pulses or component sheets of magma within the main sheets. Thermal modeling could also better explain the evolution of the late-stage emplacement of the Copper Ridge Laccolith. The crystallographic preferred orientation data from EBSD analysis could be used in a variety of ways, including use of orientation distribution functions to identify regions of high shear, which could be consistent with the margins of subsequent pulses. Thermodynamic modeling from whole-rock geochemical data could constrain phase saturation temperatures, which could help explain the differences in population densities between phases. Shape analysis and twin density tend to correlate with undercooling and may be useful corroborators with CSDs for any resulting thermal modeling.

7 References Cited

Annen, C., Latypov, R., Chistyakova, S., Cruden, A.R., and Nielsen, T.F.D., 2022, Catastrophic growth of totally molten magma chambers in months to years: Science Advances, v. 8, doi:10.1126/sciadv.abq0394.

Annen, C., Pichavant, M., Bachmann, O., and Burgisser, A., 2008, Conditions for the growth of a long-lived shallow crustal magma chamber below Mount Pelee volcano (Martinique, Lesser Antilles Arc): Journal of Geophysical Research: Solid Earth, v. 113, doi:10.1029/2007JB005049.

Arzi, A.A., 1978, Critical phenomena in the rheology of partially melted rocks: Tectonophysics, v. 44, p. 173–184, doi:10.1016/0040-1951(78)90069-0.

Best, M.G., 1982, Igneous and Metamorphic Petrology: New York, W.H. Freeman and Company.

Braunagel, M., 2016, Magnetic Evolution of the Copper Ridge Intrusion, Mount Ellen, Utah.

Broda, R.J., 2014, Geometry and Progressive Development of a Shallow Crustal Intrusive Complex, Mount Hillers, Henry Mountains, Utah: East Carolina University.

Burchardt, S., and Galland, O., 2016, Studying Volcanic Plumbing Systems – Multidisciplinary Approaches to a Multifaceted Problem: IntechOpen, 23–53 p., doi:10.5772/63959.

Caricchi, L., Townsend, M., Rivalta, E., and Namiki, A., 2021, The build-up and triggers of volcanic eruptions: Nature Reviews Earth and Environment, v. 2, p. 458–476, doi:10.1038/s43017-021-00174-8.

Cashman, K. V., 2020, Crystal Size Distribution (CSD) Analysis of Volcanic Samples: Advances and Challenges: Frontiers in Earth Science, v. 8, doi:10.3389/feart.2020.00291.

Castro, J.M., Cordonnier, B., Schipper, C.I., Tuffen, H., Baumann, T.S., and Feisel, Y., 2016, Rapid laccolith intrusion driven by explosive volcanic eruption: Nature Communications, v. 7, doi:10.1038/ncomms13585.

Coleman, D.S., Gray, W., and Glazner, A.F., 2004, Rethinking the emplacement and evolution of zoned plutons: Geochronologic evidence for incremental assembly of the Tuolumne Intrusive Suite, California: Geology, v. 32, p. 433–436, doi:10.1130/G20220.1.

Corry, C.E., 1988, Laccoliths; Mechanics of emplacement and growth: The Geological Society of America Special Paper, v. 220.

Currier, R.M., and Marsh, B.D., 2015, Mapping real time growth of experimental laccoliths: The effect of solidification on the mechanics of magmatic intrusion: Journal of Volcanology and Geothermal Research, v. 302, p. 211–224, doi:10.1016/j.jvolgeores.2015.07.009.

Dunlop, D.J., and Özdemir, Ö., 1997, Rock Magnetism: Fundamentals and Frontiers: Cambridge University Press: Cambridge University Press, doi:10.1017/CBO9780511612794.

Elliot, D.H., Fleming, T.H., Kyle, P.R., and Foland, K.A., 1999, Long-distance transport of magmas in the Jurassic Ferrar Large Igneous Province, Antarctica: Earth and Planetary Science Letters, v. 167, p. 89–104.

Flowers, R.M., 2010, The enigmatic rise of the Colorado Plateau: Geology, v. 38, p. 671–672, doi:10.1130/FOCUS072010.1.

Gilbert, G.K., 1877, Report on the geology of the Henry Mountains: U.S. Geological survey.:

Glazner, A.F., Bartley, J.M., Coleman, D.S., Gray, W., and Taylor, R.Z., 2004, Are plutons assembled over millions of years by amalgamation from small magma chambers? GSA Today, v. 14, p. 4–11, doi:10.1130/1052-5173(2004)014<0004:APAOMO>2.0.CO;2.

Gonnermann, H., and Taisne, B., 2015, Magma Transport in Dikes, *in* The Encyclopedia of Volcanoes, Elsevier, p. 215–224, doi:10.1016/B978-0-12-385938-9.00010-9.

Gudmundsson, A., 1990, Emplacement of dikes, sills and crustal magma chambers at divergent plate boundaries: Tectonophysics, v. 176, p. 257–275, doi:10.1016/0040-1951(90)90073-H.

Hansen, D.M., and Cartwright, J., 2006, The three-dimensional geometry and growth of forced folds above saucer-shaped igneous sills: Journal of Structural Geology, v. 28, p. 1520–1535, doi:10.1016/J.JSG.2006.04.004.

Higgins, M.D., 2002, Higgins2002_Closure in CSD, verification of CSD calcs, significance of CSD fans: American Mineralogist, v. 87, p. 171–175.

Higgins, M.D., 2000, Measurement of crystal size distributions: American Mineralogist, v. 85, p. 1105–1116.

Higgins, M.D., 1999, Origin of megacrysts in granitoids by textural coarsening: a crystal size distribution (CSD) study of microcline in the Cathedral Peak Granodiorite, Sierra Nevada, California: The Geological Society of London, v. 168, p. 207–219, https://www.lyellcollection.org.

Higgins, M.D., 2006, Quantitative Textural Measurements in Igneous and Metamorphic Petrology: Cambridge University Press, www.cambridge.org (accessed June 2024).

Higgins, M.D., 2011, Textural coarsening in igneous rocks: International Geology Review, v. 53, p. 354–376, doi:10.1080/00206814.2010.496177.

Horsman, E., Broda, R.J., Gwyn, N.Z., Maurer, E.A., Thornton, E.D., and Abstract, M.T.W., 2018, Progressive Construction of Laccolithic Intrusive Centers: Henry Mountains, Utah, U.S.A: Advances in Volcanology, doi:10.1007/978-3-319-14083-4_18.

Horsman, E., Morgan, S., De Saint-Blanquat, M., Habert, G., Nugent, A., Hunter, R.A., and Tikoff, B., 2009, Emplacement and assembly of shallow intrusions from multiple magma pulses, Henry Mountains, Utah, *in* Earth and Environmental Science Transactions of the Royal Society of Edinburgh, v. 100, p. 117–132, doi:10.1017/S1755691009016089.

Horsman, E., Tikoff, B., and Morgan, S., 2005, Emplacement-related fabric and multiple sheets in the Maiden Creek sill, Henry Mountains, Utah, USA: Journal of Structural Geology, v. 27, p. 1426–1444, doi:10.1016/j.jsg.2005.03.003.

Hunt, C.B., 1956, Cenozoic Geology of the Colorado Plateau: Geological Survey Professional Paper, v. 279.

Hunt, C.B., Averiti, P., and Miller, R.L., 1953, Geology and Geography of the Henry Mountains Region Utah: Geological Survey Professional Paper, v. 228.

Jackson, M.D., and Pollard, D.D. The laccolith-stock controversy: New results from the southern Henry Mountains, Utah:, http://pubs.geoscienceworld.org/gsa/gsabulletin/article-pdf/100/1/117/3379075/i0016-7606-100-1-117.pdf (accessed June 2024).

Kavanagh, J.L., Menand, T., and Sparks, R.S.J., 2006, An experimental investigation of sill formation and propagation in layered elastic media: Earth and Planetary Science Letters, v. 245, p. 799–813, doi:10.1016/J.EPSL.2006.03.025.

Magee, C. et al., 2018, Magma plumbing systems: A geophysical perspective: Journal of Petrology, v. 59, p. 1217–1251, doi:10.1093/petrology/egy064.

Marsh, B.D., 1988, Crystal size distribution (CSD) in rocks and the kinetics and dynamics of crystallization I. Theory.:

Marsh, B.D., 2007, Crystallization of silicate magmas deciphered using crystal size distributions, *in* Journal of the American Ceramic Society, v. 90, p. 746–757, doi:10.1111/j.1551-2916.2006.01473.x.

Maurer, E.A., 2015, Geometry and construction history of the Copper Ridge laccolith, Mount Ellen, Henry Mountains, Utah.

Menand, T., 2008, The mechanics and dynamics of sills in layered elastic rocks and their implications for the growth of laccoliths and other igneous complexes: Earth and Planetary Science Letters, v. 267, p. 93–99, doi:10.1016/J.EPSL.2007.11.043.

Morgan, D.J., and Jerram, D.A., 2006, On estimating crystal shape for crystal size distribution analysis: Journal of Volcanology and Geothermal Research, v. 154, p. 1–7, doi:10.1016/j.jvolgeores.2005.09.016.

Morgan, S., Stanik, A., Horsman, E., Tikoff, B., de Saint Blanquat, M., and Habert, G., 2008, Emplacement of multiple magma sheets and wall rock deformation: Trachyte Mesa intrusion, Henry Mountains, Utah: Journal of Structural Geology, v. 30, p. 491–512, doi:10.1016/j.jsg.2008.01.005.

Murray, K.E., Reiners, P.W., and Thomson, S.N., 2016, Rapid Pliocene-Pleistocene erosion of the central Colorado Plateau documented by apatite thermochronology from the Henry Mountains: Geology, v. 44, p. 483–486, doi:10.1130/G37733.1.

Nelson, S.T., and Davidson, J.P., 1993, Interactions Between Mantle-Derived Magmas and Mafic Crust, Henry Mountains, Utah: Journal of Geophysical Research, v. 98, p. 1837–1852.

Nelson, S.T., Davidson, J.P., and Sullivan, K.R., 1992, New age determinations of central Colorado Plateau laccoliths, Utah: Recognizing disturbed K-Ar systematics and re-evaluating tectonomagmatic relationships: Geological Society of America Bulletin, v. 104,

p. 1547–1560, http://pubs.geoscienceworld.org/gsa/gsabulletin/article-pdf/104/12/1547/3381263/i0016-7606-104-12-1547.pdf.

Pederson, J.L., Mackley, R.D., and Eddleman, J.L., 2002, Colorado Plateau uplift and erosion evaluated using GIS: GSA Today, p. 4–10.

Prior, D.J. et al., 1999, The application of electron backscatter diffraction and orientation contrast imaging in the SEM to textural problems in rocks: American Mineralogist, v. 84, p. 1741–1759, http://pubs.geoscienceworld.org/msa/ammin/article-pdf/84/11-12/1741/4008237/amin_84_11_12_1741-1759.pdf.

De Saint Blanquat, M., Horsman, E., Habert, G., Morgan, S., Vanderhaeghe, O., Law, R., and Tikoff, B., 2011, Multiscale magmatic cyclicity, duration of pluton construction, and the paradoxical relationship between tectonism and plutonism in continental arcs: Tectonophysics, v. 500, p. 20–33, doi:10.1016/j.tecto.2009.12.009.

de Sousa, L., 2021, Constraints on Incremental Assembly of Upper Crustal Igneous Intrusions, Mount Ellen, Henry Mountains, Utah.

Thompson, G.A., and Zoback, M. Lou, 1979, Regional geophysics of the Colorado Plateau: Tectonophysics, v. 61, p. 149–181, doi:10.1016/0040-1951(79)90296-8.

Thomson, K., and Hutton, D., 2004, Geometry and growth of sill complexes: Insights using 3D seismic from the North Rockall Trough: Bulletin of Volcanology, v. 66, p. 364–375, doi:10.1007/S00445-003-0320-Z/FIGURES/12.

Thornton, E., 2014, Timing, internal flow characteristics, and emplacement mechanisms of the intrusive sheet network on the southern margin of Mount Hillers, Henry Mountains, southern Utah: East Carolina University.

Tibaldi, A., 2015, Structure of volcano plumbing systems: A review of multi-parametric effects: Journal of Volcanology and Geothermal Research, v. 298, p. 85–135, doi:10.1016/j.jvolgeores.2015.03.023.

Ward, M.T., 2014, Geometry and Construction History of a Complex Intrusive Center in the Shallow Crust, Mount Pennell, Henry Mountains, Utah.

Weber, G., Simpson, G., and Caricchi, L., 2020, Magma diversity reflects recharge regime and thermal structure of the crust: Nature Research Scientific Reports, v. 10, doi:10.1038/s41598-020-68610-1.

White, S.M., Crisp, J.A., and Spera, F.J., 2006, Long-term volumetric eruption rates and magma budgets: Geochemistry, Geophysics, Geosystems, v. 7, doi:10.1029/2005GC001002.

Zieg, M.J., and Marsh, B.D., 2012, Multiple reinjections and crystal-mush compaction in the Beacon sill, McMurdo Dry Valleys, Antarctica: Journal of Petrology, v. 53, p. 2567–2591, doi:10.1093/petrology/egs059.

8 Appendices

8.1 Appendix A: Crystal Size Distribution Data

Table 2. CSD data for the upper sheet of the Copper Ridge Laccolith LN15 samples.

	Quartz		Anorthite		Orthoclase	
	Crystal Size (µm)	(ln) Pop. Density	Crystal Size (µm)	(ln) Pop. Density	Crystal Size (µm)	(ln) Pop. Density
LN15_4a	268.9		268.9	-22.39	268.9	
	208.6	-23.58	208.6	-21.63	208.6	
	148	-19.65	148	-20.2	148	
	95.7	-17.38	95.7	-18.01	95.7	-19.79
	67.2	-16.46	67.2	-16.86	67.2	-18.01
	52.1	-15.59	52.1	-15.96	52.1	-16.93
	37	-14.59	37	-14.81	37	-15.81
	21.64	-13.45	21.64	-13.32	21.64	-13.72
	7.5	-11.64	7.5	-11.24	7.5	-11.5
	Quartz		Anorthite		Orthoclase	
	Crystal Size (µm)	(ln) Pop. Density	Crystal Size (µm)	(ln) Pop. Density	Crystal Size (µm)	(ln) Pop. Density
LN15_6a	268.9		268.9	-22.31	101.3	
	208.6	-22.43	208.6	-20.7	78.6	
	148	-19.76	148	-19.54	55.8	
	95.7	-17.58	95.7	-17.55	36.1	-19.37
	67.2	-16.23	67.2	-16.51	25.3	-17.64
	52.1	-15.4	52.1	-15.53	19.6	-15.48
	37	-14.28	37	-14.58	13.9	-13.99
	21.64	-12.93	21.64	-12.96	8.15	-12.01
	7.5	-10.88	7.5	-10.59	2.83	-9.35
	Quartz		Anorthite		Orthoclase	
	Crystal Size (µm)	(ln) Pop. Density	Crystal Size (µm)	(ln) Pop. Density	Crystal Size (µm)	(ln) Pop. Density
LN15_10a	268.9	-24	268.9	-24.01	89.6	
	208.6	-23.83	208.6	-21.47	69.5	
	148	-19.69	148	-19.72	49.3	-20.79
	95.7	-18.04	95.7	-17.84	31.9	-18.48
	67.2	-16.66	67.2	-17.06	22.4	-17.07
	52.1	-15.84	52.1	-15.93	17.4	-15.4
	37	-14.68	37	-14.93	12.3	-14.06
	21.64	-13.31	21.64	-13.3	7.21	-12.21
	7.5	-11.25	7.5	-11	2.5	-9.73

Table 3. CSD data for the upper sheet of the Copper Ridge Laccolith CR22 samples.

Sample	Quartz		Anorthite		Orthoclase	
	Crystal Size (µm)	(ln) Pop. Density	Crystal Size (µm)	(ln) Pop. Density	Crystal Size (µm)	(ln) Pop. Density
CR_2205a	131.8	-20.17	149.4	-22.09	119.5	
	102.2	-19.62	115.9	-21.99	92.7	
	72.5	-17.61	82.2	-18.55	65.8	
	46.9	-15.97	53.2	-16.76	42.6	-18.87
	33	-14.4	37.3	-15.22	29.9	-17.1
	25.6	-13.68	29	-14.18	23.2	-15.2
	18.1	-12.65	20.6	-12.34	16.4	-12.96
	10.61	-12.05	12.02	-11.38	9.62	-11.89
	3.68		4.17		3.33	

Sample	Quartz		Anorthite		Orthoclase	
	Crystal Size (µm)	(ln) Pop. Density	Crystal Size (µm)	(ln) Pop. Density	Crystal Size (µm)	(ln) Pop. Density
CR_2205b	143.4		134.4	-21.85	89.6	
	111.2		104.3		69.5	
	78.9	-18.79	74	-21.34	49.3	
	51.1	-15.43	47.9	-18.22	31.9	-18.86
	35.9	-13.55	33.6	-15.35	22.4	-15.4
	27.8	-12.45	26.1	-13.96	17.4	-13.77
	19.7	-11.37	18.5	-12.12	12.3	-11.9
	11.54	-11.09	10.82	-11.28	7.21	-10.88
	4		3.75		2.5	

Sample	Quartz		Anorthite		Orthoclase	
	Crystal Size (µm)	(ln) Pop. Density	Crystal Size (µm)	(ln) Pop. Density	Crystal Size (µm)	(ln) Pop. Density
CR_2206	162.5	-21.31	134.4		162.5	
	126	-18.73	104.3	-20.06	126	
	89.4	-18.06	74	-18.33	89.4	-20.36
	57.8	-15.93	47.9	-16.56	57.8	-18.57
	40.6	-14.54	33.6	-15.27	40.6	-16.35
	31.5	-13.88	26.1	-14	31.5	-15.44
	22.4	-12.98	18.5	-12.49	22.4	-13.6
	13.07	-12.49	10.82	-11.51	13.07	-12.62
	4.53		3.75		4.53	

Sample	Quartz		Anorthite		Orthoclase	
	Crystal Size (µm)	(ln) Pop. Density	Crystal Size (µm)	(ln) Pop. Density	Crystal Size (µm)	(ln) Pop. Density
CR_2207	179.3	-22.79	201.7	-21.89	203.2	
	139	-20.97	156.4	-21.21	157.6	
	98.7	-18.46	111	-19.32	111.8	-21.37
	63.8	-16.42	71.8	-17.53	72.3	-19.46
	44.8	-15	50.4	-15.99	50.8	-17.07
	34.8	-14.12	39.1	-14.74	39.4	-15.19
	24.7	-12.94	27.7	-12.94	28	-13.52
	14.43	-12.36	16.23	-12.04	16.35	-12.47
	5		5.63		5.67	

Sample	Quartz		Anorthite		Orthoclase	
	Crystal Size (µm)	(ln) Pop. Density	Crystal Size (µm)	(ln) Pop. Density	Crystal Size (µm)	(ln) Pop. Density
CR_2208a	167.3	-20.85	155.4		113.5	
	129.8	-19.89	120.5		88.1	
	92.1	-17.66	85.5	-20.56	62.5	-20.73
	59.6	-15.64	55.3	-18.16	40.4	-20.1
	41.8	-14.42	38.8	-16.28	28.4	-17.15
	32.4	-13.73	30.1	-14.27	22	-15.5
	23	-12.78	21.4	-12.52	15.6	-13.33
	13.47	-12.13	12.5	-11.37	9.14	-11.74
	4.67		4.33		3.17	

Sample	Quartz		Anorthite		Orthoclase	
	Crystal Size (µm)	(ln) Pop. Density	Crystal Size (µm)	(ln) Pop. Density	Crystal Size (µm)	(ln) Pop. Density
CR_2208b	147.2		134.4		134.4	
	114.2		104.3	-20.01	104.3	
	81	-18.97	74	-18.34	74	
	52.4	-15.71	47.9	-16.55	47.9	-19.19
	36.8	-13.91	33.6	-15.33	33.6	-16.76
	28.6	-12.98	26.1	-13.89	26.1	-15.2
	20.3	-12.1	18.5	-12.06	18.5	-13.06
	11.85	-11.77	10.82	-10.92	10.82	-11.83
	4.11		3.75		3.75	

Table 4. CSD data for the lower sheet of the Copper Ridge Laccolith LN15 samples.

Sample	Quartz		Anorthite		Orthoclase	
	Crystal Size (µm)	(ln) Pop. Density	Crystal Size (µm)	(ln) Pop. Density	Crystal Size (µm)	(ln) Pop. Density
LN15_11a	268.9	-24.02	103.4		105.9	
	208.6		80.2	-22.08	82.2	
	148	-23.47	56.9	-21.91	58.3	
	95.7	-19.27	36.8	-21.19	37.7	-19.07
	67.2	-17.24	25.9	-17.63	26.5	-18.84
	52.1	-15.74	20.1	-16.92	20.5	-17.48
	37	-14.26	14.2	-15.44	14.6	-15.89
	21.64	-12.69	8.32	-13.68	8.53	-13.88
	7.5	-10.87	2.88	-10.85	2.95	-11.36
	Quartz		Anorthite		Orthoclase	
	Crystal Size (µm)	(ln) Pop. Density	Crystal Size (µm)	(ln) Pop. Density	Crystal Size (µm)	(ln) Pop. Density
LN15_13a	268.9		89.6	-22.14	105.9	
	208.6		69.5	-22.03	82.2	
	148	-20.7	49.3	-19.4	58.3	-21.95
	95.7	-18.25	31.9	-16.37	37.7	-19.3
	67.2	-16.76	22.4	-14.62	26.5	-17.62
	52.1	-15.86	17.4	-13.74	20.5	-15.7
	37	-14.17	12.3	-12.71	14.6	-14.14
	21.64	-12.44	7.21	-11.03	8.53	-11.85
	7.5	-11.24	2.5	-9.14	2.95	-9.7
	Quartz		Anorthite		Orthoclase	
	Crystal Size (µm)	(ln) Pop. Density	Crystal Size (µm)	(ln) Pop. Density	Crystal Size (µm)	(ln) Pop. Density
LN15_14a	152.4		268.9		179.3	
	118.2	-22.57	208.6	-22.86	139	
	83.9	-19.42	148	-21.05	98.7	
	54.3	-17.49	95.7	-18.34	63.8	-19.73
	38.1	-16.2	67.2	-16.92	44.8	-18.63
	29.5	-14.37	52.1	-15.75	34.8	-16.75
	21	-13.19	37	-14.62	24.7	-14.94
	12.26	-11.83	21.64	-13.27	14.43	-12.91
	4.25	-10.68	7.5	-11.23	5	-11

LN15_15b	Quartz		Anorthite		Orthoclase	
	Crystal Size (µm)	(ln) Pop. Density	Crystal Size (µm)	(ln) Pop. Density	Crystal Size (µm)	(ln) Pop. Density
	152.4		105.9	-21.7	89.6	
	118.2	-22.78	82.2	-21.16	69.5	
	83.9	-20.88	58.3	-19.97	49.3	-19.85
	54.3	-18.18	37.7	-17.03	31.9	-18.85
	38.1	-16.43	26.5	-15.46	22.4	-16.77
	29.5	-14.85	20.5	-14.48	17.4	-15.5
	21	-13.28	14.6	-13.22	12.3	-13.68
	12.26	-11.87	8.53	-11.94	7.21	-11.82
	4.25	-10.92	2.95	-9.79	2.5	-9.76

LN15_16a	Quartz		Anorthite		Orthoclase	
	Crystal Size (µm)	(ln) Pop. Density	Crystal Size (µm)	(ln) Pop. Density	Crystal Size (µm)	(ln) Pop. Density
	143.4		268.9	-22.48	268.9	
	111.2		208.6	-21.78	208.6	
	78.9	-20.86	148	-20.76	148	
	51.1	-17.95	95.7	-17.74	95.7	-21.22
	35.9	-16.14	67.2	-16.36	67.2	-19.25
	27.8	-14.26	52.1	-15.23	52.1	-17.31
	19.7	-12.5	37	-13.98	37	-15.5
	11.54	-10.86	21.64	-12.6	21.64	-13.37
	4	-9.84	7.5	-10.53	7.5	-10.72

LN15_18a	Quartz		Anorthite		Orthoclase	
	Crystal Size (µm)	(ln) Pop. Density	Crystal Size (µm)	(ln) Pop. Density	Crystal Size (µm)	(ln) Pop. Density
	268.9	-23.46	89.6	-20.78	268.9	-24.14
	208.6	-23.29	69.5	-19.39	208.6	-23.24
	148	-20.82	49.3	-18.22	148	-21.1
	95.7	-18.37	31.9	-16	95.7	-18.47
	67.2	-16.55	22.4	-14.79	67.2	-17.23
	52.1	-15.47	17.4	-14.24	52.1	-16.57
	37	-14.5	12.3	-13.25	37	-15.45
	21.64	-13.39	7.21	-11.77	21.64	-14.18
	7.5	-12.22	2.5	-9.81	7.5	-12.46

	Quartz		Anorthite		Orthoclase	
	Crystal Size (µm)	(ln) Pop. Density	Crystal Size (µm)	(ln) Pop. Density	Crystal Size (µm)	(ln) Pop. Density
LN15_19a	268.9		116.5		89.6	
	208.6		90.4	-21.19	69.5	
	148		64.1	-19.52	49.3	
	95.7	-19.76	41.5	-17.07	31.9	-18.79
	67.2	-17.71	29.1	-15.46	22.4	-17.37
	52.1	-15.58	22.6	-14.07	17.4	-15.72
	37	-13.76	16	-13.17	12.3	-13.99
	21.64	-11.93	9.38	-11.67	7.21	-11.57
	7.5	-10.62	3.25	-9.63	2.5	-9.13

	Quartz		Anorthite		Orthoclase	
	Crystal Size (µm)	(ln) Pop. Density	Crystal Size (µm)	(ln) Pop. Density	Crystal Size (µm)	(ln) Pop. Density
LN15_20a	152.4	-21.45	268.9	-23.58	268.9	
	118.2	-21.33	208.6	-21.97	208.6	-22.24
	83.9	-19.74	148	-20.2	148	-20.39
	54.3	-17.95	95.7	-18.09	95.7	-18.4
	38.1	-15.7	67.2	-17.31	67.2	-17.09
	29.5	-14.63	52.1	-15.96	52.1	-16.26
	21	-13.52	37	-14.97	37	-15.25
	12.26	-12.55	21.64	-13.61	21.64	-14.1
	4.25	-11.45	7.5	-11.36	7.5	-12.15

	Quartz		Anorthite		Orthoclase	
	Crystal Size (µm)	(ln) Pop. Density	Crystal Size (µm)	(ln) Pop. Density	Crystal Size (µm)	(ln) Pop. Density
LN15_21a	143.4	-22.64	268.9	-23.16	268.9	
	111.2	-21.04	208.6	-21.55	208.6	-22.37
	78.9	-19.56	148	-19.56	148	-20.59
	51.1	-16.99	95.7	-17.68	95.7	-18.13
	35.9	-15.47	67.2	-16.53	67.2	-17.05
	27.8	-14.49	52.1	-15.87	52.1	-16.02
	19.7	-13.73	37	-14.85	37	-14.9
	11.54	-13.14	21.64	-13.47	21.64	-13.87
	4	-12.06	7.5	-11.47	7.5	-12.03

Table 5. CSD data for the lower sheet of the Copper Ridge Laccolith CR22 samples.

	Quartz		Anorthite		Orthoclase	
	Crystal Size (µm)	(ln) Pop. Density	Crystal Size (µm)	(ln) Pop. Density	Crystal Size (µm)	(ln) Pop. Density
CR_2203	146.7		140		89.6	
	113.8		108.6	-21.97	69.5	
	80.7	-20.42	77.1	-20.6	49.3	
	52.2	-16.29	49.9	-16.75	31.9	-18.46
	36.7	-14.22	35	-14.64	22.4	-15.34
	28.4	-13.12	27.2	-13.24	17.4	-13.87
	20.2	-12.06	19.3	-11.6	12.3	-11.79
	11.8	-11.82	11.27	-10.79	7.21	-10.85
	4.09		3.91		2.5	
	Quartz		Anorthite		Orthoclase	
	Crystal Size (µm)	(ln) Pop. Density	Crystal Size (µm)	(ln) Pop. Density	Crystal Size (µm)	(ln) Pop. Density
CR_2204	132.5		168.7		89.6	
	102.8		130.9	-20.79	69.5	
	72.9	-20.41	92.8	-18.94	49.3	-19.74
	47.2	-17.44	60.1	-16.61	31.9	-18.58
	33.1	-14.81	42.2	-14.83	22.4	-15.27
	25.7	-13.15	32.7	-13.61	17.4	-14.01
	18.2	-11.87	23.2	-12.52	12.3	-11.99
	10.66	-11.52	13.58	-11.78	7.21	-10.94
	3.7		4.71		2.5	

8.2 Appendix B: Equations

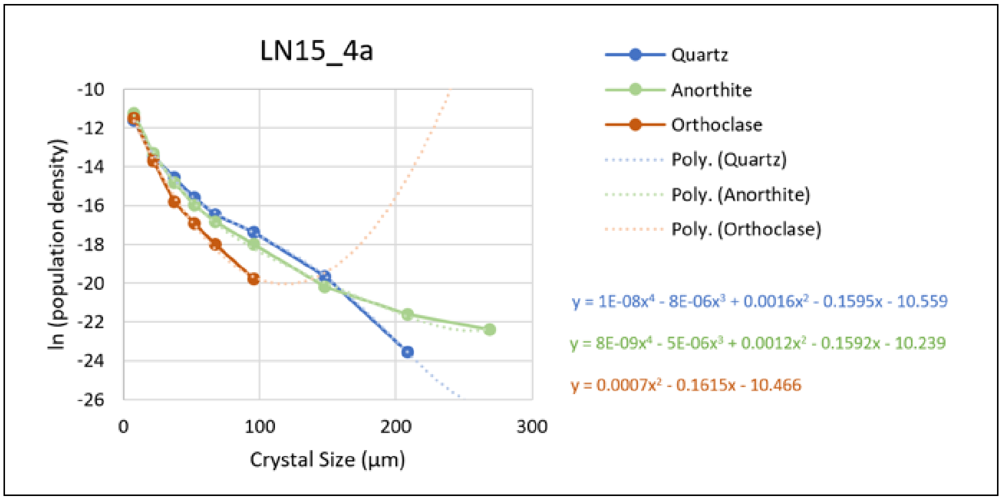

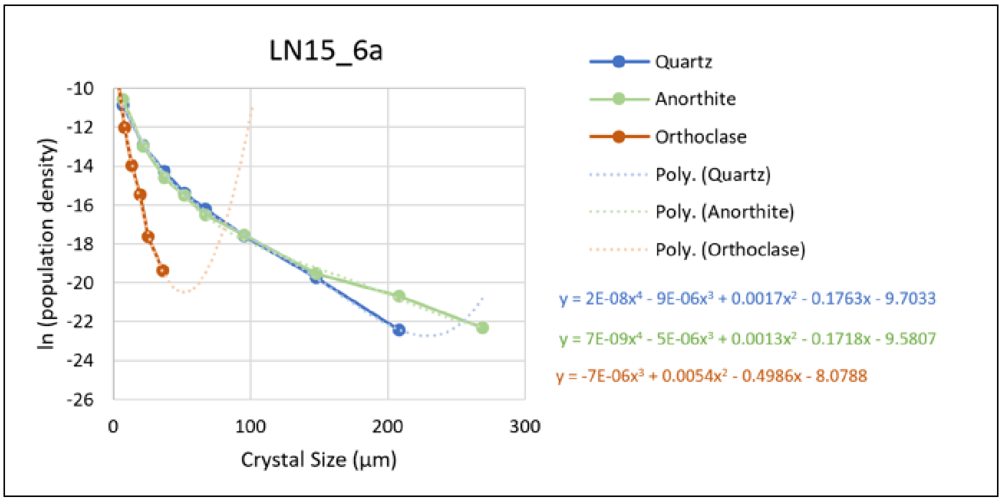

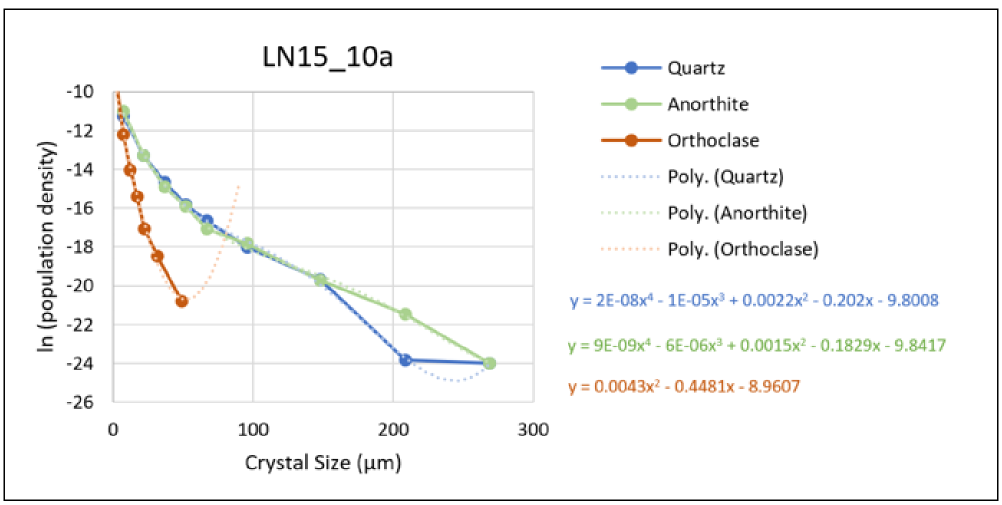

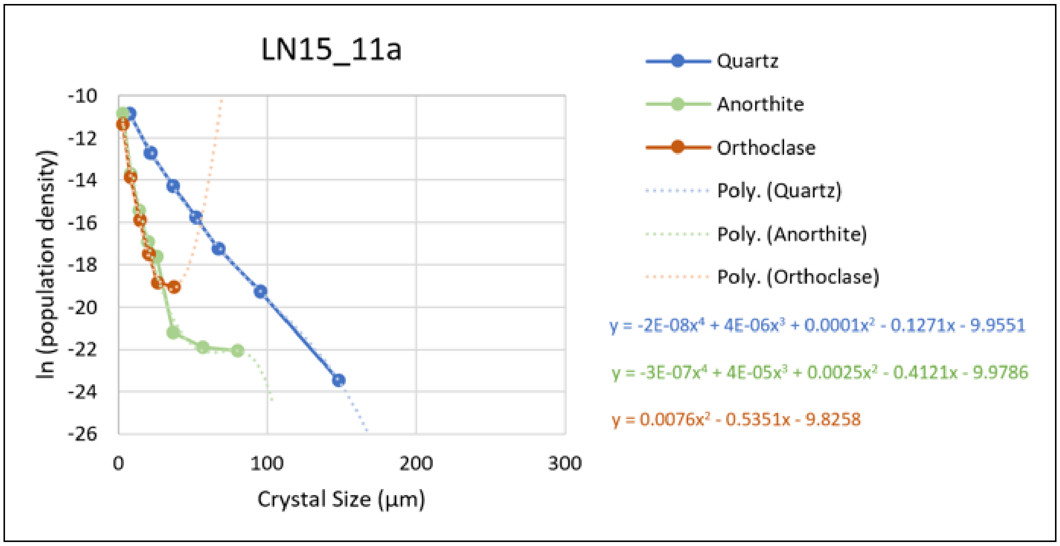
LN15_11a
-10
-12
-14
-16
-18
-20
-22
-24
-26
ln (population density)
0
100
200
300
Crystal Size (µm)
Quartz
Anorthite
Orthoclase
Poly. (Quartz)
Poly. (Anorthite)
Poly. (Orthoclase)
y = -2E-08x⁴ + 4E-06x³ + 0.0001x² - 0.1271x - 9.9551
y = -3E-07x⁴ + 4E-05x³ + 0.0025x² - 0.4121x - 9.9786
y = 0.0076x² - 0.5351x - 9.8258

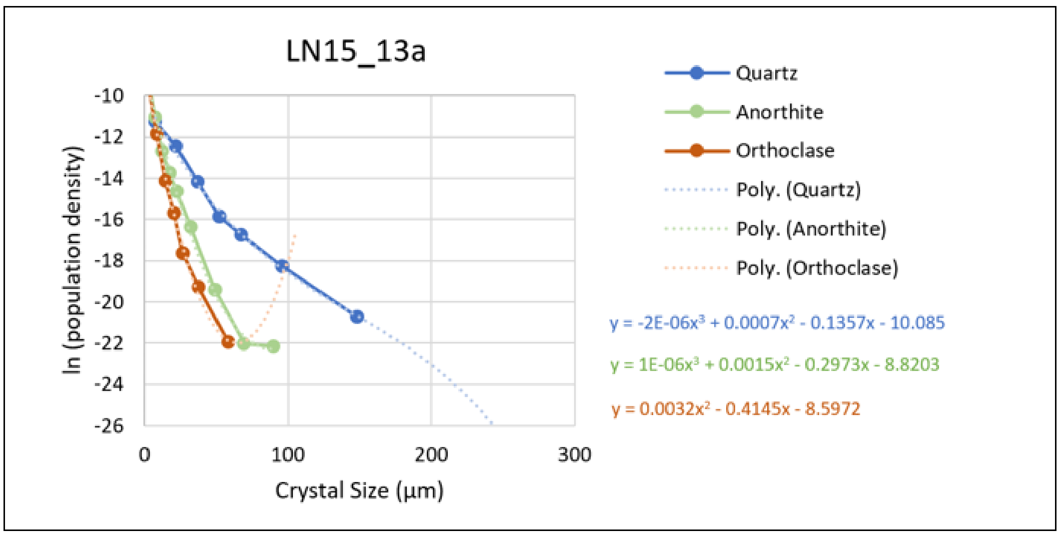
LN15_13a
-10
-12
-14
-16
-18
-20
-22
-24
-26
ln (population density)
0
100
200
300
Crystal Size (µm)
Quartz
Anorthite
Orthoclase
Poly. (Quartz)
Poly. (Anorthite)
Poly. (Orthoclase)
y = -2E-06x³ + 0.0007x² - 0.1357x - 10.085
y = 1E-06x³ + 0.0015x² - 0.2973x - 8.8203
y = 0.0032x² - 0.4145x - 8.5972

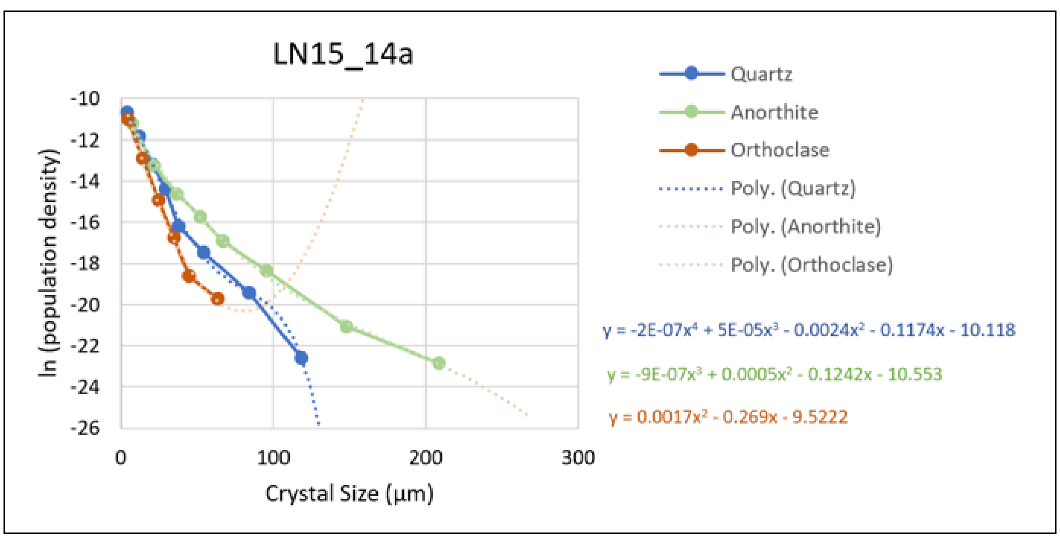
LN15_14a
-10
-12
-14
-16
-18
-20
-22
-24
-26
ln (population density)
0
100
200
300
Crystal Size (µm)
Quartz
Anorthite
Orthoclase
Poly. (Quartz)
Poly. (Anorthite)
Poly. (Orthoclase)
y = -2E-07x⁴ + 5E-05x³ - 0.0024x² - 0.1174x - 10.118
y = -9E-07x³ + 0.0005x² - 0.1242x - 10.553
y = 0.0017x² - 0.269x - 9.5222

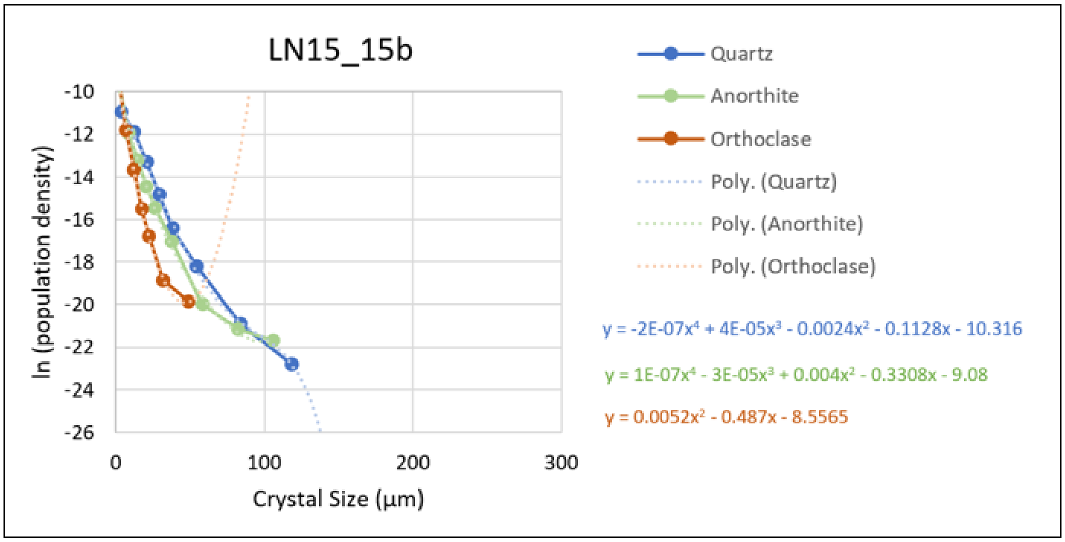
LN15_15b
ln (population density)
Crystal Size (µm)
Quartz
Anorthite
Orthoclase
Poly. (Quartz)
Poly. (Anorthite)
Poly. (Orthoclase)
y = -2E-07x⁴ + 4E-05x³ - 0.0024x² - 0.1128x - 10.316
y = 1E-07x⁴ - 3E-05x³ + 0.004x² - 0.3308x - 9.08
y = 0.0052x² - 0.487x - 8.5565

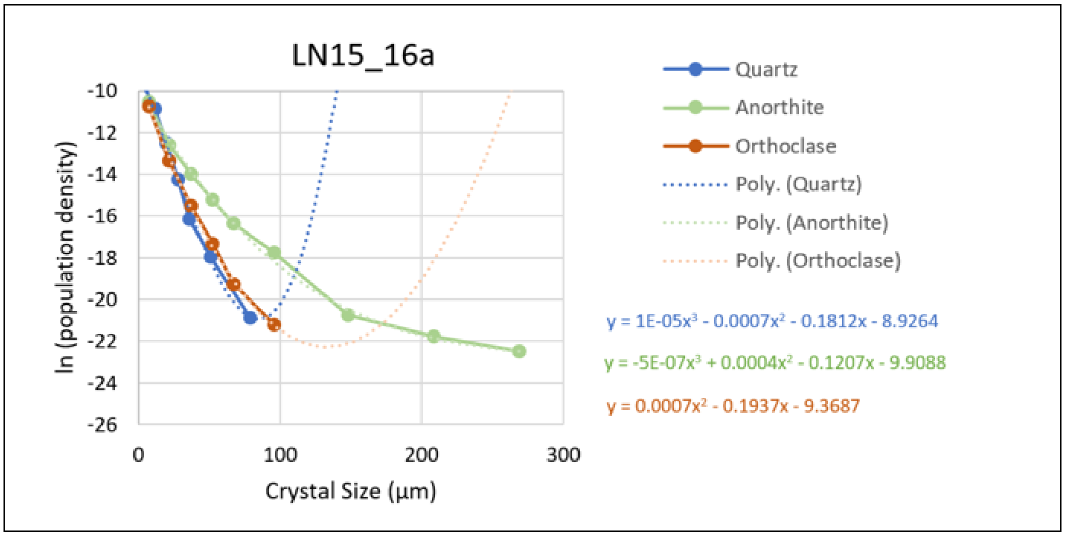
LN15_16a
ln (population density)
Crystal Size (µm)
Quartz
Anorthite
Orthoclase
Poly. (Quartz)
Poly. (Anorthite)
Poly. (Orthoclase)
y = 1E-05x³ - 0.0007x² - 0.1812x - 8.9264
y = -5E-07x³ + 0.0004x² - 0.1207x - 9.9088
y = 0.0007x² - 0.1937x - 9.3687

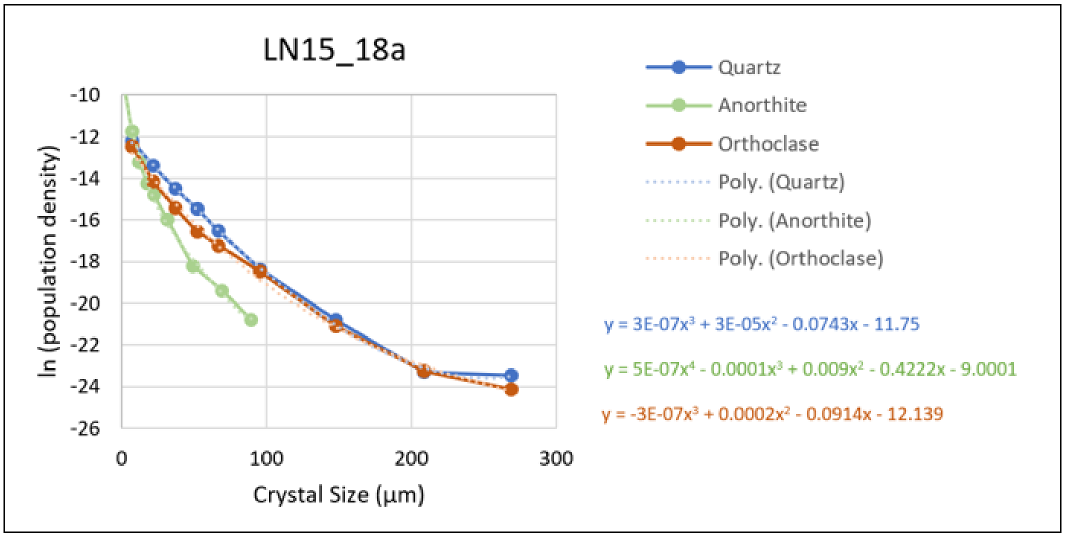
LN15_18a
ln (population density)
Crystal Size (µm)
Quartz
Anorthite
Orthoclase
Poly. (Quartz)
Poly. (Anorthite)
Poly. (Orthoclase)
y = 3E-07x³ + 3E-05x² - 0.0743x - 11.75
y = 5E-07x⁴ - 0.0001x³ + 0.009x² - 0.4222x - 9.0001
y = -3E-07x³ + 0.0002x² - 0.0914x - 12.139

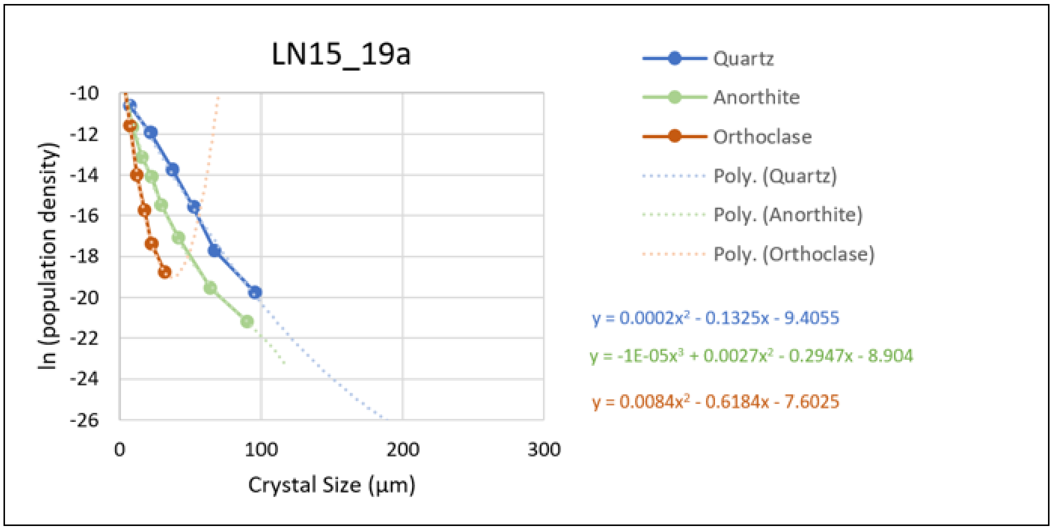
LN15_19a
ln (population density)
Crystal Size (µm)
Quartz
Anorthite
Orthoclase
Poly. (Quartz)
Poly. (Anorthite)
Poly. (Orthoclase)
y = 0.0002x² - 0.1325x - 9.4055
y = -1E-05x³ + 0.0027x² - 0.2947x - 8.904
y = 0.0084x² - 0.6184x - 7.6025

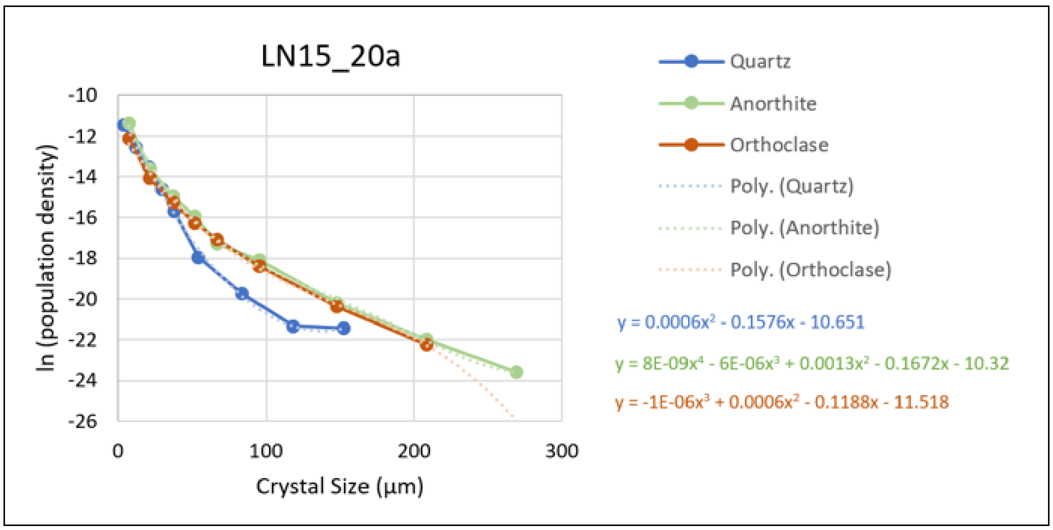
LN15_20a
ln (population density)
Crystal Size (µm)
Quartz
Anorthite
Orthoclase
Poly. (Quartz)
Poly. (Anorthite)
Poly. (Orthoclase)
y = 0.0006x² - 0.1576x - 10.651
y = 8E-09x⁴ - 6E-06x³ + 0.0013x² - 0.1672x - 10.32
y = -1E-06x³ + 0.0006x² - 0.1188x - 11.518

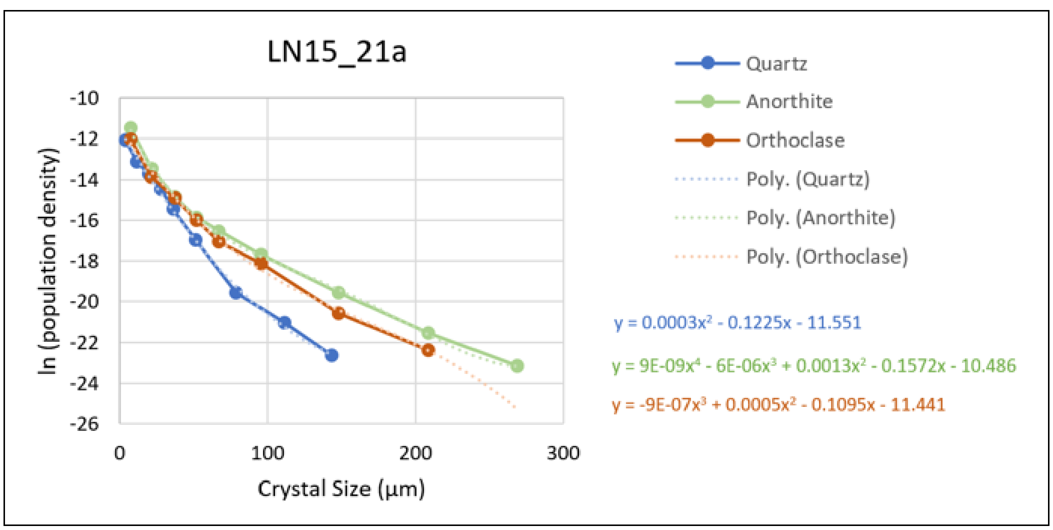
LN15_21a
ln (population density)
Crystal Size (µm)
Quartz
Anorthite
Orthoclase
Poly. (Quartz)
Poly. (Anorthite)
Poly. (Orthoclase)
y = 0.0003x² - 0.1225x - 11.551
y = 9E-09x⁴ - 6E-06x³ + 0.0013x² - 0.1572x - 10.486
y = -9E-07x³ + 0.0005x² - 0.1095x - 11.441

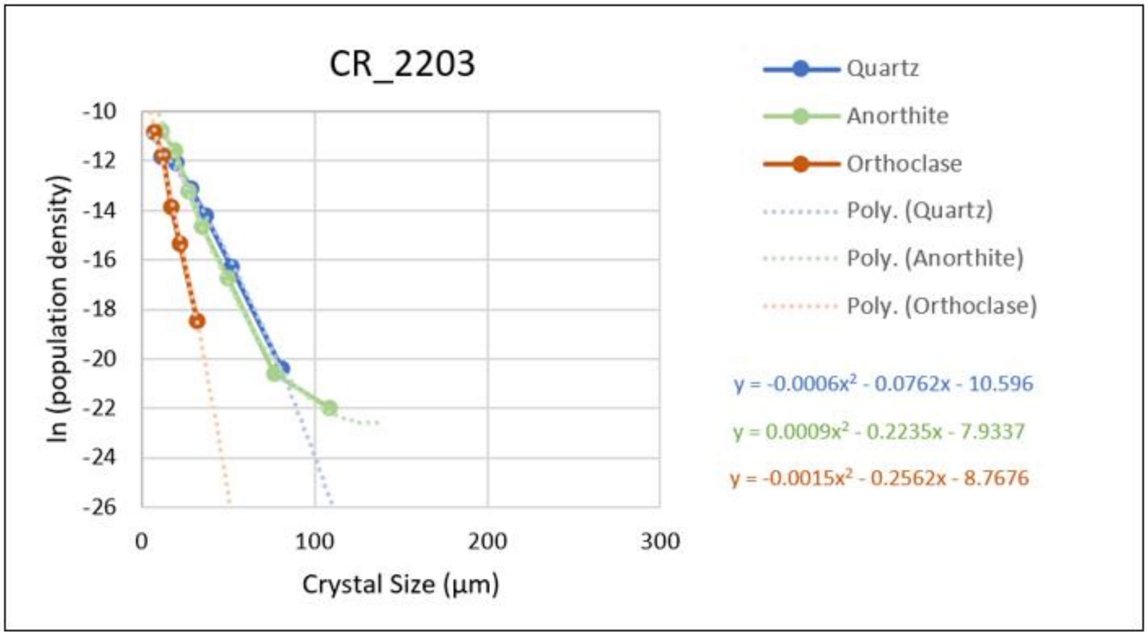
CR_2203
Quartz
Anorthite
Orthoclase
Poly. (Quartz)
Poly. (Anorthite)
Poly. (Orthoclase)
y = -0.0006x² - 0.0762x - 10.596
y = 0.0009x² - 0.2235x - 7.9337
y = -0.0015x² - 0.2562x - 8.7676
ln (population density)
Crystal Size (µm)
-10
-12
-14
-16
-18
-20
-22
-24
-26
0
100
200
300

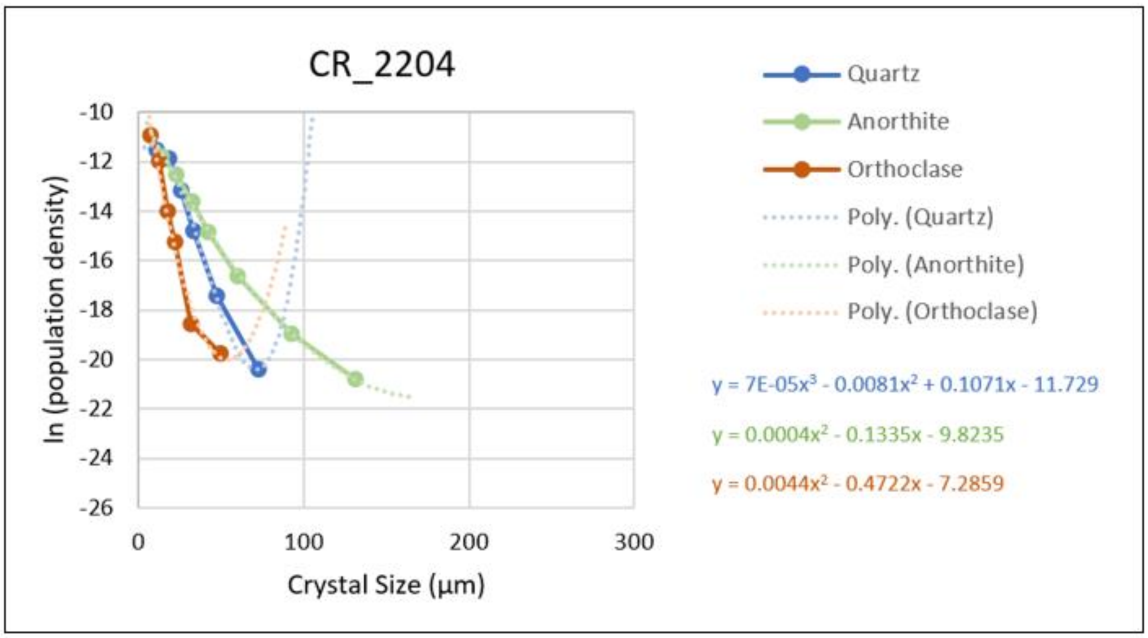
CR_2204
Quartz
Anorthite
Orthoclase
Poly. (Quartz)
Poly. (Anorthite)
Poly. (Orthoclase)
y = 7E-05x³ - 0.0081x² + 0.1071x - 11.729
y = 0.0004x² - 0.1335x - 9.8235
y = 0.0044x² - 0.4722x - 7.2859
ln (population density)
Crystal Size (µm)
-10
-12
-14
-16
-18
-20
-22
-24
-26
0
100
200
300

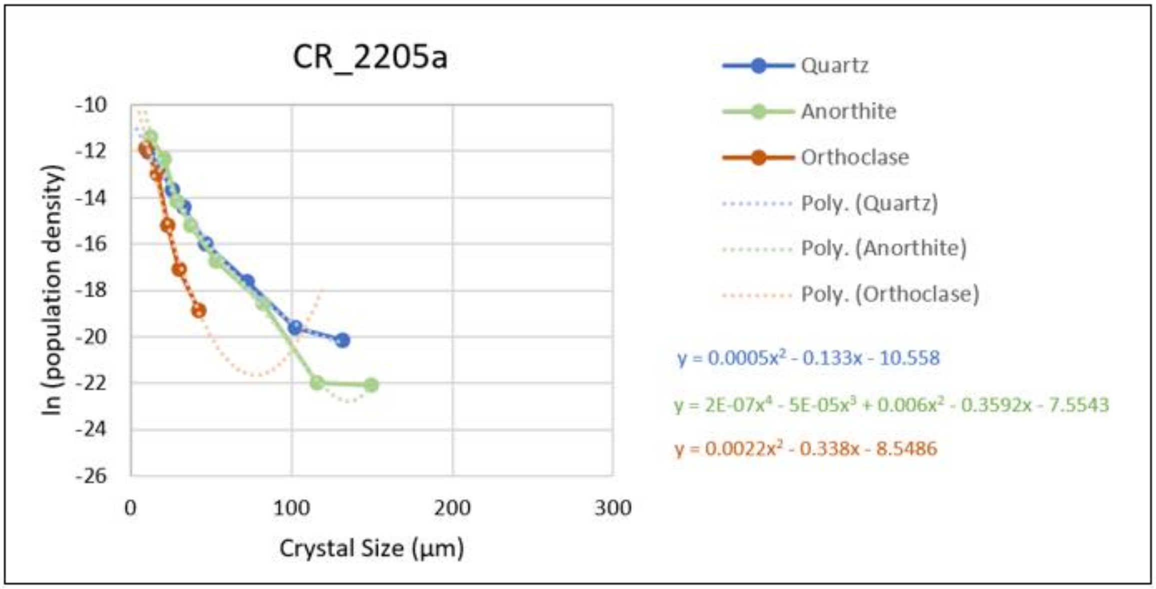
CR_2205a
ln (population density)
-10
-12
-14
-16
-18
-20
-22
-24
-26
0
100
200
300
Crystal Size (µm)
Quartz
Anorthite
Orthoclase
Poly. (Quartz)
Poly. (Anorthite)
Poly. (Orthoclase)
y = 0.0005x² - 0.133x - 10.558
y = 2E-07x⁴ - 5E-05x³ + 0.006x² - 0.3592x - 7.5543
y = 0.0022x² - 0.338x - 8.5486

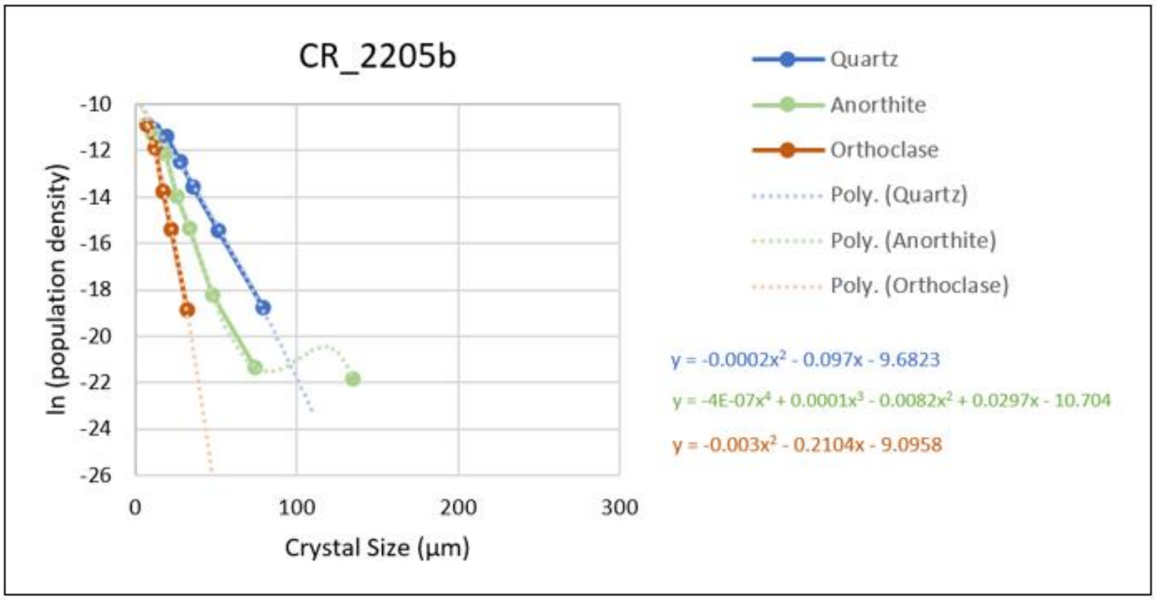
CR_2205b
ln (population density)
-10
-12
-14
-16
-18
-20
-22
-24
-26
0
100
200
300
Crystal Size (µm)
Quartz
Anorthite
Orthoclase
Poly. (Quartz)
Poly. (Anorthite)
Poly. (Orthoclase)
y = -0.0002x² - 0.097x - 9.6823
y = -4E-07x⁴ + 0.0001x³ - 0.0082x² + 0.0297x - 10.704
y = -0.003x² - 0.2104x - 9.0958

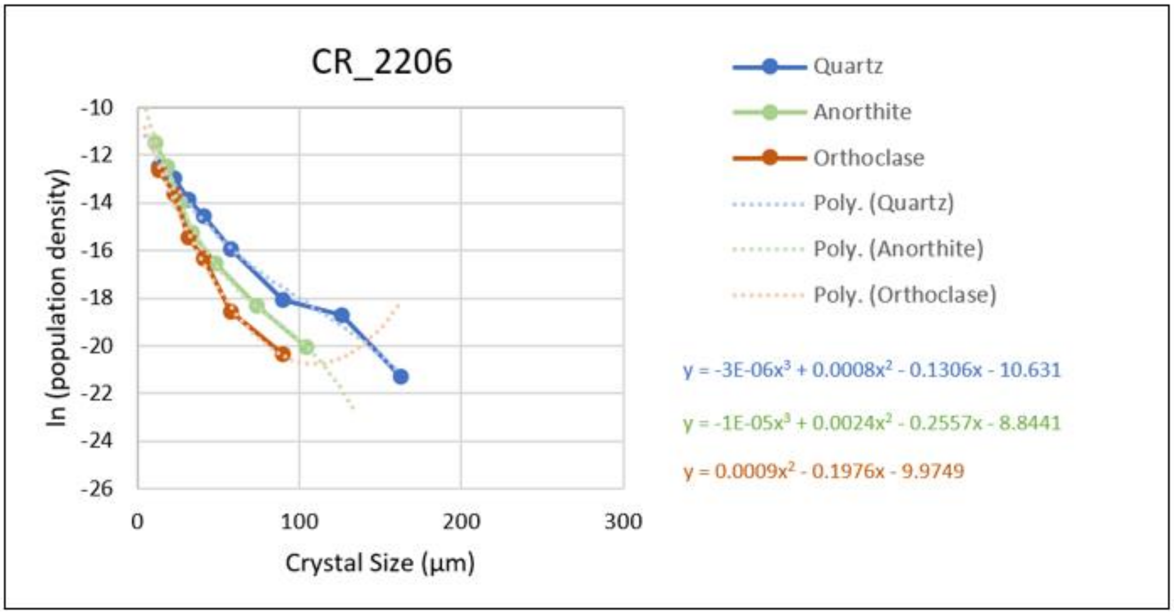
CR_2206
Quartz
Anorthite
Orthoclase
Poly. (Quartz)
Poly. (Anorthite)
Poly. (Orthoclase)
y = -3E-06x³ + 0.0008x² - 0.1306x - 10.631
y = -1E-05x³ + 0.0024x² - 0.2557x - 8.8441
y = 0.0009x² - 0.1976x - 9.9749
ln (population density)
Crystal Size (μm)
-10
-12
-14
-16
-18
-20
-22
-24
-26
0
100
200
300

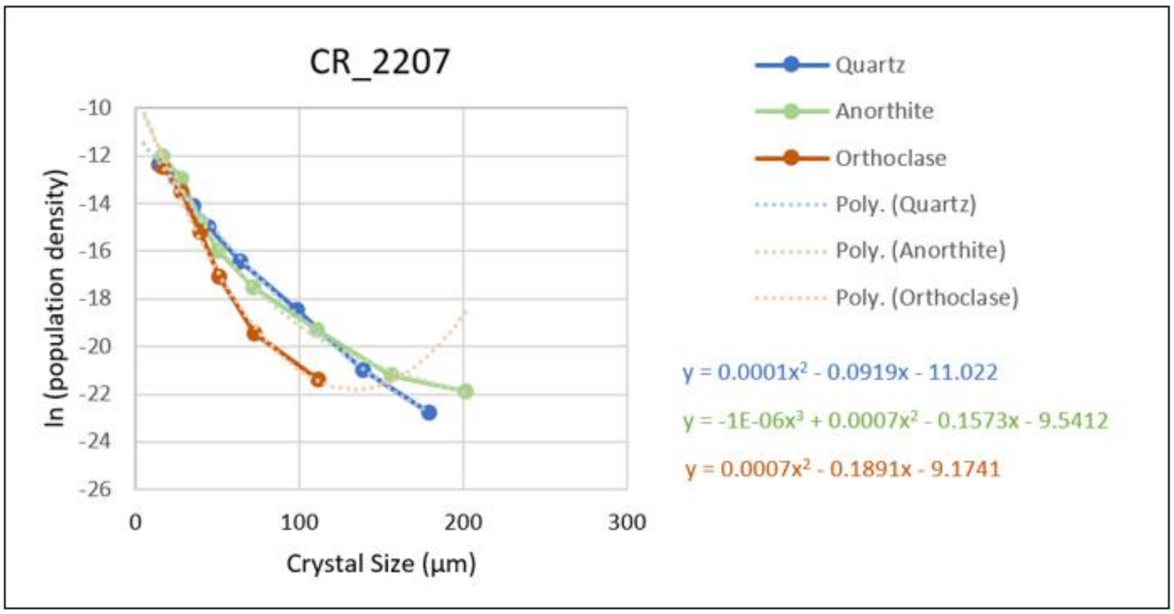
CR_2207
Quartz
Anorthite
Orthoclase
Poly. (Quartz)
Poly. (Anorthite)
Poly. (Orthoclase)
y = 0.0001x² - 0.0919x - 11.022
y = -1E-06x³ + 0.0007x² - 0.1573x - 9.5412
y = 0.0007x² - 0.1891x - 9.1741
ln (population density)
Crystal Size (μm)
-10
-12
-14
-16
-18
-20
-22
-24
-26
0
100
200
300

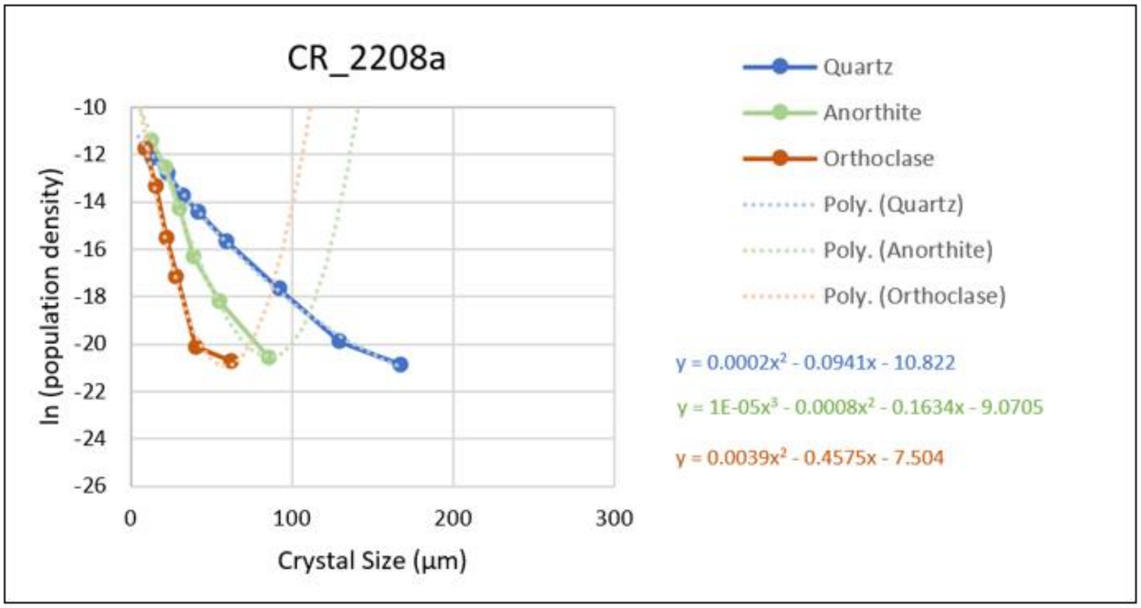
CR_2208a
ln (population density)
Crystal Size (µm)
-10
-12
-14
-16
-18
-20
-22
-24
-26
0
100
200
300
Quartz
Anorthite
Orthoclase
Poly. (Quartz)
Poly. (Anorthite)
Poly. (Orthoclase)
y = 0.0002x² - 0.0941x - 10.822
y = 1E-05x³ - 0.0008x² - 0.1634x - 9.0705
y = 0.0039x² - 0.4575x - 7.504

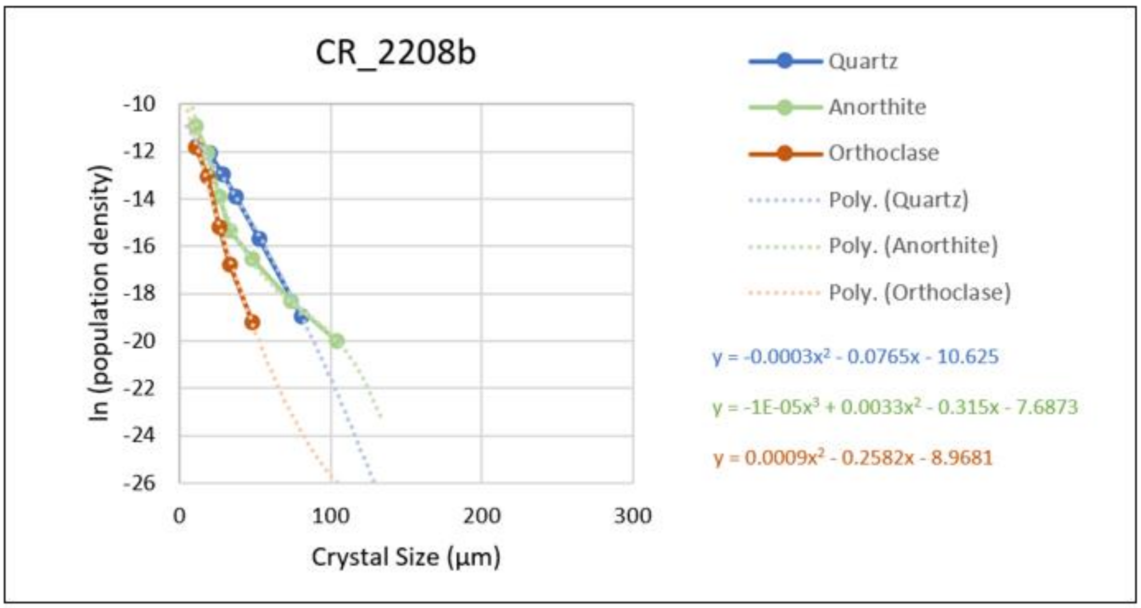
CR_2208b
ln (population density)
Crystal Size (µm)
-10
-12
-14
-16
-18
-20
-22
-24
-26
0
100
200
300
Quartz
Anorthite
Orthoclase
Poly. (Quartz)
Poly. (Anorthite)
Poly. (Orthoclase)
y = -0.0003x² - 0.0765x - 10.625
y = -1E-05x³ + 0.0033x² - 0.315x - 7.6873
y = 0.0009x² - 0.2582x - 8.9681

8.3 Appendix C: EBSD Phase Maps

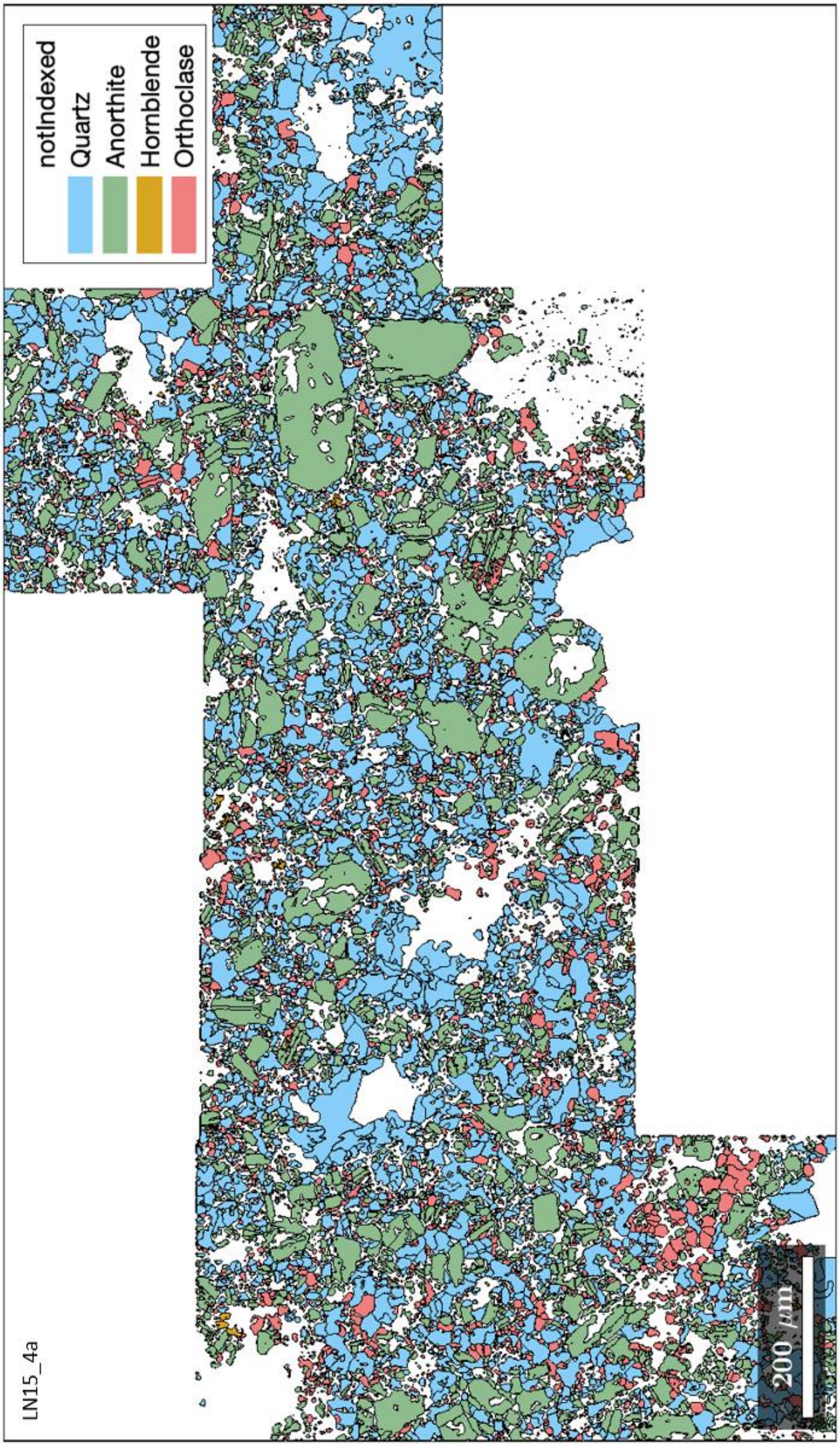
notIndexed
Quartz
Anorthite
Hornblende
Orthoclase
LN15_4a
200 μm

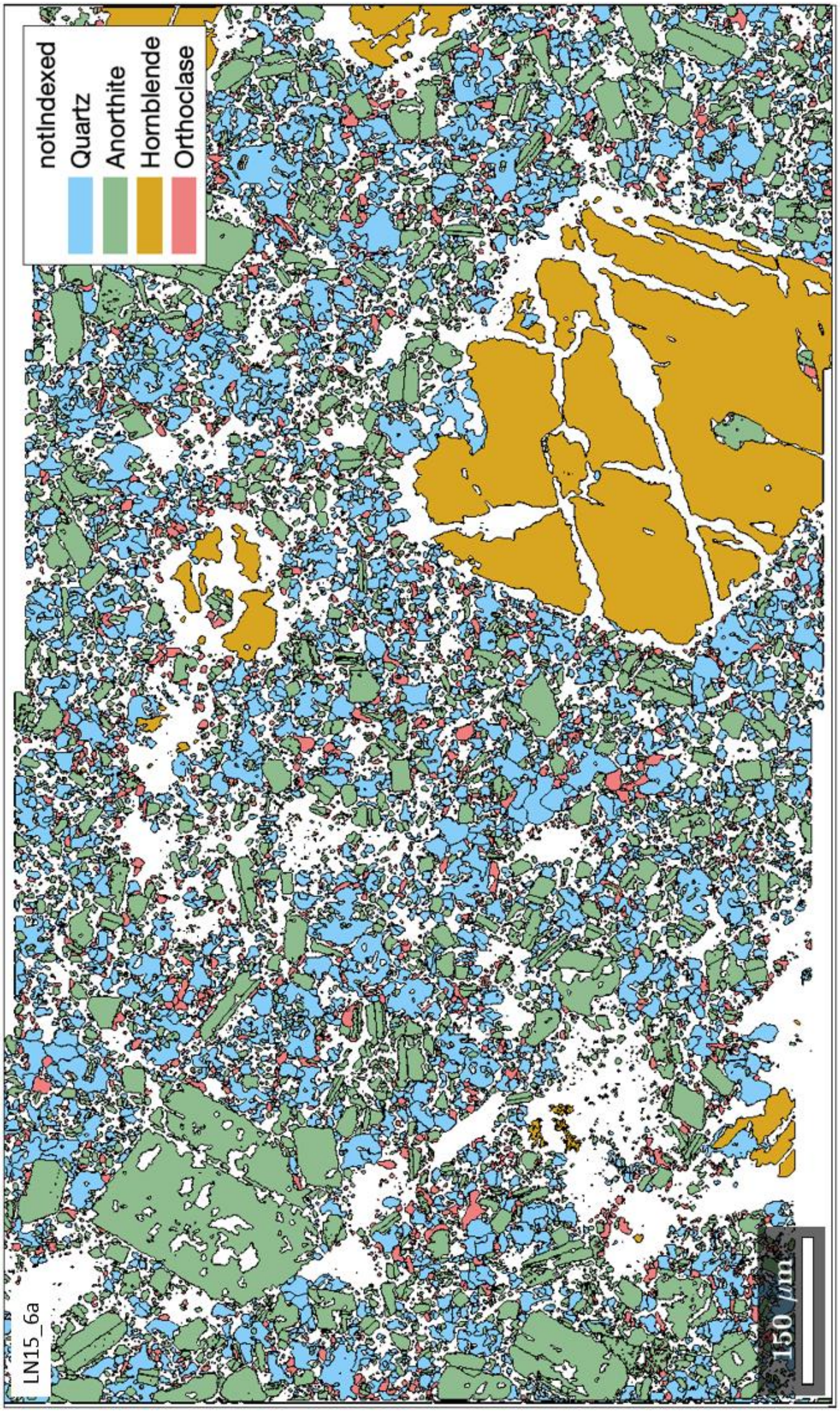
notIndexed
Quartz
Anorthite
Hornblende
Orthoclase
LN15_6a
150 µm

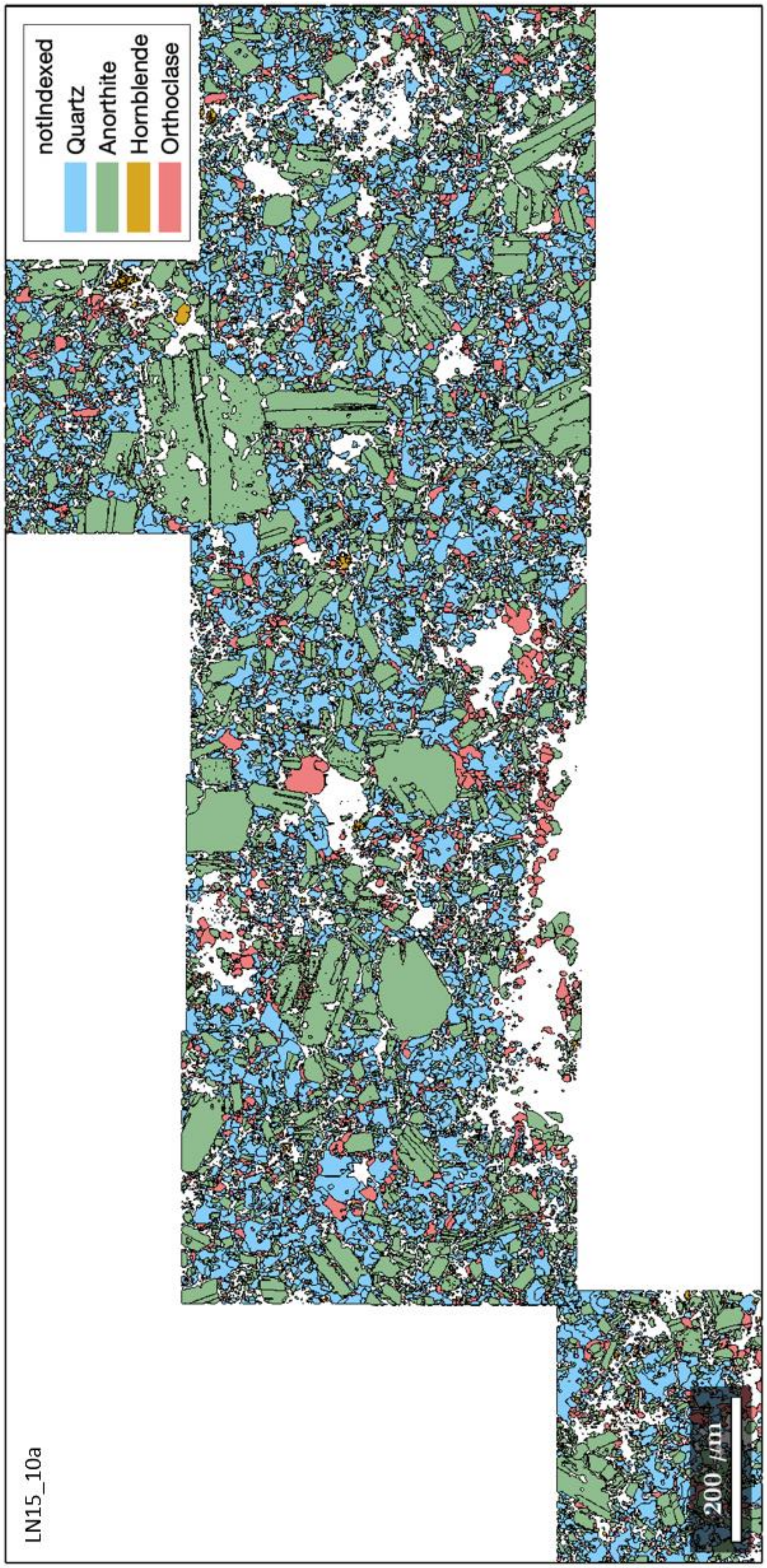
notIndexed
Quartz
Anorthite
Hornblende
Orthoclase
LN15_10a
200 μm

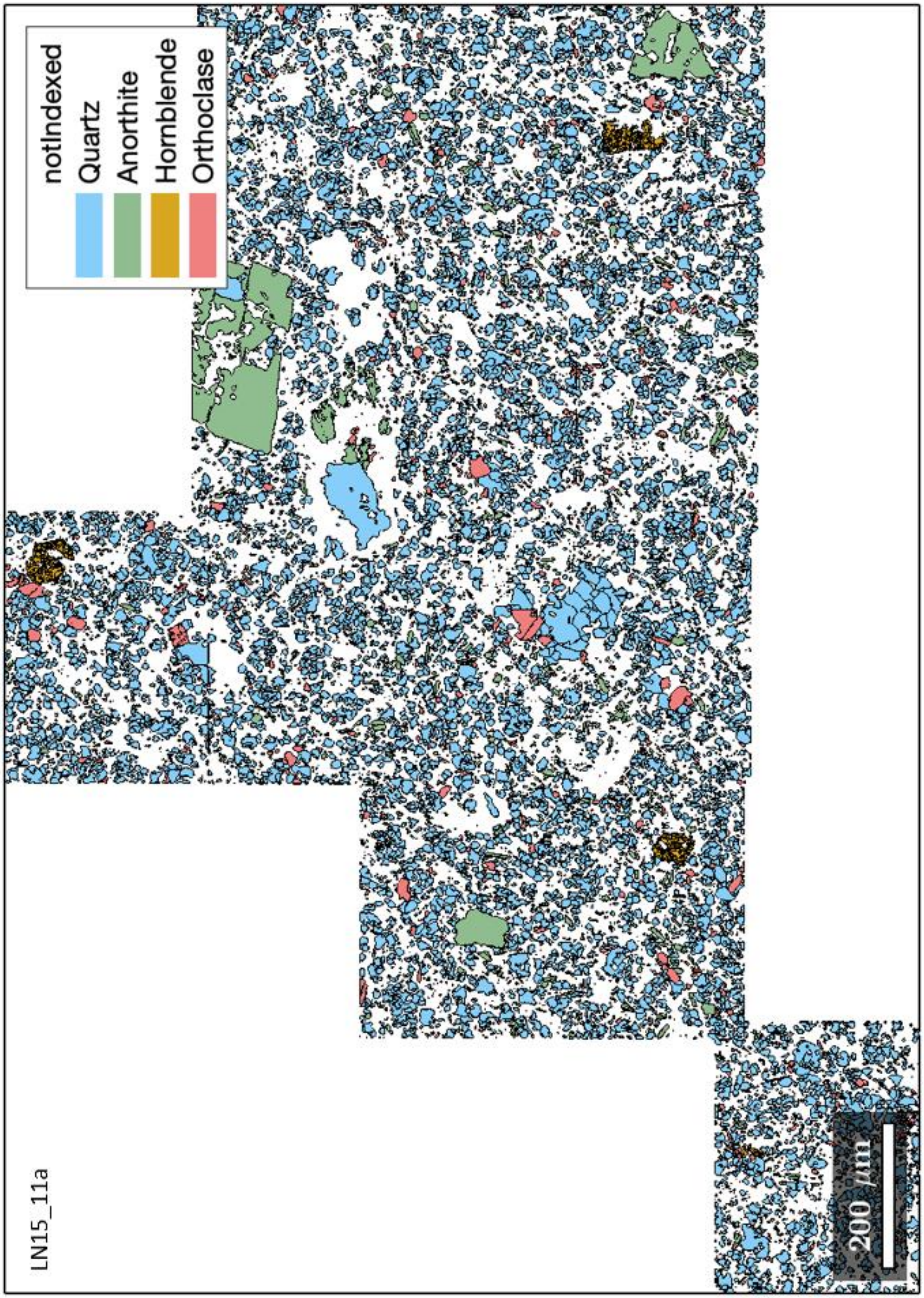
notIndexed
Quartz
Anorthite
Hornblende
Orthoclase
LN15_11a
200 μm

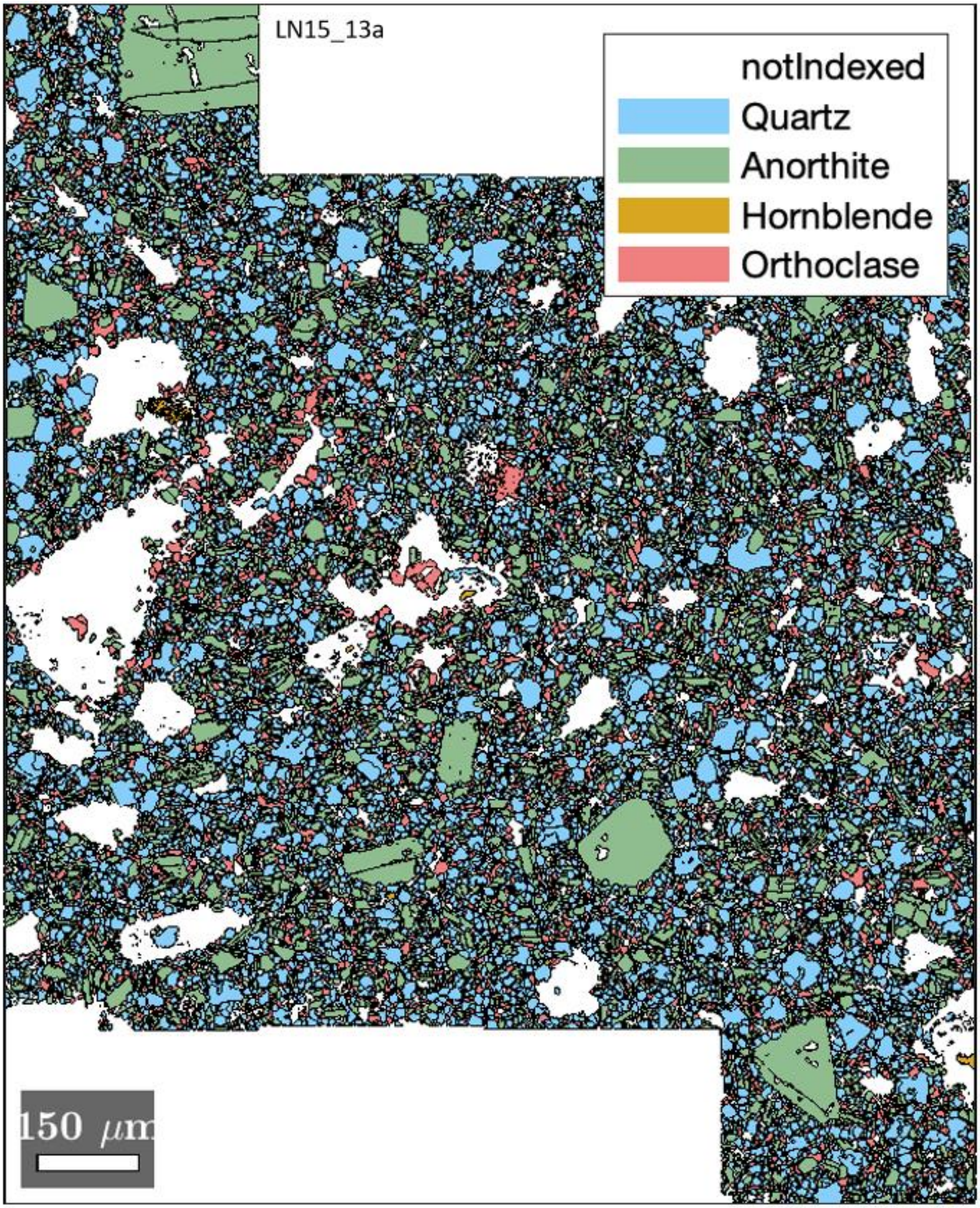
LN15_13a
notIndexed
Quartz
Anorthite
Hornblende
Orthoclase
150 μm

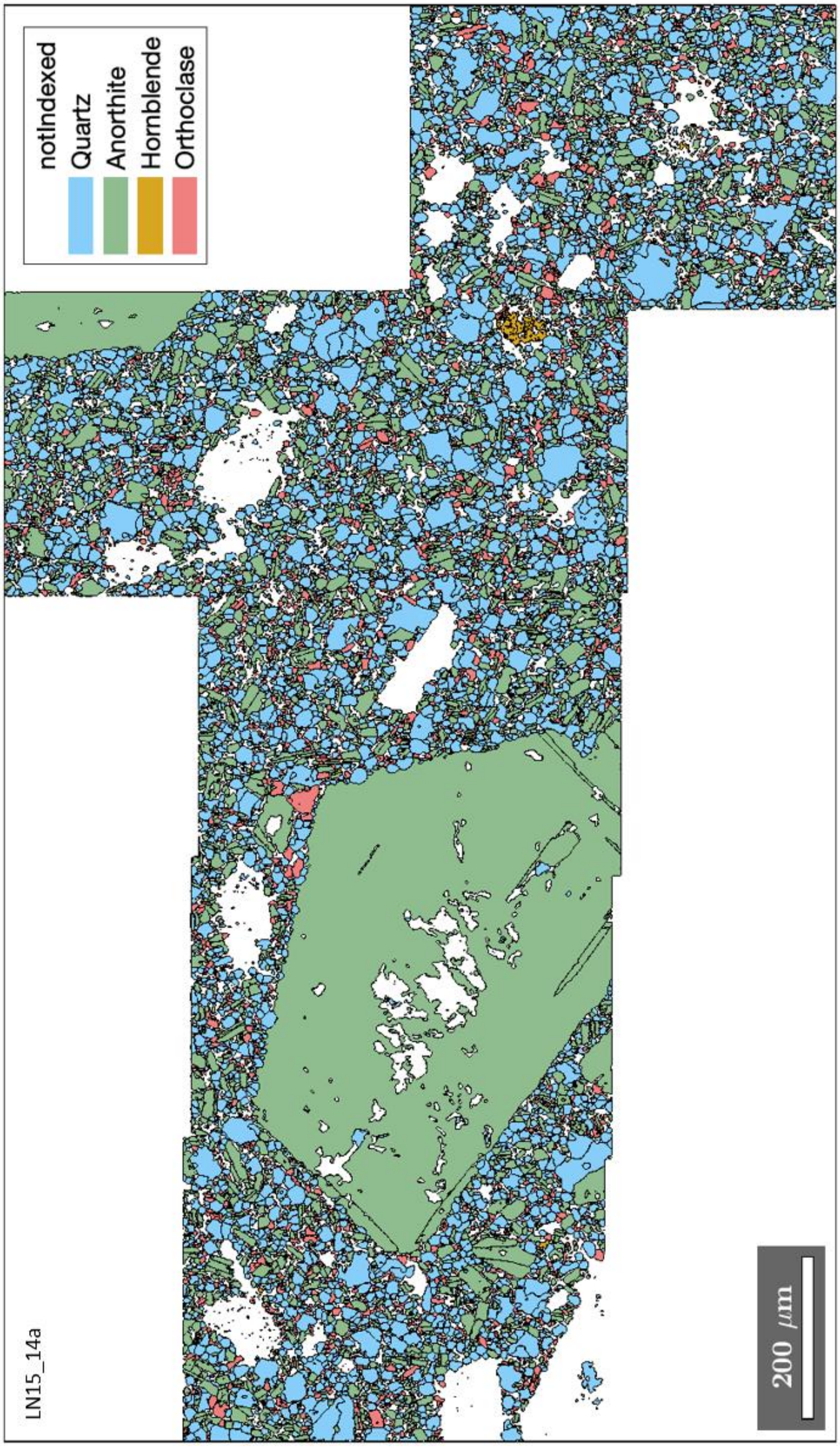
notIndexed
Quartz
Anorthite
Hornblende
Orthoclase
LN15_14a
200 μm

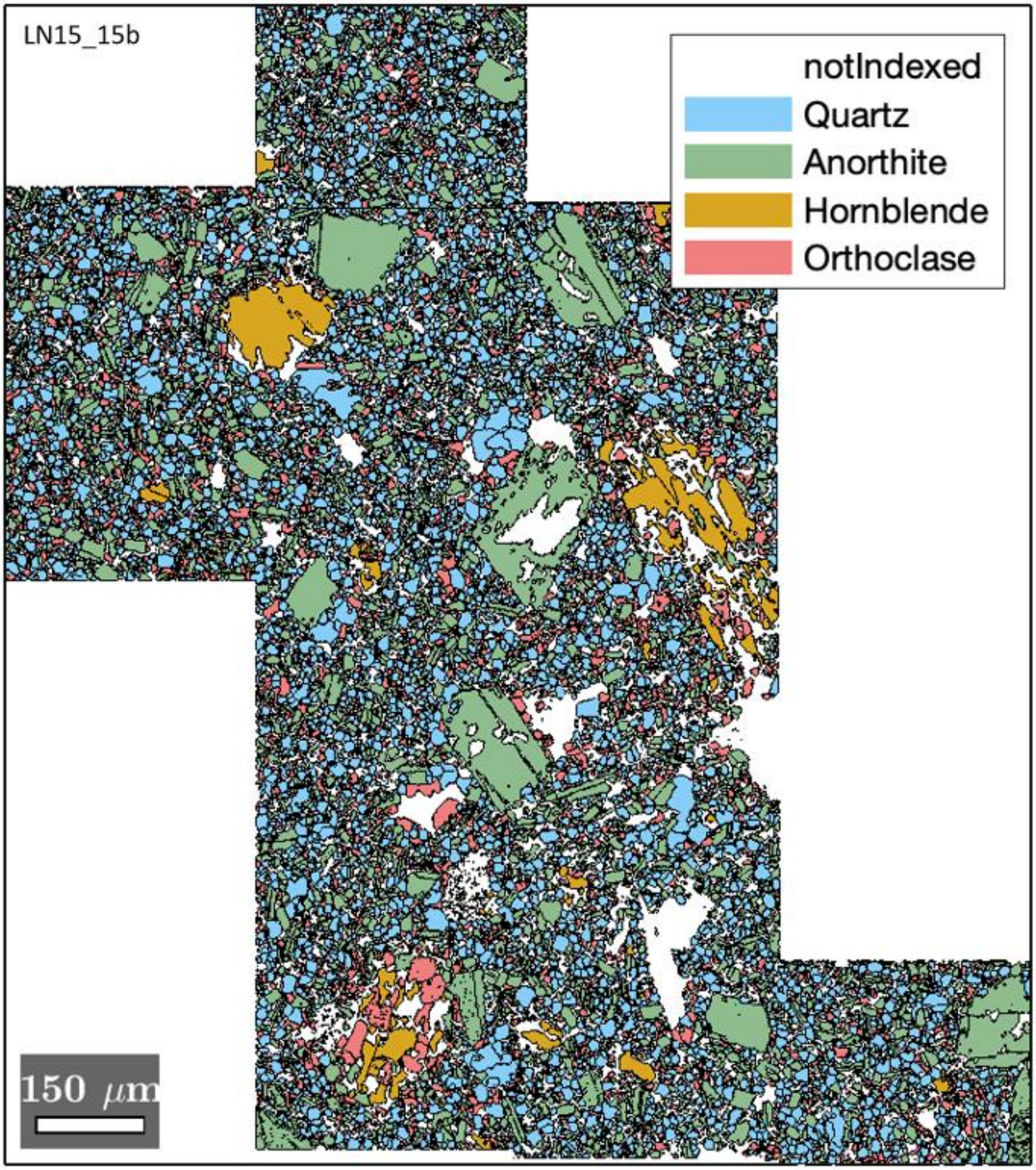
LN15_15b
notIndexed
Quartz
Anorthite
Hornblende
Orthoclase
150 μm

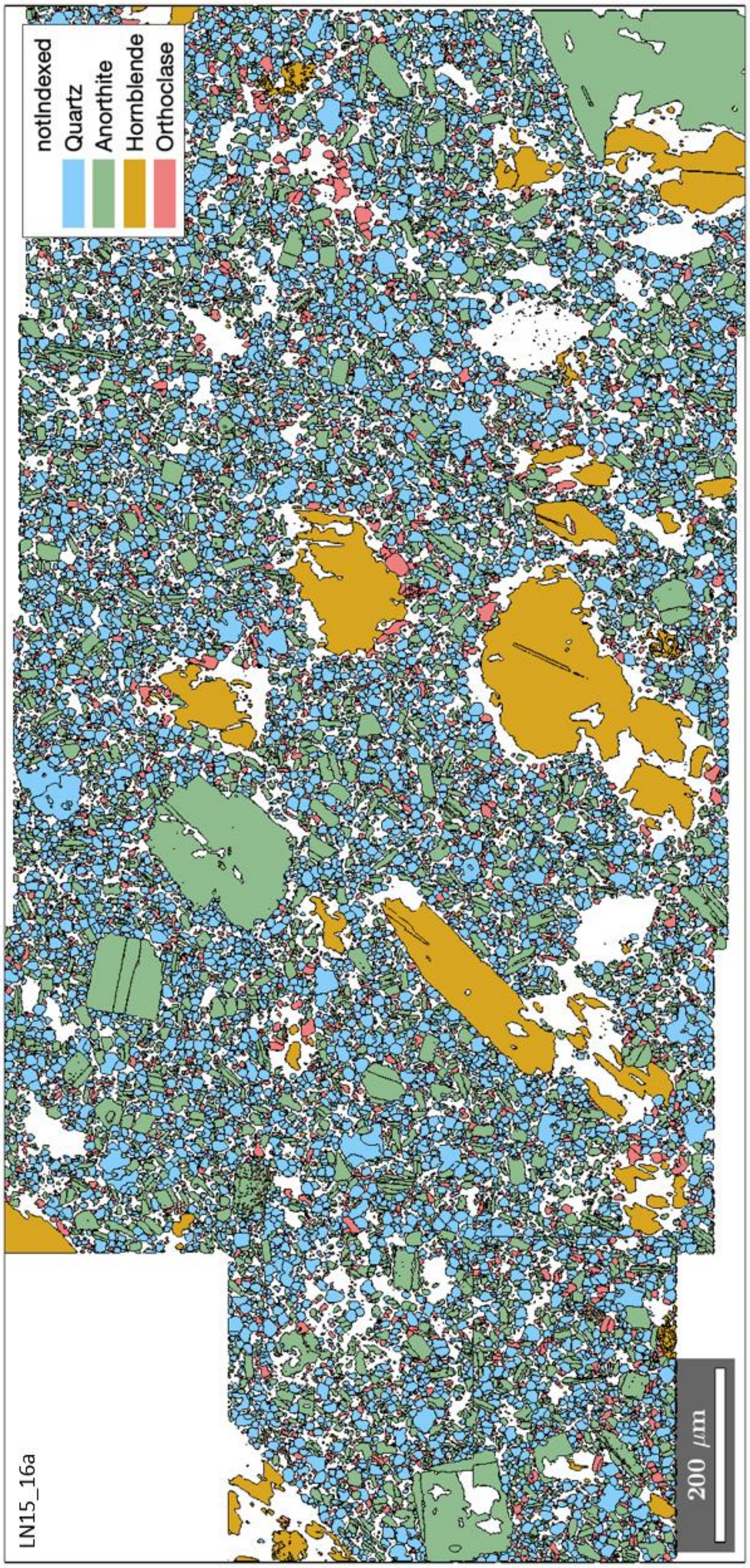
notIndexed
Quartz
Anorthite
Hornblende
Orthoclase
LN15_16a
200 μm

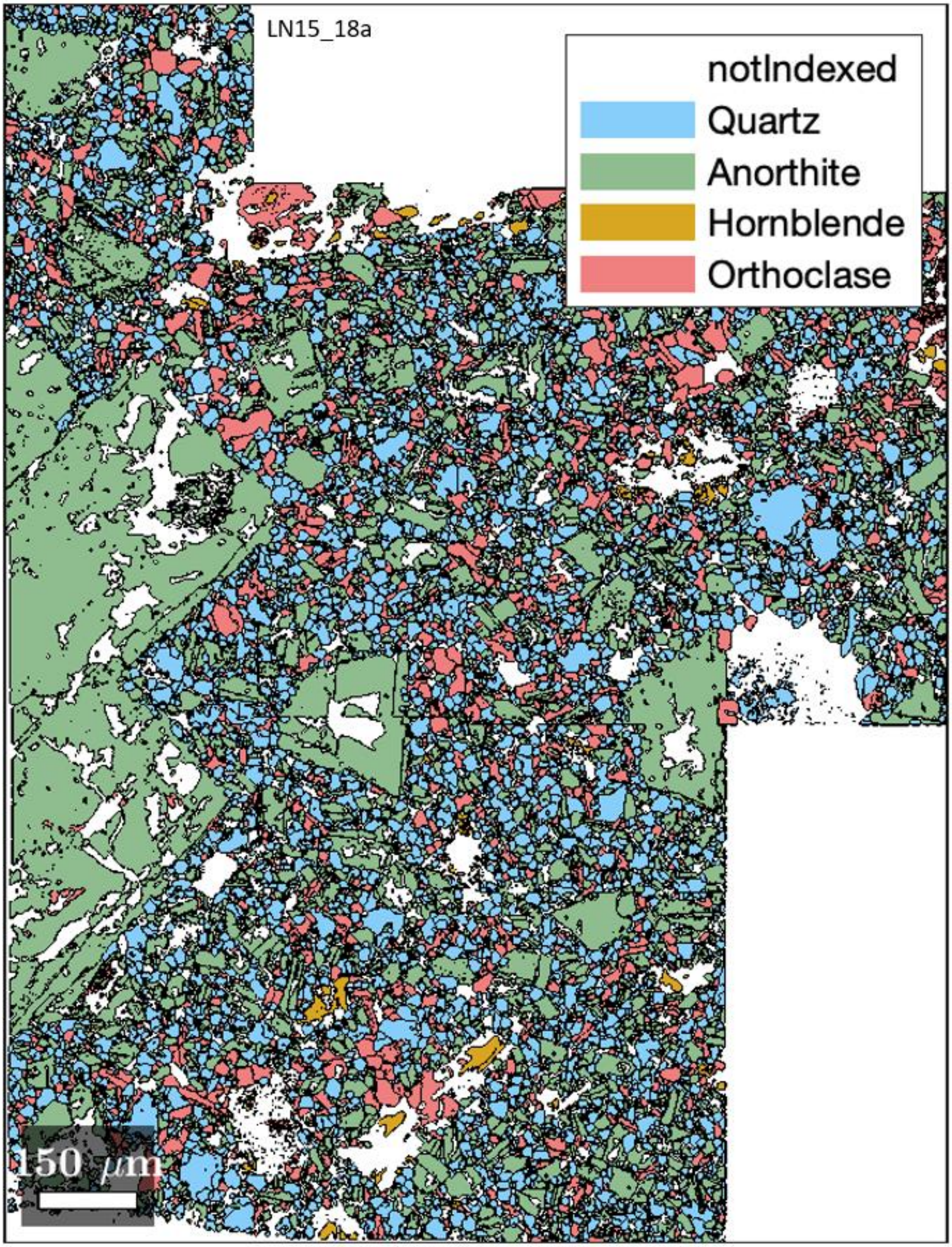
LN15_18a
notIndexed
Quartz
Anorthite
Hornblende
Orthoclase
150 μm

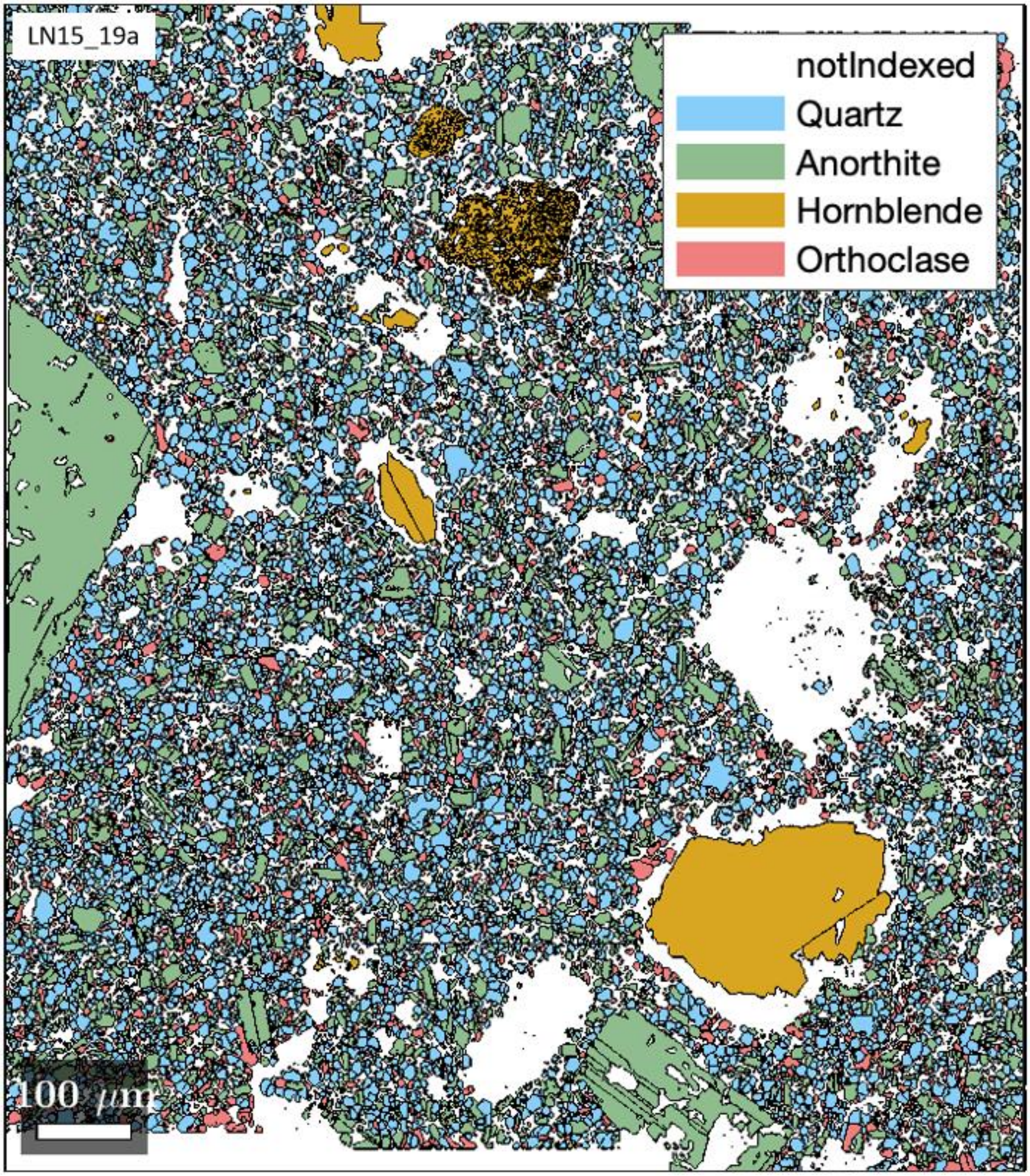
LN15_19a
notIndexed
Quartz
Anorthite
Hornblende
Orthoclase
100 μm

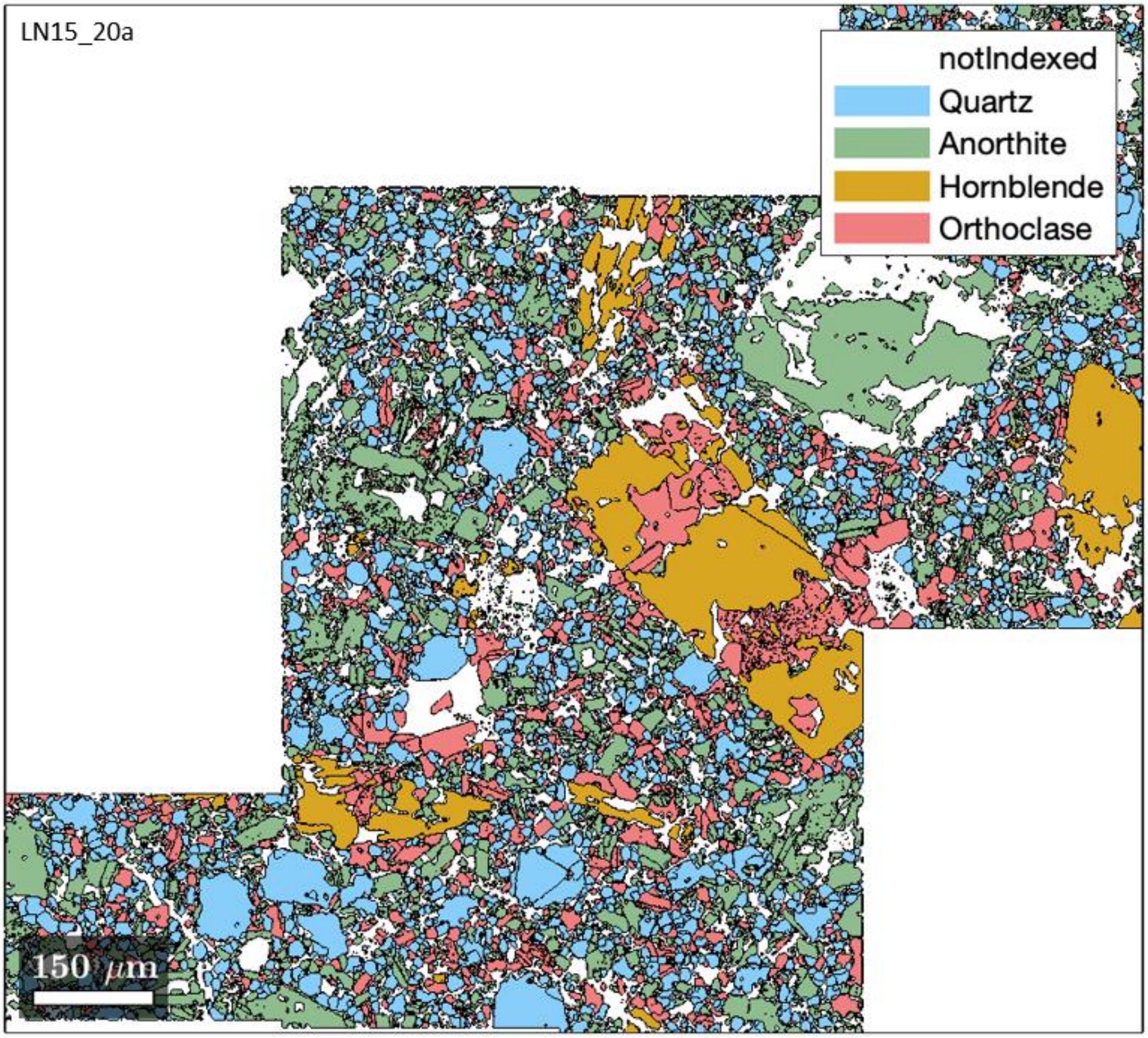
LN15_20a
notIndexed
Quartz
Anorthite
Hornblende
Orthoclase
150 μm

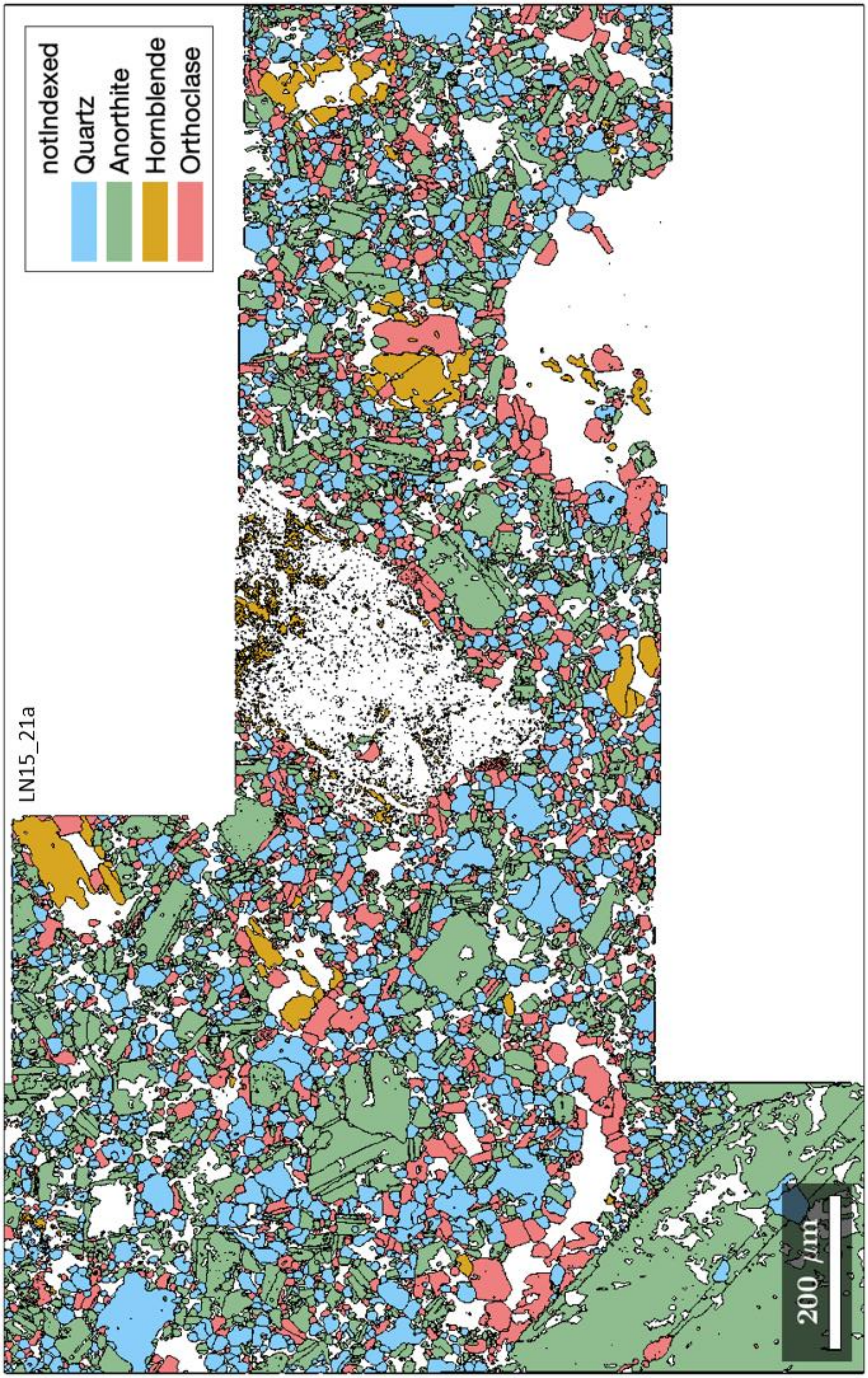
LN15_21a
notIndexed
Quartz
Anorthite
Hornblende
Orthoclase
200 μm

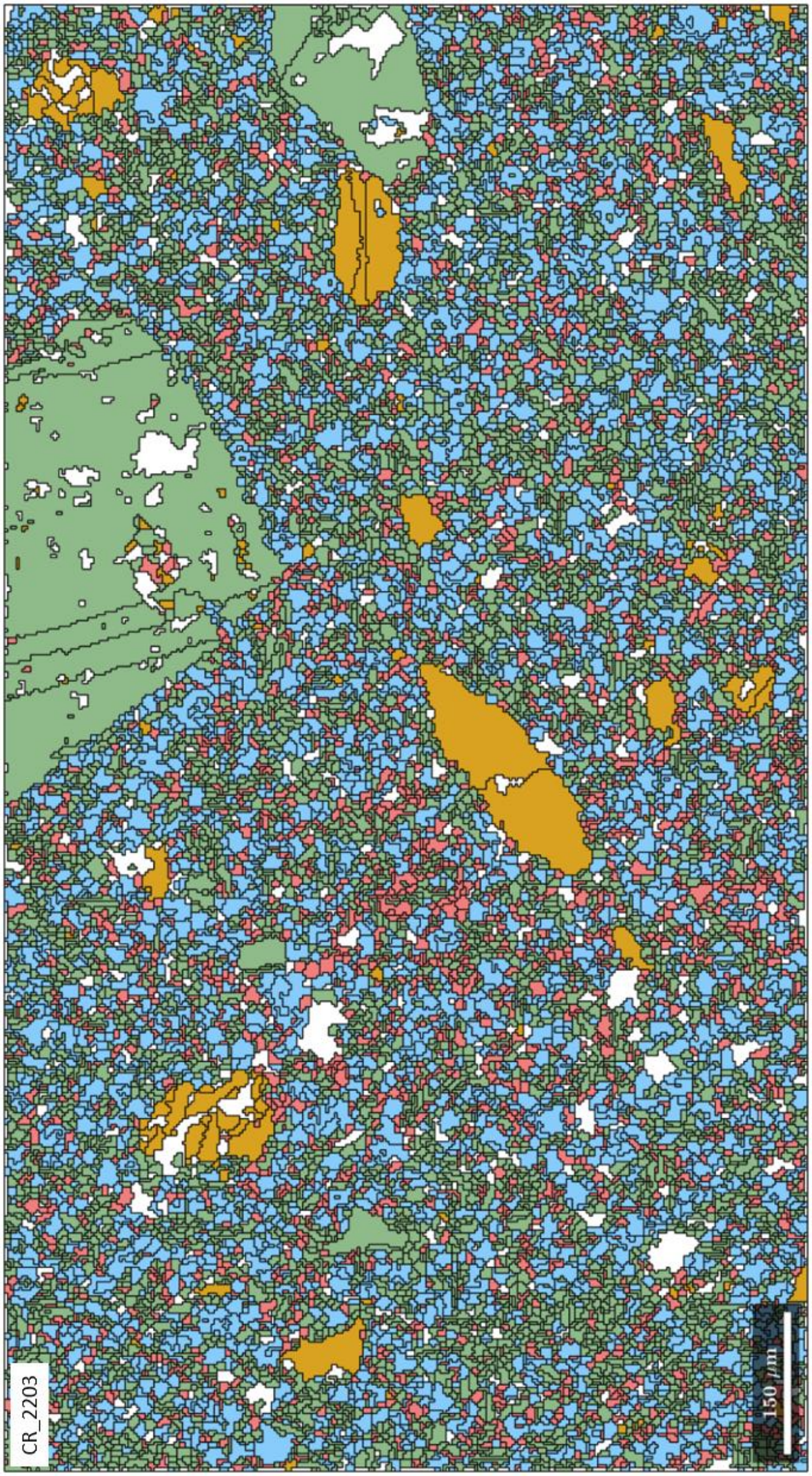
CR_2203
150 μm

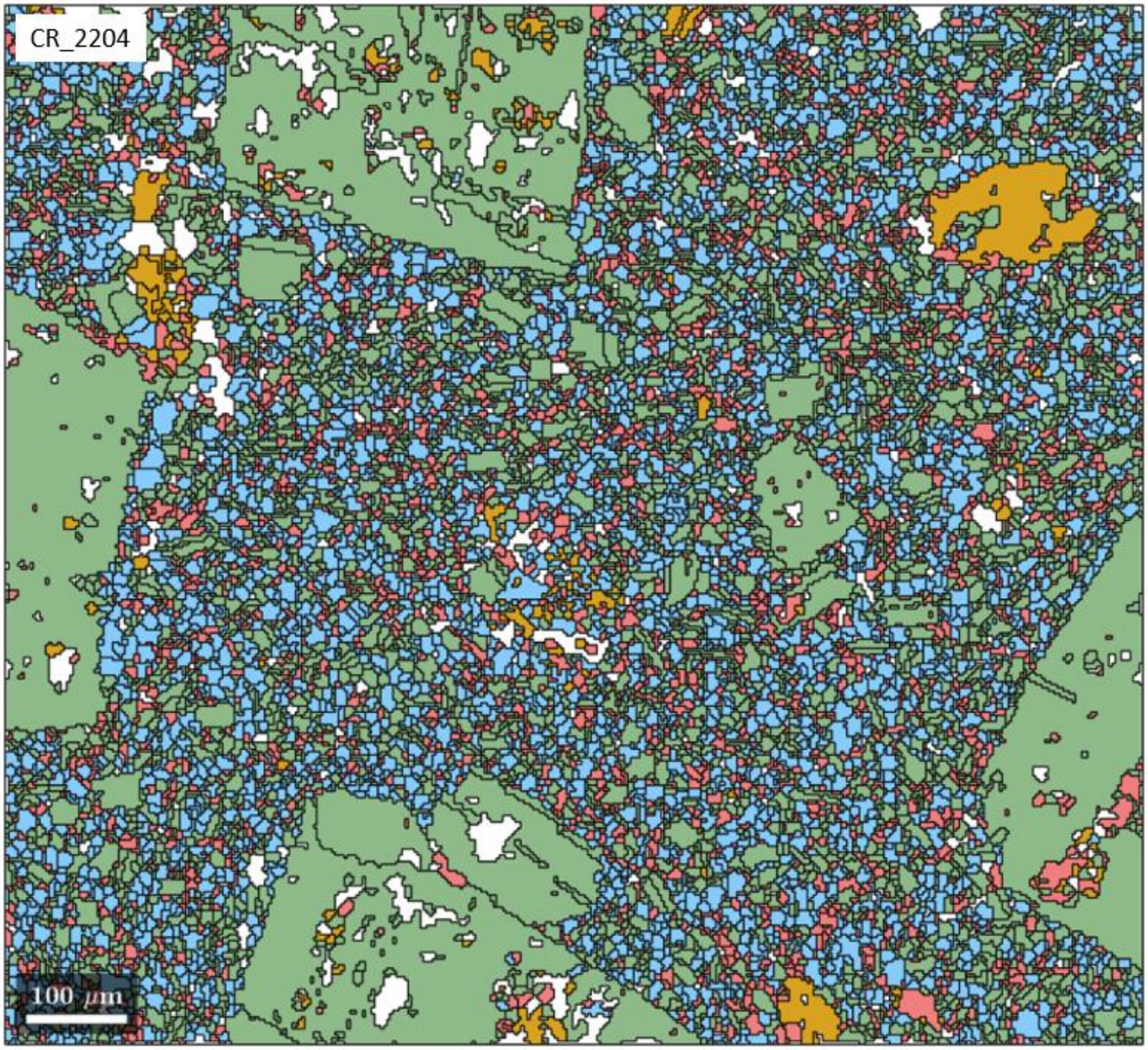
CR_2204
100 μm

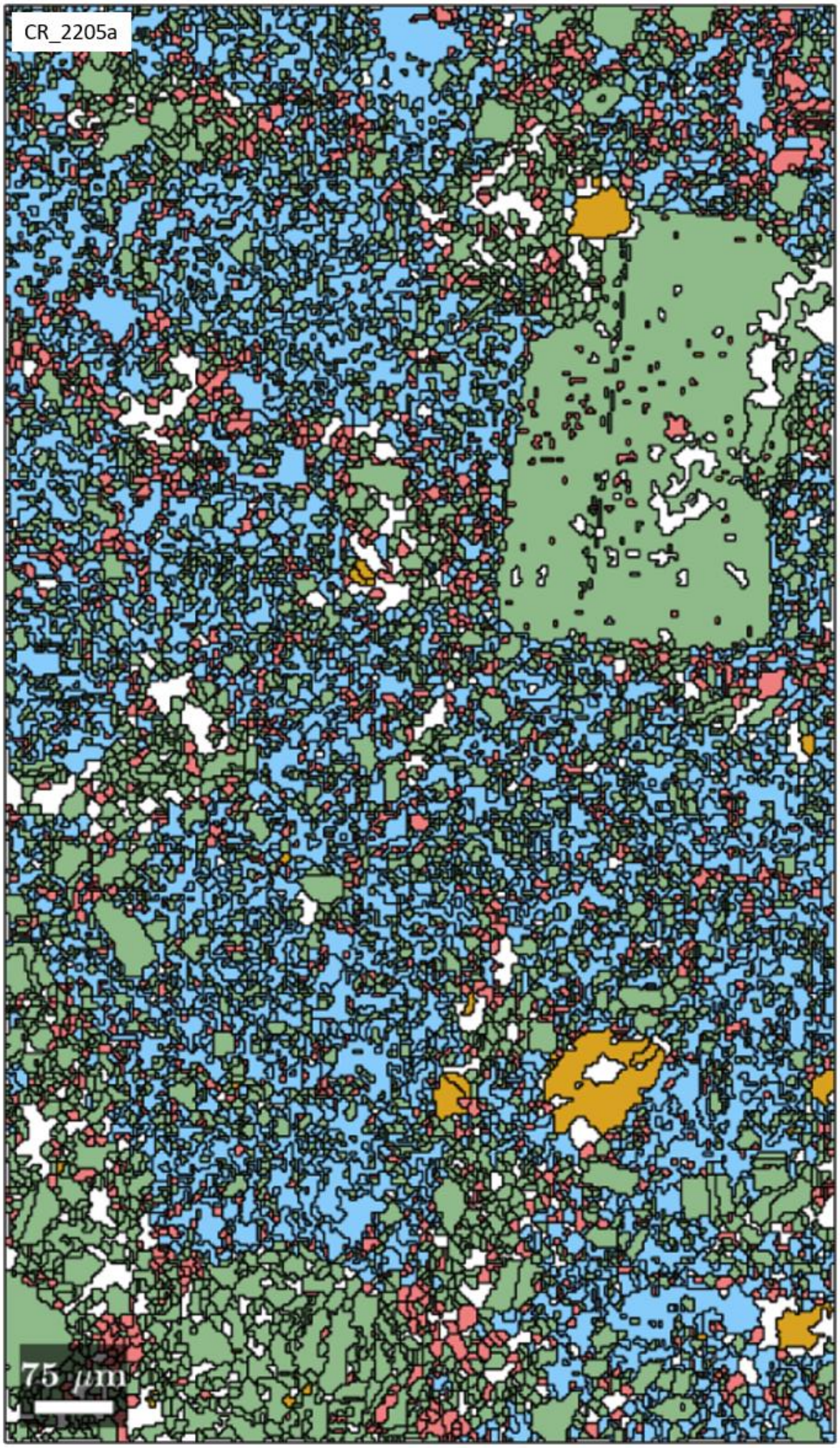
CR_2205a
75 μm

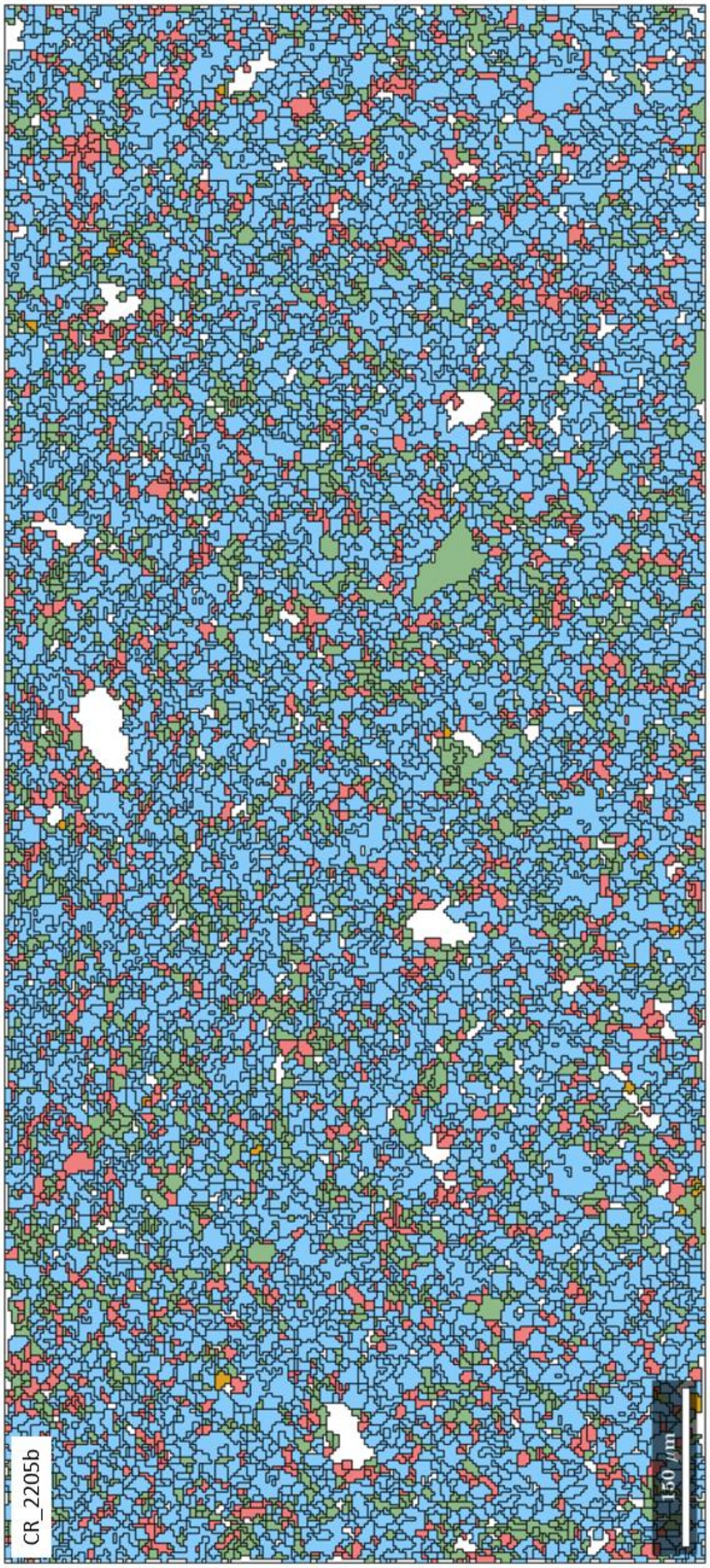
CR_2205b
150 μm

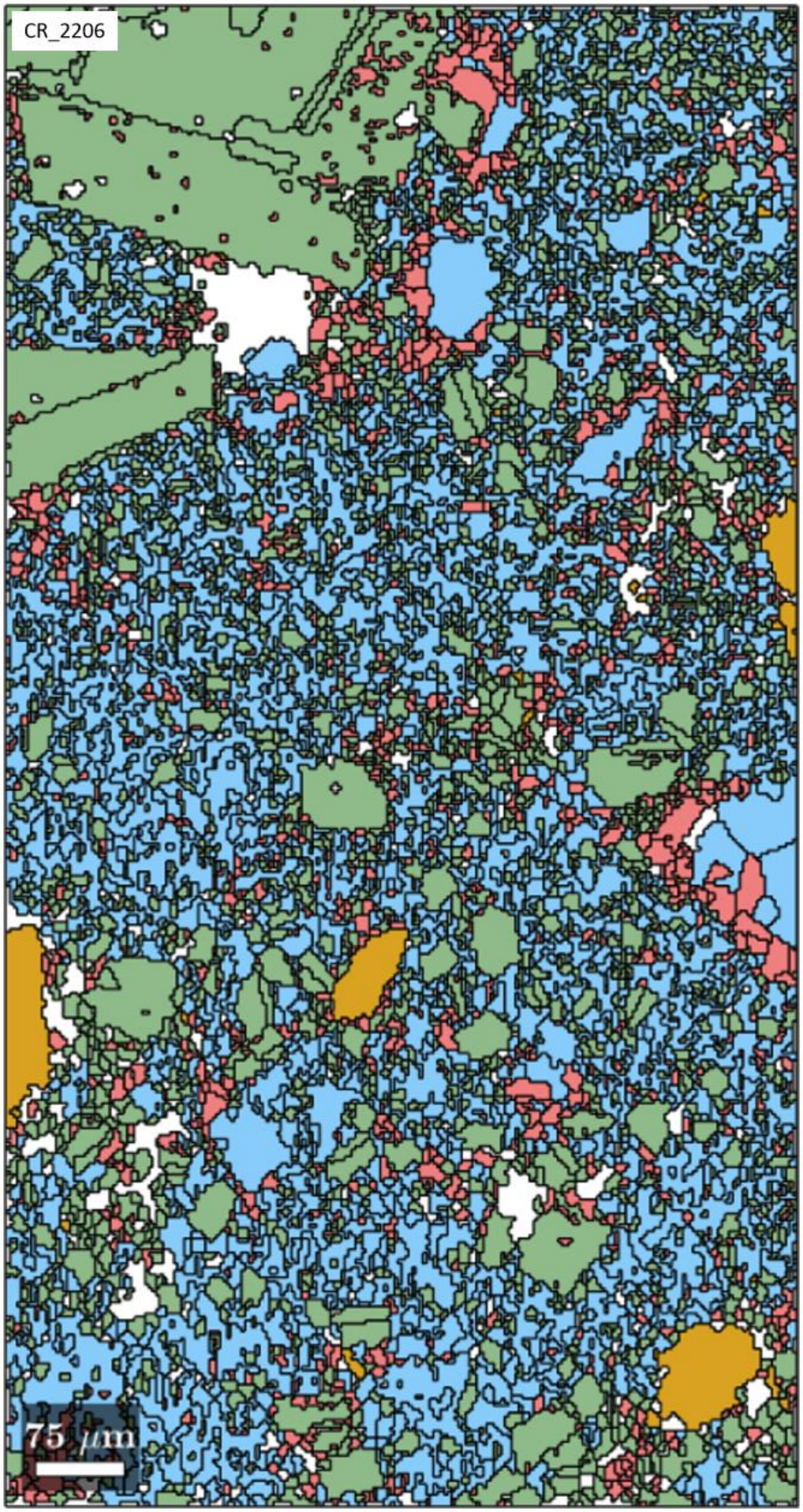
CR_2206
75 μm

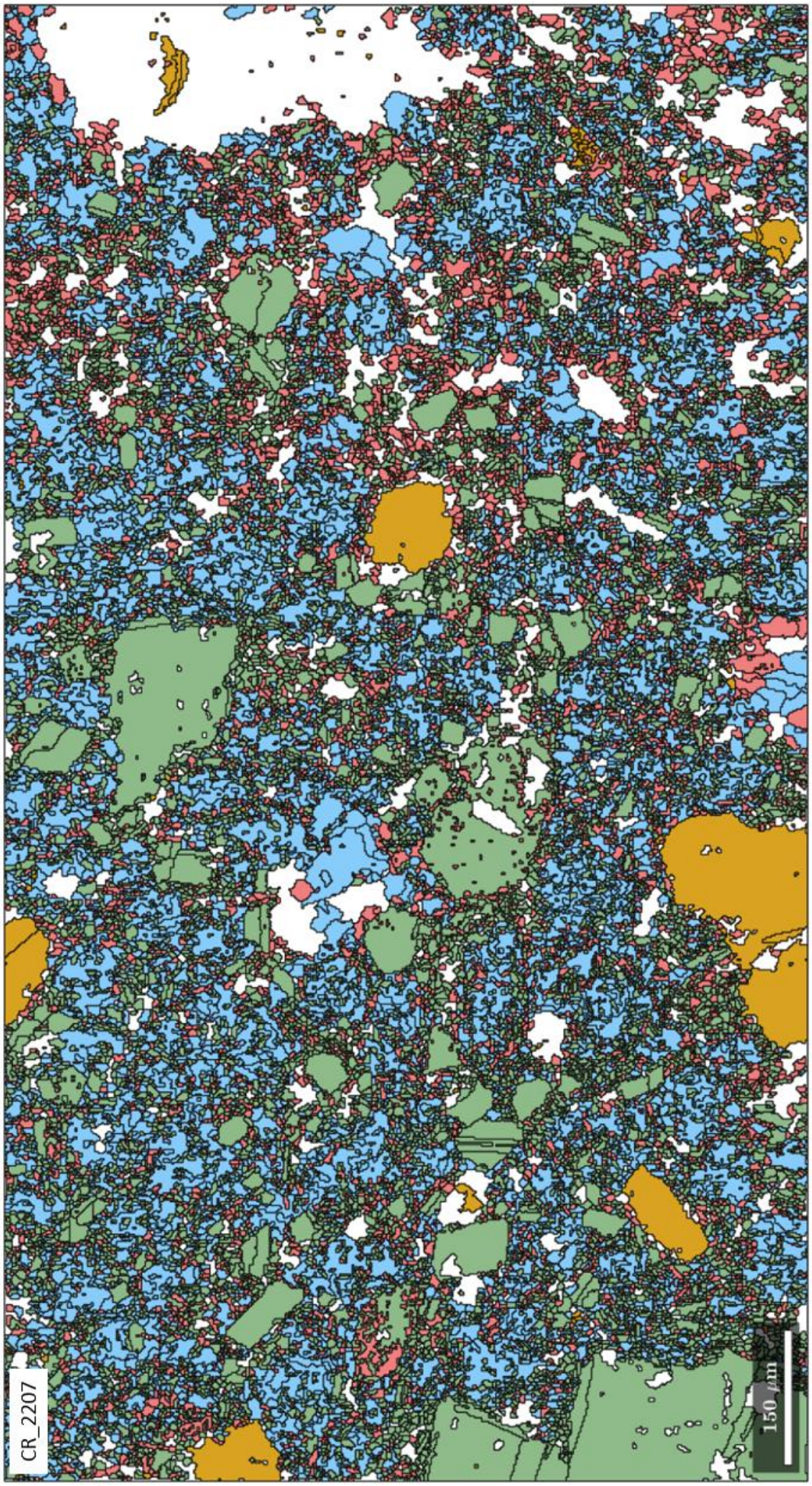
CR_2207
150 μm

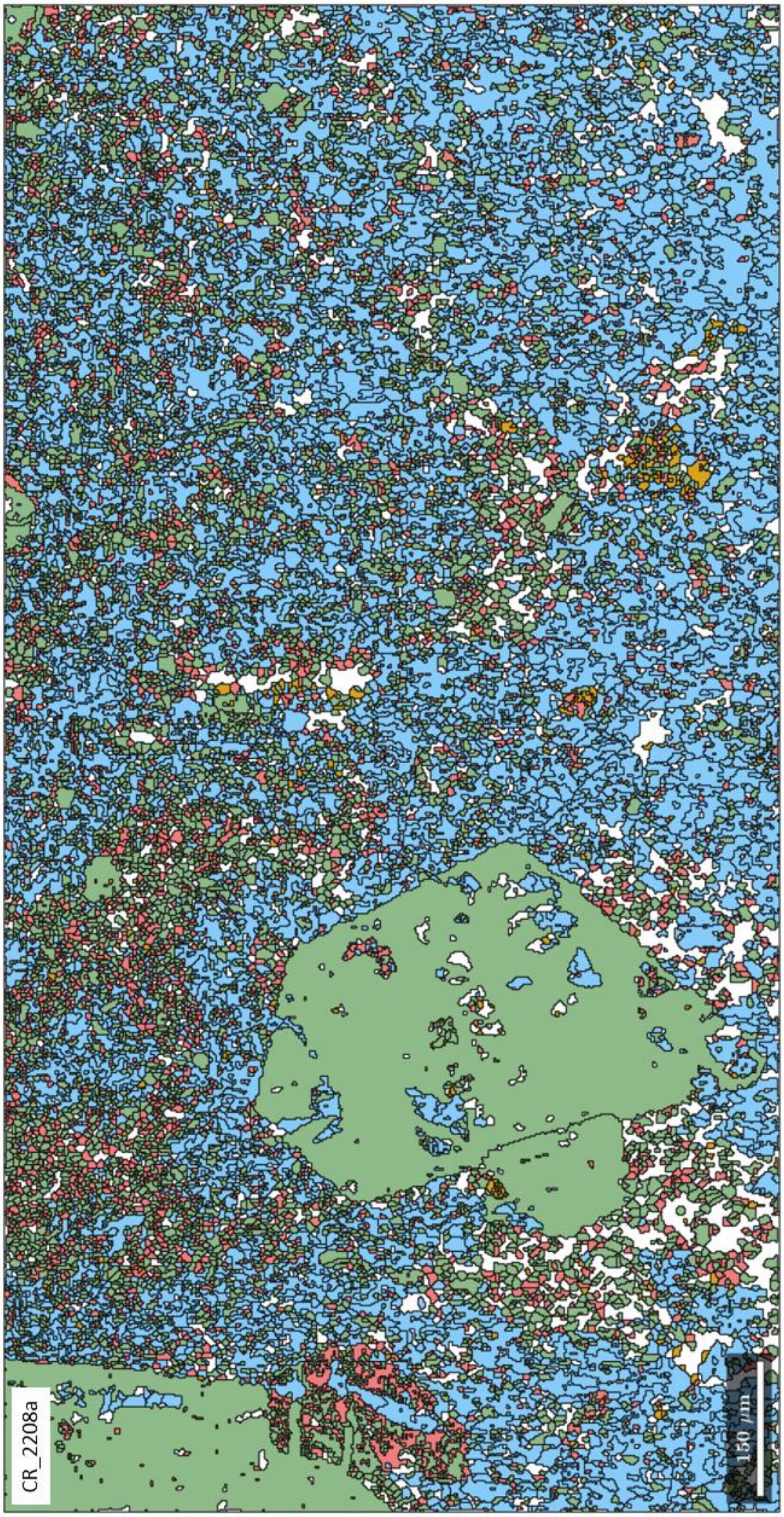
CR_2208a
150 μm

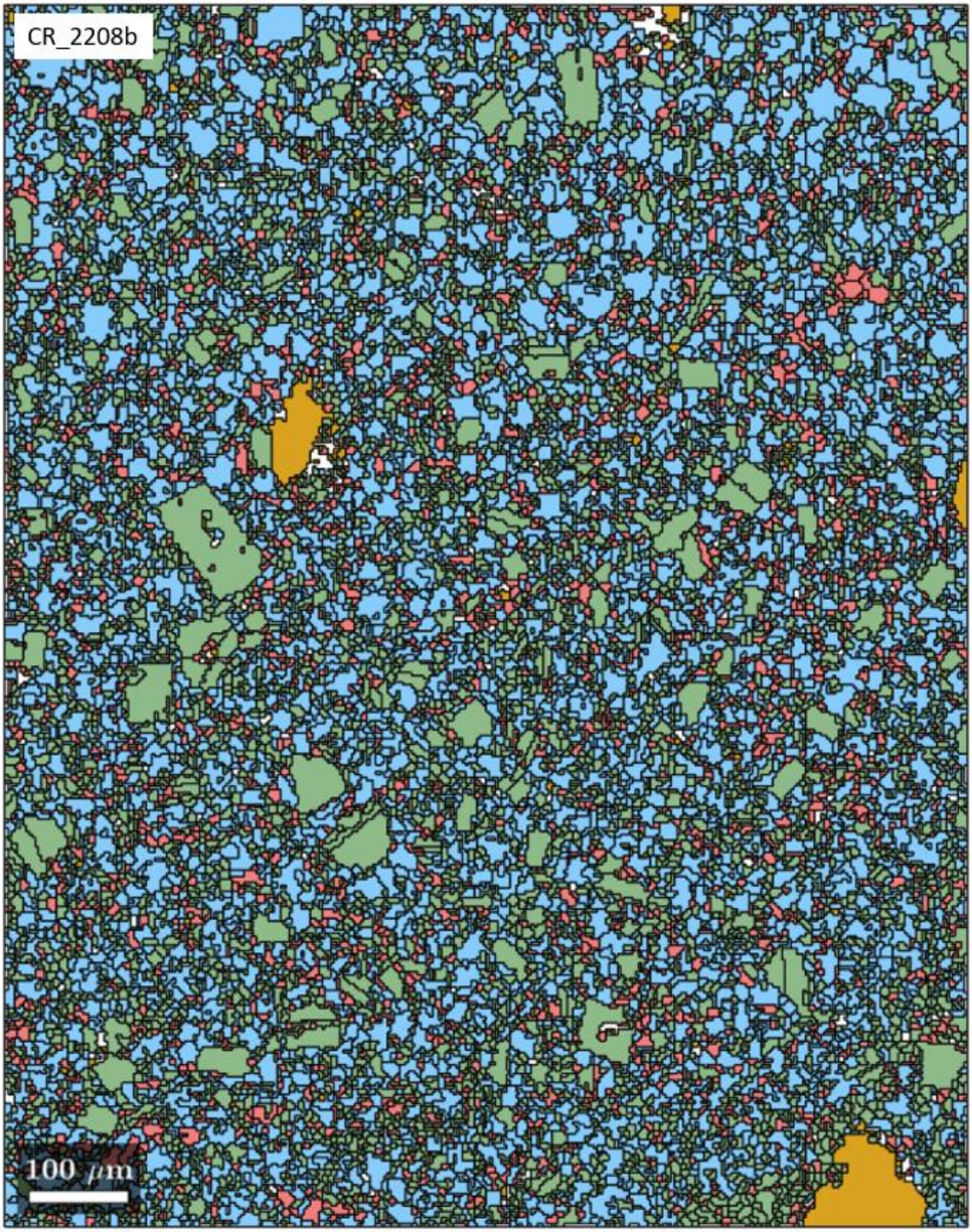
CR_2208b
100 μm